Evolution of galactic disks and spheroids

Dajana Dzanovic

Evolution of Galactic Disks and Spheroids

by Dajana Džanović

September 2004

Abstract

In this Thesis the structural properties of galaxies using quantitative 2-dimensional bulge to disk decompositions are analysed across a range of environments and redshifts. The study of morphological properties of galaxies is undergoing a significant progress since large galaxy surveys such as the Sloan Digital Sky Survey are producing a vast amounts of data enabling properties such as galaxy structure to be analysed on a statistical level. The wide-field imaging available today makes the studies of the nearby and high redshift environments comparable on a similar physical scale and depth. The advances in the theoretical studies and understanding the physics behind processes that govern galaxy formation and evolution make studies such as this one important since they provide basic estimates of galaxy structure that can be used to constrain the current theoretical models.

By comparing the structural properties of bright cluster galaxies between $z \sim 0.5$ and present we are able to confirm that galaxies have undergone a high degree of evolution although the exact processes that govern this evolution still remain unresolved. In order to account for the evolution of $z \sim 0.5$ cluster spirals into present-day S0s a significant number of spiral galaxies (factor of 3) must have had their disks faded to make them drop out of our magnitude limited sample. However, the structural properties between the faded-disk spirals and present day S0s are not consistent. One possibility is that the progenitor galaxies might have been accreted recently from the field and that these have also been previously pre-processed.

The study of the structural properties of field galaxies has resulted in a poten-

tial evidence that galaxies in the field environment have an additional structural component or structural property that cannot be accounted for by the current 2-dimensional decomposition methods. This study has found that disks contribute about 3 times as much light as bulges to the total luminosity density of the local universe. Tighter constraints in terms of bulge and disk mass densities would help to constrain the current theoretical predictions.

Evolution

of

Galactic Disks and Spheroids

by Dajana Džanović

A Thesis submitted to the University of Durham
in accordance with the regulations for
admittance to the Degree of Doctor of Philosophy.

Department of Physics
University of Durham

September 2004

Contents

List of Figures

List of Tables

Declaration

The work described in this Thesis was undertaken between October 2000 and September 2004 whilst the author was a research student under the supervision of Prof. Ray Sharples in the Department of Physics at the University of Durham. This work has not been submitted for any other degree at the University of Durham or at any other University. Portions of this work have appeared in the paper listed below.

- Džanović D., Sharples R.M., Benson A.J. & Frenk C.S., 2003, ApSS, **285**, 73-77.

Acknowledgments/Apologies

The time has come for me to apologise to all that have in some way or other influenced the days of the PhD.

First apology goes to my supervisor Ray Sharples for not quite getting it most of the time. To Andrew Benson and Carlos Frenk for not quite finishing the SDSS project. To John Lucey for bugging him with embarrassingly basic astronomy questions and to Michael Balogh for exactly the same reason. Apologies to Carlton Baugh and Lydia Heck for overworking the CDML cluster. To Alan Lotts for making him boost the home quota. Apologies to Pete Edwards too for almost taking over one of his projects. And to Pat for not buying much chocolate during the fantastic year 4.

My apologies to all the ex-office mates for having to share space and air with me.

Apologies to several special individuals for not being able to get rid of me.

One last thing - if ANYONE dares to mention two-dimensional bulge-to-disk decompositions to me EVER again - you have been warned!

Chapter 1

Introduction to Galaxy Morphology

In this Chapter a brief summary of the various methods for the morphological classifications of galaxies is given. Also discussed is the scientific motivation for the work undertaken in this Thesis.

1.1 The Hubble Sequence

The morphological classification of galaxies has traditionally been assigned visually using a scheme introduced by Hubble (1936). The so-called Hubble sequence has been somewhat modified since the original publication with new galaxy classes added by Sandage (1961) yet the basis for this 'Revised Hubble sequence' still remains the same. The Hubble system is based upon the prominence of the central concentration of light also known as a bulge or a spheroid, the presence of a disk and the morphology of the spiral arm structure within the disk. The Hubble classification system is nicely illustrated in the so-called tuning-fork diagram shown in Figure 1.1 and demonstrates that (in general) galaxies can be classified into four main morphological types : elliptical, S0, spiral and irregular.

Elliptical galaxies, E, are often referred to as 'early' types since in the Hubble sequence scenario they represent old systems which were the first to form. They are made out of old stellar populations and therefore in general have red colours. This galaxy type appears smooth and structureless with stellar motions very much randomised. The shape of elliptical galaxies is expressed in terms of their minor to major axis ratio.

Spiral galaxies comprise of a central region of high surface brightness which is embedded into a thin rotating disk of stars. The disks very often show internal structure such as the spiral arms - regions of enhanced brightness/star formation and are also known to exhibit barred structure. Spiral galaxies are sometimes referred to as 'late' types since they are believed to have formed at later times. They span a range of subtypes depending on the prominence of the bulge and the tightness of the spiral arms. The spectra of spiral galaxies are mainly dominated by young stars with the population of young stars increasing from types Sa-b to Sc-d.

Lenticular galaxies (also known as S0s) are intermediate between the elliptical and spiral types and form sort of a bridge between the two. They are characterized by a smooth central brightness component similar to an elliptical galaxy but they also contain a thin disk of stars similar to that of spiral galaxies but which is in contrast dominated by old stellar populations.

Irregular galaxies form another distinct galaxy type which appears not to have any regular structure at all. Irregular galaxies are quite often characterized by large star-forming and dusty regions.

The morphological properties of galaxies are not the only galaxy properties to be reflected in the Hubble tuning-fork. Integrated colours and spectral types for example exhibit a monotonic increase along the E-S0-Sab-Scd-Irr sequence i.e. the mean galaxy colour starts off as being red for ellipticals and becomes progressively bluer for late type spirals as the overall galaxy spectra become more dominated by young stellar populations. Since the prominence of the disk over the bulge increases in the similar fashion the above is strongly suggestive of a close link between galaxy spectral/colour properties and the underlying morphological appearance. However, there exists a large number of galaxies that do not comfortably fit onto the proposed classification scheme - a problem that was recognised by Hubble himself. This has become even more evident since the Hubble Space Telescope observations have revealed that the fraction of galaxies that fit comfortably onto the Hubble system drops as one looks deeper into the past (Abraham & van den Bergh 2001).

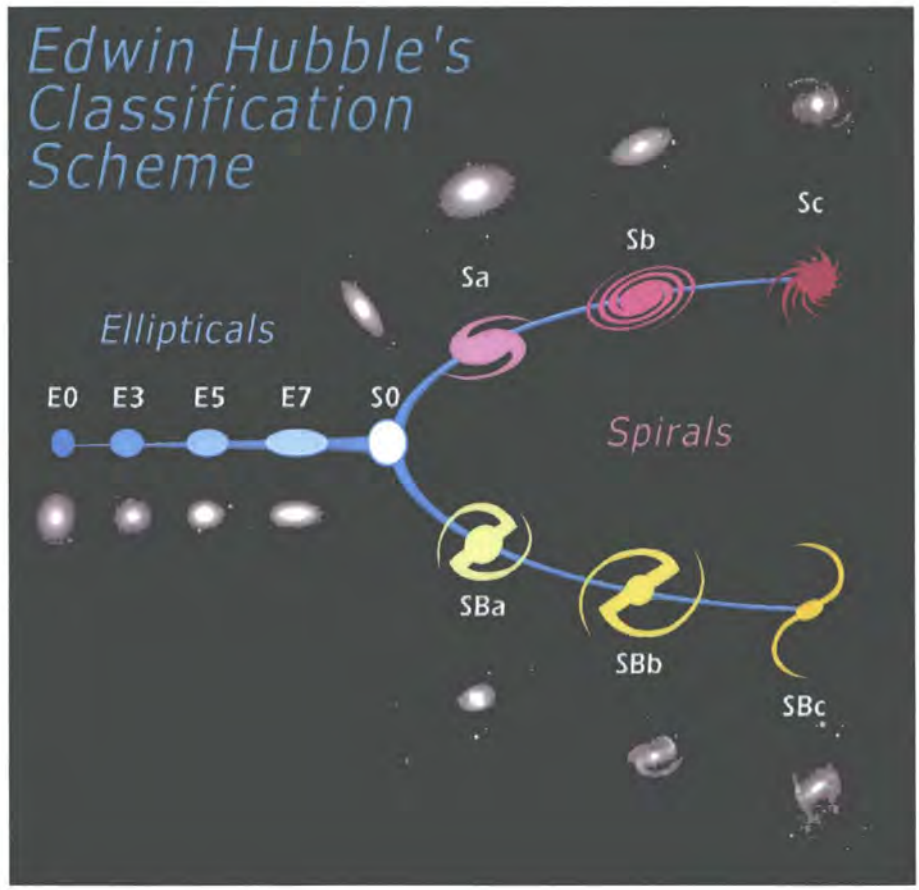

Figure 1.1: The Hubble's 'tuning-fork' classification scheme of galaxies. The morphologies range from elliptical galaxies on the left, S0s in the middle to barred and unbarred spiral galaxies on the right. The scheme is based on the visual appearance of galaxies according to how centrally concentrated they appear to be and also the presence (dominance) of the disk and the spiral arm structure.

1.2 Effects of Environment on Galaxy Morphology

The origin and the apparent diversity of galaxy morphology remains a long-standing issue which could provide a key to discerning among the existing models of galaxy formation and evolution. Investigating the morphological changes as a function of lookback time and correlating properties such as galaxy star formation rates and environment with galaxy morphology can have significant implications on understanding the mechanisms responsible for galaxy formation and evolution. For example, it has long been known (Sandage & Brucato 1979) that the field, where the galaxy density is much lower than that of a cluster region, is dominated by spiral galaxies. The fraction of elliptical galaxies and S0s in the field is typically of the order of $\sim$ 20% (Griffiths et al. 1994). The colours of the field spirals are also on average bluer than of those found in the cluster environment (Oemler 1992). Galaxy clusters on the other hand represent the other extreme galaxy environment since they are highly overdense regions of the universe that are predominately populated with elliptical and S0 types (Dressler 1980a). Furthermore a special class of massive ellipticals galaxies - cD - only occurs near the centres of rich clusters of galaxies. All this is indicative that galaxy morphology and environment are closely inter-related and therefore makes galaxy clusters a unique laboratory for studying the effects of environment on galaxy evolution.

There is a genuine need to create a coherent picture of how various galaxy types form and evolve. The small scatter around the colour-magnitude relation for elliptical galaxies found in the present-day clusters (Bower et al. 1992) and in clusters at intermediate redshifts (Ellis et al. 1997) is consistent with these galaxies having formed at high redshifts. These studies have also revealed that the population of E/S0 galaxies was bluer in the past i.e. the colour-magnitude relation still holds but is shifted to 'blue' colours for clusters at intermediate redshifts. This could be

taken as a suggestion that galaxies may have experienced a cluster-induced evolution however, a similar trend (studied in terms of the galaxy star formation rates) was found for galaxies that belong to the general field population (Lilly et al. 1996) where the star formation rate was found to be much higher in the past. It is therefore difficult to separate galaxy evolution which might be due to the simple passive consumption of gas and that which is induced by galaxy environment. Since many different processes can be at work within the cluster environment itself it is proving to be very difficult to distinguish between the various physical mechanisms that could be responsible for the environmentally-induced evolution within the galaxy clusters themselves (Treu et al. 2003).

In recent years evidence has accumulated that environmental processes can affect both the star formation (Kennicutt 1998, Moss & Whittle 2000) and morphological (Dressler 1980b, Smail et al. 1997, Goto et al. 2003) characteristics of galaxies but the nature and timescale of the relevant evolutionary processes remain unclear. Galaxies are known to interact with one another or with the gas that may fill the environment they live in and are therefore likely to experience changes in their appearance and gas/stellar content as a direct result of the environment. A galaxy can interact with the intercluster medium via ram pressure stripping or some other cluster-related mechanism. This leads to a direct removal of the gas supply followed by the termination of the star formation after a possible temporary short-term increase in the star formation (Gunn & Gott 1972, Abadi et al. 1999). A cluster galaxy can gravitationally interact with the cluster potential and such cluster-induced tidal interactions can act to temporarily increase the star formation rates. This would lead to an increase in the consumption of the gas supply effectively leading to a quenching of star formation and rapid changes in the galaxy structure (Fujita 1998). Finally, cluster galaxies can mutually interact via mergers or galaxy harassment (Moore et al. 1999). A common thread between all of the above mentioned processes is that they are responsible for a gradual slowing down and eventual halting of the star formation in galaxies - what is now commonly termed as 'starvation'.

All cluster-related processes will eventually lead to the morphological changes that follow the 'starvation' of galaxies but depending on the exact process(es), that again may act in different parts of the cluster, the morphological changes are likely to occur on different timescales from those observed in terms of the change in the star formation rate. This can prove to be a powerful tool for determining what mechanism is more effective within a different region of a galaxy cluster (Treu et al. 2003). Treu et al. (2003) also suggest that galaxies may get preprocessed in groups before they get accreted to become part of the cluster itself. This indeed is plausible since the morphological segregation of galaxies is also found to hold in X-ray bright galaxy groups (Heldson & Ponman 2003).

The environmental effects on galaxy evolution and morphology can also be studied as a function of the local projected galaxy density. The idea was first studied in more detail by Dressler (1980b) who used the morphology-density relation (where density was defined to be the surface density to the 10^{th} nearest projected neighbour) as a way of investigating the environmental effects on galaxy evolution in what appeared to be non-centrally concentrated (non-relaxed) clusters. Dressler (1980b) found that the morphology-density relation in the local universe was identical for relaxed (centrally concentrated) and non-relaxed clusters. However, a study by Whitmore et al. (1993) showed that galaxy morphology is also strongly correlated with the distance from the cluster centre with the fraction of ellipticals steeply rising in the cluster core thus claiming the morphology-radius relation a more fundamental one. This only demonstrates how difficult it is to disentangle which (local or global) effect is more important because the local density and the distance from the cluster centre are closely correlated in relaxed clusters. Dressler et al. (1997) extended the study of the population gradients as a function of the local galaxy density to a sample of intermediate redshift clusters ($z \sim 0.5$) and found that for clusters which appeared to be highly centrally-concentrated the fraction of early-type galaxies was a steeply increasing function of local density. In contrast with what was found for the nearby clusters, the low-concentration clusters at intermediate redshifts showed no gradient in the morphological mix with local density possibly because the intermediate redshift low-concentration clusters were not yet

fully evolved so that the corresponding segregation of the morphological types did not have time to occur (Dressler et al. 1997). In addition, Dressler et al. (1997) found that the galaxy population mix within the cluster environment appears to have undergone a transformation between $z \sim 0.5$ and present since the relative proportion of spiral galaxies in $z \sim 0.5$ clusters was found to be several times higher than in the nearby clusters. The study also revealed a large number of interacting galaxies and galaxies with peculiar morphologies (Smail et al. 1997).

In the spectroscopic follow-up of the intermediate redshift cluster spiral galaxy populations Poggianti et al. (1999) showed that these galaxies appear to have had their star formation (SF) ceased abruptly in the very recent past and subsequently termed them 'passive spirals'. Although the morphology of these galaxies was consistent with them being late types their SF activity was found to be much less than that of the corresponding field counterparts (Dressler et al. 1999). This is suggestive of an evolutionary environment-related mechanism(s) which presumably acts to transform the $z \sim 0.5$ cluster spirals into the present-day S0s and which appears to work on two time scales. One mechanism abruptly stops the star formation, occurs on a timescale of ~ 1 Gyr and is responsible for creating the passive spiral galaxy population observed in $z \sim 0.5$ clusters and the second mechanism is responsible for the morphological transformation of spirals to S0s, takes several Gyrs and appears to have taken place between $z \sim 0.5$ and present.

In an attempt to form an evolutionary bridge between the galaxy populations seen in clusters at $z \sim 0.5$ and the present Couch et al. (1998) studied the morphological mix in three clusters at $z = 0.31$. Couch et al. (1998) found that the fraction of spirals/S0s was significantly lower/higher than that found for the $z \sim 0.5$ clusters although not as low/high as that found for the nearby cluster sample. Examining the spectral signatures of their morphologically classified galaxies Couch et al. (1998) concluded that most of the star-forming galaxies are consistent with being late type spirals but also find a significant number of late morphologies that have had their star formation truncated in the recent past (passive spirals). These galaxies show no preferred position within the cluster itself although there is some

(small number statistics) evidence that the spiral galaxy excess does depend on the global cluster environment. This study is suggestive of several physical processes governing the morphological changes within the cluster and of a continuous accretion (and transformation) of galaxies from the field.

In summary the existence of some environment-related process(es) governs the change of the morphological properties of galaxies in clusters and appears to have taken place between $z \sim 0.5$ and present. The question that remains to be answered is what this process(es) might be and how can we distinguish between the simple galaxy evolution due to the gradual consumption of gas and the more rapid one induced by the galaxy environment i.e. nature vs nurture scenario (Bower 1990). In order to study the processes which might govern the morphological changes of galaxies there remains a need for a robust morphological classification scheme since its correlation with other galaxy properties and galaxy environment can lead to understanding of the nature of galaxy evolution. Morphology is one of the key observational characteristics used to classify and differentiate classes of galaxies and one of the most sensitive traces of environmental evolution.

1.3 Quantitative Means of Classifying Galaxies Morphologically

A traditional way to obtain galaxy morphologies is to visually classify them using the Hubble system. However, this process can be very subjective and time consuming if the number of galaxies is large (Dressler 1980a, Smail et al. 1997). Signatures in the galaxy spectra can be employed to allow for a broad morphological classification of galaxies thus making it possible to analyse large galaxy samples (Domínguez 2001). Although a general correlation between the spectroscopic and Hubble morphologies is known to exist the samples derived from the two methods can be considerably different. In particular, classification using the spectroscopic features is sensitive to any small-scale star-formation activity occurring relatively

recently in early type galaxies, while the Hubble morphology is insensitive to this process. Equally, a late-type Hubble morphology might have exhausted most of its star-forming fuel at present but has not yet had time to undergo a full morphological transformation. de Vaucouleurs (1961) were the first to establish a broad correlation between the galaxy colour (which arises from the dominant stellar populations) and the morphological type. In a recent study Strateva et al. (2001) have made use of the colours to broadly separate galaxies in two classes : red (ellipticals and S0s) and blue (spirals) enabling a morphological study of a large data-set. A slightly different approach that is not based on the underlying stellar populations/galaxy colours was pioneered by Abraham et al. (1994) who used the concentration index as a means of automated morphological classification of galaxies. A concentration index measures how centrally concentrated galaxy light profiles is i.e. the more peaky the surface brightness of a galaxy is the higher the concentration index and the more elliptical-like the galaxy should be. Using the concentration index Abraham et al. (1994) showed that galaxies can be broadly separated into elliptical and spiral morphologies and has proven particularly useful when dealing with large galaxy samples (Smail et al. 1997). Both the colour and the concentration index have been investigated as a function of visual morphology by Shimasaku et al. (2001) for a large sample of galaxies and have found there to be a broad correlation with the contamination typically of the order of $15 - 20\%$.

Table 1.1: Morphological classification schemes. The T-scheme represents the numerical Hubble sequence and is useful in quantitative morphological studies. The table is taken from van den Bergh (1998).

Hubble	E	E-S0	S0	S0/a	Sa	Sa-b	Sb	Sb-c	Sc	Sc-Irr	Irr I
de Vauc.	E	$S0^-$	$S0^o$	$S0^+$	Sa	Sab	Sb	Sbc	Scd	Sdm	Im
T	-5	-3	-2	0	1	2	3	4	6	8	10

In a quest to create a more detailed and more quantitative morphological classification system de Vaucouleurs devised a system represented in terms of a T-parameter defined in Table 1.1. The T-parameter correlates strongly with inte-

grated colours of galaxies and also describes the apparent morphological features in more detail (van den Bergh 1998). Apart from being subjective this classification scheme suffers from the luminosity and evolutionary effects being projected onto a single classification parameter i.e. galaxies simultaneously become fainter and bluer along the sequence (van den Bergh 1998).

The above reflect a need for a classification scheme that is more quantitative in nature, which should be non-subjective and reproducible and whose biases can be understood and characterised through simulations.

More recently quantitative measures based on fitting two-dimensional galaxy surface brightness profiles to the galaxy bulge and disk components have been shown to produce non-subjective measures of the Hubble morphology that can be applied to a large sample of galaxies and across a relatively large redshift range (Ratnatunga et al. 1999, Simard et al. 2002). The main advantages of using the two-dimensional bulge-to-disk decomposition methods is that they are reproducible and that their limitations can be understood through simulations. They also give quantitative estimates (with errors) of the galaxy structural components and of the amount of luminous mass that resides in these components. The main problem with the methods is that they are parametric i.e. they use empirically deduced laws to fit galaxy surface brightness components. The particular empirical formalisms came in use after specific studies have demonstrated that galaxy bulges are well fit assuming a '$r^{1/n}, n = 1, ..., 6$' profile (Andredakis et al. 1995) and that disks are well fit assuming an exponential disk model (de Jong 1996).

Although based on the same empirical laws, the number of fitting parameters that arise from employing these formalisms have led to a number of different decomposition methods to be developed. The main differences between the methods lie in the minimization routines they use to obtain the galaxy fits, the way they correct for the effect of seeing and the shape of the bulge profile they assume. A number of codes have been used to obtain structural properties of galaxies in clusters ranging from the present-day all the way to $z \sim 0.3$ (McIntosh et al. 2002, Tru-

jillo et al. 2001, Tran et al. 2003, Balogh et al. 2002) while other codes have been used to study the general field populations (Wadadekar et al. 1999, Ratnatunga et al. 1999, Benson et al. 2002, Simard et al. 2002). The performance of one of the decomposition methods, Gim2D written by Simard et al. (2002), has been compared with the decomposition outputs of the Medium Deep Survey of Ratnatunga et al. (1999). These were found to be in good agreement with no obvious systematic differences (Simard et al. 2002).

The two-dimensional (2D) bulge-to-disk decomposition methods have lead to some interesting scientific discoveries. McIntosh et al. (2002) have used Gim2D (Simard et al. 2002) to study properties of a population of blue galaxies in nearby clusters ($z < 0.06$) and of the corresponding field population. They found that cluster galaxies do to indeed have different structural properties that can be explained by the accretion of field spirals and their subsequent cluster-induced evolution. They also find that no single physical process can explain all the differences seen between the cluster and the field samples and that preprocessing in groups is very likely. Gim2D has also been used to explore properties in clusters at $z \sim 0.25$ selected based on their X-ray luminosity (Balogh et al. 2002). This study revealed that the observed bulge-to-disk ratios appear to depend on the global cluster properties (i.e. X-ray luminosity) where the low X-ray luminosity clusters were found to be predominately populated with galaxies with smaller bulge-to-disk ratios in contrast with galaxies that belong to X-ray luminous clusters. The code developed by Trujillo et al. (2001) has been used to study galaxies in clusters across a range of redshifts to test for structural evolution in galaxies between past ($z \sim 0.1$) and present (the Coma cluster at $z = 0.02$).

1.4 The Thesis Aim

In this Thesis we study quantitative morphological properties of galaxies in different environments - galaxy clusters and field. We also investigate the evolution of these properties with redshift to try to understand the mechanisms that cause galaxy ap-

pearance and structure to change in clusters from $z \sim 0.5$ to the present-day. The motivation for this work comes from the past studies (Dressler 1980b, Dressler et al. 1997). However, in this Thesis quantitative measures of basic structural parameters of galaxies are used to explore the amount evolution in terms of the change in the galaxy structural parameters and in terms of various physical processes that may be acting as a direct consequence of galaxy environment.

In Chapter 2 we present the results of a comparison of two independent decomposition methods (codes) for determining galaxy bulge-to-disk ratios :

- Gim2D - publicly available code written by Luc Simard, and the
- Fit-Galaxy code written by Andrew Benson (private communication).

We test both methods using simulations to try to quantify any limitations and biases the codes may have. We also run both codes on real data to reveal any systematic differences. In Chapters 3 and 4 we use Gim2D to study the evolution of galaxy properties from $z \sim 0.5$ to present in *clusters*. The quantitative bulge-to-disk ratios obtained from the CCD imaging of galaxy clusters at $z \sim 0.0$ and $z \sim 0.5$ are correlated with the visually obtained galaxy morphologies to try to put constraints on the nature of galaxy evolution in clusters. A particular care is taken in trying to understand the mechanism(s) which appear to have transformed the $z \sim 0.5$ spiral galaxies into the present-day S0s.

The Fit-Galaxy code has already been used by Benson et al. (2002) in a study of a small (~ 100) *field* galaxy sample which revealed that the total luminosity densities of bulges and disks in the field to be very similar. Therefore we employ the Fit-Galaxy code to determine the bulge-to-disk ratios of a larger (~ 9000) sample of field galaxies to try put constraints on the current theoretical studies of galaxy formation and evolution and present the results in Chapter 5.

The summary and conclusion for this Thesis are presented in Chapter 6.

Chapter 2

Quantitative Galaxy Morphology

In this Chapter two independent methods for bulge-to-disk decompositions of galaxies are introduced and compared. A number of tests are performed to reveal and estimate any potential biases in each of the decomposition routines. The codes are used in the subsequent Chapters to study the evolution of quantitative structural properties of galaxies with redshift and as a function of environment.

2.1 Introduction

2.1.1 Introduction to Bulge-to-Disk Decompositions

The surface brightness of a galaxy is commonly expressed in terms of the highly concentrated central component, also known as the bulge or spheroid, and the extended disk. The empirical formalisms that have been shown to well represent the surface brightness profiles of bulges and disks are given by :

$$I_b = I_e exp(-7.67[(r/r_e)^{1/4} - 1]) \tag{2.1}$$

i.e. an $r^{1/4}$-law for the bulge, where r_e is the half-light radius and I_e is the surface brightness at r_e, and,

$$I_d = I_0 exp(-r/r_d) \tag{2.2}$$

an exponential-law for the disk, where r_d is the exponential disk scale-length and I_0 is the central intensity.

Equations 2.1 and 2.2 can be used to define a set of free parameters that (once determined) can be used to create a model image of the galaxy. A comparison

between the model and real galaxy surface brightness distributions, including inclination effects, indicates how well the assumed parameters represent the underlying galaxy light. If these are found to agree then the fitting (model) parameters can be taken to be represent the galaxy structure well enabling the galaxy structural properties such as the bulge-to-disk ratios (the ratio of the total luminosity in the bulge to the total luminosity in the disk) to be investigated.

2.1.2 Historical Development of Bulge-to-Disk Decomposition Methods

Kent (1985) was first to introduce a simultaneous fitting of the bulge and disk components by determining the fitting parameters I_0, I_e, r_d, r_e and i (where i is the inclination of the galaxy disk and is defined to be the angle between the normal to the disk and the line of sight) from the quality of the fit. The accuracy of the bulge-to-disk decomposition was found to vary widely and the best decompositions were obtained for objects that had easily separable bulge and disk components. Nevertheless, the results demonstrated the validity of the assumed empirical laws and showed that there exists a good correlation between the Hubble morphology and the inferred bulge-to-total ratios (B/T*). Figure 2.1 demonstrates that the dominance of the bulge decreases from type S0 to Sc and indicates a good correlation between the Hubble morphology and B/T.

Andredakis et al. (1995) used a more generalized form of Kent's decomposition method to specifically fit the bulge components of a sample of morphologically selected galaxies with types ranging from S0 to Sbc. The bulge light profile was fit using a more general type of profile : $I_b = I_e exp(-7.67[(r/r_e)^{1/n} - 1]$, first proposed by Sérsic (1968), where n is often referred to as the Sérsic index and determines the 'peakiness' of the profile. Andredakis et al. (1995) let n be a free parameter

*B/T is the fraction of the total luminosity that is contributed by the bulge and is related to bulge-to-disk ratio via $B/D = [(B/T)^{-1} - 1]^{-1}$. The advantage of using B/T is that it is confined to the interval $[0, 1]$.

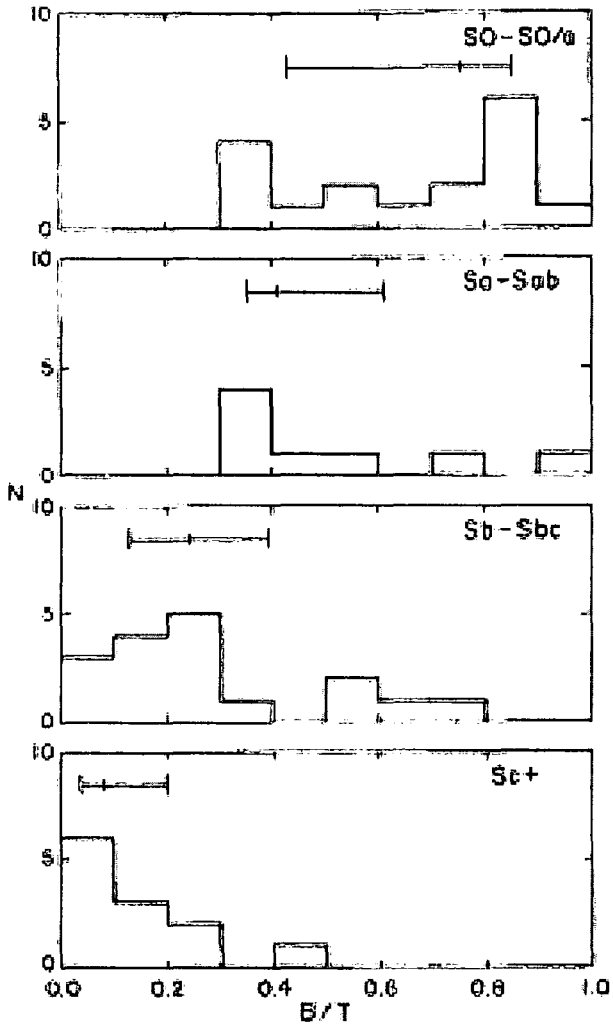

Figure 2.1: Distribution of B/T as a function of morphological type taken from Kent (1985). This correlation quantifies the Hubble classification which is based upon the prominence of the bulge i.e. more bulge-dominated types (S0, Sa) have larger B/T ratios.

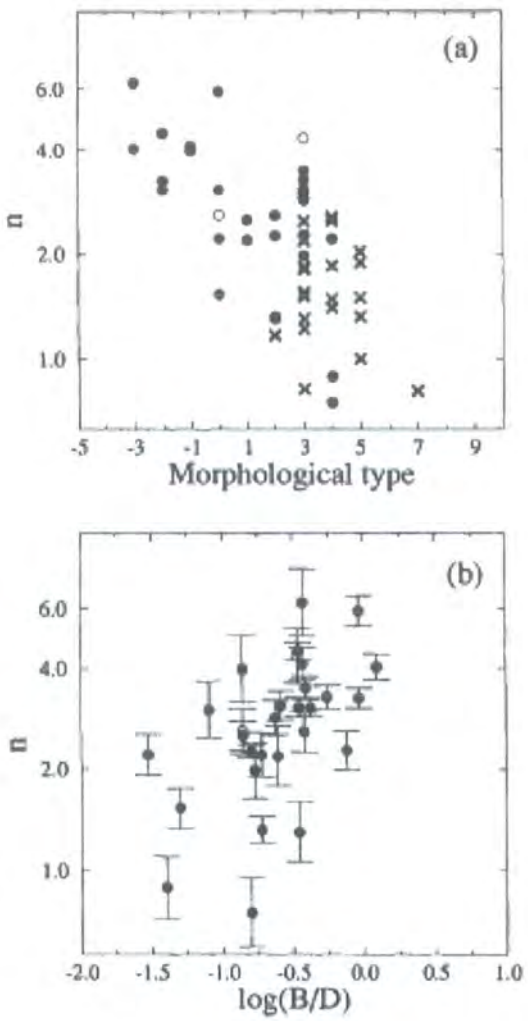

Figure 2.2: (a) The best-fitting Sérsic index n (plotted in logarithm) versus the morphological type of the galaxy. Andredakis et al. (1995) = circles, Kent (1985) = crosses. (b) n versus bulge to disk ratio, B/D, suggesting that n increases with the B/D ratio. Figure taken from Andredakis et al. (1995).

and found that its value varied systematically from 1 for late-type bulges to 6 for early-type bulges (Figure 2.2). de Jong (1996) was also to suggest that bulges of field spirals are better fit using a pure exponential i.e. $n = 1$ type of profile. As well as fitting n the above studies also introduced several new fitting parameters : the bulge and disk position angles (PA_b and PA_d, where a position angle is defined as the angle of orientation of the galaxy's main axis with respect to a coordinate system) and the bulge ellipticity (e_b, used to describe the flattening of the bulge component). The role of these parameters can be best understood in terms of a galaxy placed on a 2-dimensional Cartesian grid of (x, y) centered on the galaxy such that the position of every point of the galaxy bulge and disk component on this grid is respectively represented by Equations 2.3 and 2.4.

$$r_e(x,y)^2 = \frac{1}{e_b}[x\cos(PA_b) - y\sin(PA_b)]^2 + e_b[x\sin(PA_b) + y\cos(PA_b)]^2 \quad (2.3)$$

$$r_d(x,y)^2 = [x\cos(PA_d) - y\sin(PA_d)]^2 + \frac{1}{\cos(i)^2}[x\sin(PA_d) + y\cos(PA_d)]^2 \quad (2.4)$$

The idea behind the 2D bulge-to-disk decomposition methods is that if the model galaxy, deduced from the best-fit parameters as defined above, represents the real galaxy profile well than these parameters can be used to infer and study the properties of different structural components of the galaxy itself (for more information on the parameter minimization see Appendix A.1).

2.1.3 Multi-parameter Fitting and Computing Time

The studies of Kent (1985), Andredakis et al. (1995), de Jong (1996) have dealt with samples of up to 100 galaxies and despite the ever increasing number of parameters the computing time for these studies did not represent a large problem. However, wide-field cameras used today produce survey data of a vast number of galaxies that can be studied in terms of their quantitative morphologies. One such survey is the Medium Deep Survey (MDS) of Griffiths et al. (1994) and the authors discuss the problem of choosing between fitting too few parameters, which can potentially lead to serious biases, and fitting too many parameters which would lead to increase in the computing time. As a trade-off between the number of fitting parameters and

the computing time Ratnatunga et al. (1999) adopt a maximum likelihood image analysis which attempts to automatically optimize the number of fitting parameters for every galaxy in the MDS. More sophisticated mathematical techniques, such as the Metropolis algorithm used by Simard et al. (2002), have been employed to provide fast and robust way of determining bulge and disk components of a large number of galaxies given a large number of fitting parameters. Also, the development of computing facilities enables these quantitative methods to be done in a reasonable amount of computing time.

2.2 Methods for 2-Dimensional Bulge-to-Disk Decomposition

2.2.1 Fitting Parameters Revisited

In terms of a $r^{1/n}$ bulge and an exponential disk and including the contribution of the total galaxy flux and the sky background the 2D decomposition usually leads to a total of 12 free parameters :

- total flux : total flux in the model galaxy,
- B/T : ratio of the amount of light in the bulge and the total amount of light,
- r_e : effective radius of a bulge,
- e_b : bulge ellipticity,
- PA_b : bulge position angle,
- r_d : effective radius of a disk,
- i : inclination angle of a disk,
- PA_d : disk position angle,
- x_c, y_c : subpixel offset of the model centre with respect to the galaxy centre,
- background flux : residual sky background level,
- n : Sérsic index.

To enable the decomposition procedure to be as accurate and as fast as possible the emphasis is put on the following :

- The importance of correcting for the Point Spread Function (PSF[†]) since the PSF acts to smear out the central (core) region of the real galaxy and if the same is not done for the model galaxy i.e. if the seeing is not corrected for, this can lead to a false estimate of the galaxy components particularly the bulge.
- Using postage-stamps or thumbnail-images that are extracted around and centered on the galaxy of interest. The importance of using postage-stamp images lies in the fact that the decomposition run-time depends upon the number of pixels in the image i.e. larger the postage-stamp is longer the time for the object decomposition. However, the extracted postage-stamp image should not be made too small either since they need to have enough sky-background pixels to ensure a good discrimination between the sky background and the galaxy flux.
- The mean sky background level should be ~ 0 since the decomposition codes have been designed to work with no (or very little) underlying background and is important because any excess sky light can be swapped for the galaxy light and could therefore lead to incorrect B/T and other parameter estimates.

In the two fitting procedures described in this Chapter any deviations from the above will be noted and if necessary discussed in more detail. In this Chapter we explore similarities and differences of two independent multi-dimensional fitting codes : the Gim2D code of Simard et al. (2002) and the Fit-Galaxy code of Benson et al. (2002).

2.2.2 Galaxy Image 2D Decomposition - Gim2D

Introduction

This section introduces Gim2D - a publicly available code written by Simard et al. (2002) which has been widely used for the automated bulge-to-disk decompositions of galaxy light profiles (Balogh et al. 2002, Nelson et al. 2002). This code was purposely written for imaging obtained using the Hubble Space Telescope (HST)

[†]PSF is a measure of how much the light from a distant point source is smeared due to the atmosphere and telescope optics.

Wide Field and Planetary Camera (WFPC2) which has a very well modelled PSF (Krist 1995). However, the code can also be used for ground-based data but in case of the ground-based imaging we have to ensure that the decompositions are preformed accurately given a much larger and not as well defined PSF.

Object Detection

To locate and extract a small postage-stamp image around every galaxy Gim2D relies upon SExtractor, the object detection algorithm written by Bertin & Arnouts (1996). SExtractor allows for the galaxy centroid position and the isophotal area (area at the faintest isophote) to be obtained once the object is detected and a postage-stamp image is extracted. SExtractor also measures the mean level of the sky background for each galaxy (3σ threshold is usually sufficient to discriminate between the object and the background) and this value is subtracted from the corresponding galaxy image in Gim2D. In the work presented here, Gim2D is set to extract a postage-stamp of a size set to a multiple of a galaxy isophotal area. A value of $15 \times iso_{area}$ was selected after some model tests. This provides enough background pixels for an accurate determination of the sky background but makes the postage-stamp sufficiently small to ensure a reasonable run-time. It typically takes $\sim$ 5 minutes to decompose a 91 $\times$ 91 pixel image. If the postage-stamp size is increased to 181 $\times$ 181 pixels the run-time can increase up to an hour. The sky-background is not recommended to be a free fitting parameter in Gim2D because the underlying sky is not well known and can potentially bias the output (Simard et al. 2002). However, before the decomposition procedure is initiated, Gim2D uses the pixels flagged by SExtractor as belonging to the background (flag value 0) to recompute the background value and therefore ensures that the mean sky level really is close to zero. All the background pixels and also pixels flagged as 'bad' (flag value -2) by SExtractor are subsequently excluded from the fitting altogether.

Point Spread Function

During the minimization in Gim2D the seeing is kept fixed. It is taken to be a bright unsaturated stellar image for ground-based imaging or in case of the Hubble

Space Telescope observation an analytic PSF modelled using the Tiny Tim software (Krist 1995).

Minimization Technique : Metropolis Algorithm

Gim2D allows for up to 12 parameters to be fit and uses the Metropolis algorithm (Metropolis et al. 1953) to search for the minimum χ^2 in this multi-dimensional parameter space. Before starting the Metropolis algorithm, Gim2D works in the Initial Condition Filter (ICF) mode i.e. it creates a user-specified number of models between the limits of the user-specified multi-dimensional parameter space example of which is given in Table 2.1. The ICF computes the given model likelihoods and once it has created the given number of models the ICF sets the sampling origin to the parameters of the best model, making it a sub-volume to be exploited by the Metropolis Algorithm.

Table 2.1: Gim2D : Multi-dimensional parameter space limits.

Parameter	Initial	Low	High	Step
ICF	300			
Total Flux	300000.0	100000.0	500000.0	400000.0
B/T	0.5	0.0	1.0	1.0
r_e	10.0	0.0	20.0	20.0
e_b	0.35	0.0	0.7	0.7
PA_b	90.0	-360.0	360.0	180.0
r_d	10.0	0.0	20.0	20.0
i	45.0	0.0	85.0	85.0
PA_d	90.0	-360.0	360.0	180.0
x	0.0	0.0	1.0	0.1
y	0.0	0.0	1.0	0.1
Sky Background	0.0	0.0	0.0	0.0
n	4.0	4.0	4.0	0.0

The first line of the parameter file shown in Table 2.1 indicates the number N

of initial multi-dimensional searches in terms of the Initial Condition Filter (ICF). The subsequent lines define the multi-parameter volume with the first column indicating the initial parameter values. The second and third columns represent the minimum and maximum limits on the parameter values. No values outside these hard limits will be explored by the ICF or the Metropolis algorithm. Finally, the fourth column sets the size of the initial perturbation to be applied to the parameters during the ICF search. If a given parameter(s) is not to be fit then the size for the initial perturbation is set to zero and all other values to a constant that represents the adopted parameter value (in this case Sky Background is not fit and the value is set to 0). For each of the N models Gim2D computes the likelihood that the parameter set is the true one given the data and the model. After sampling the parameter space N times in the ICF mode Gim2D picks the best model i.e. the model with the highest likelihood as the starting point for the Metropolis algorithm minimization.

After the best initial model is found the Metropolis algorithm computes the likelihood that the parameter set is the true one given the data and the model, P_0. It then generates a random trial perturbation about the initial parameter values, assigns it a 'temperature' and computes the likelihood value for this trial perturbation, P_1. If $P_1 > P_0$ the 'new location' is immediately accepted. If $P_1 < P_0$ the perturbation will only be accepted P_1/P_0 of the time which means that the algorithm will sometimes accept trial perturbations which will take it to the region of lower likelihood and therefore avoids getting stuck in the local minima. The size of the trial perturbation depends upon the number of iterations accepted - if too many are being accepted the 'temperature' is increased and larger perturbations are tried. If too many are being accepted, the 'temperature' of the search is decreased and the size of the trial perturbation is decreased too. The convergence is achieved when the difference between the two likelihood values separated by a 100 iterations is less than 3σ of the likelihood value fluctuation. The errors are derived using a Monte Carlo approach of the parameter probability distribution and are given in terms of 68% confidence limits on the fitted parameters. Figure 2.3 demonstrates search through a 1-dimensional B/T space. Note that the Metropolis algorithm initiates

a large search (part of the ICF) and fairly quickly starts to converge towards what it thinks is a minimum. A useful feature of the algorithm is that (unlike gradient method searches) it will try to 'get-out' of the converging minimum by widening the search. If it fails to find a better defined minimum it will converge again and the process is repeated until the 'real' minimum is found.

Gim2D Outputs

After it finds the model that corresponds to the highest likelihood, Gim2D produces a residual (object - model) map and calculates the value of the corresponding χ^2_ν. If $\chi^2_\nu \sim 1$ and the residual map is noise dominated and without any remaining galaxy structure, the best-fit model is accepted to represent the real galaxy profile well.

2.2.3 Fit Galaxy

Introduction

The 2-dimensional decomposition code described here is based on a technique deployed by Wadadekar et al. (1999). Fit-Galaxy is a private code that was developed by Benson et al. (2002) and assumes the standard empirical formalisms for the 2-dimensional surface brightnesses of a galaxy bulge and disk components respectively (Equations 2.1 and 2.2).

Object Detection

To locate and extract a small postage-stamp image around every galaxy Fit-Galaxy relies upon SExtractor the object detection algorithm written by Bertin & Arnouts (1996). SExtractor allows for the galaxy centroid position to be obtained once the object is detected and a postage-stamp image around it is extracted. SExtractor also measures the mean level of the sky background for each galaxy (3σ threshold is usually sufficient to discriminate between the object and the background) and this value is subtracted from the corresponding galaxy image. To mask the overlapping objects within the extracted postage-stamp Fit-Galaxy relies upon an in-built masking algorithm which finds any objects that contaminate the galaxy of interest

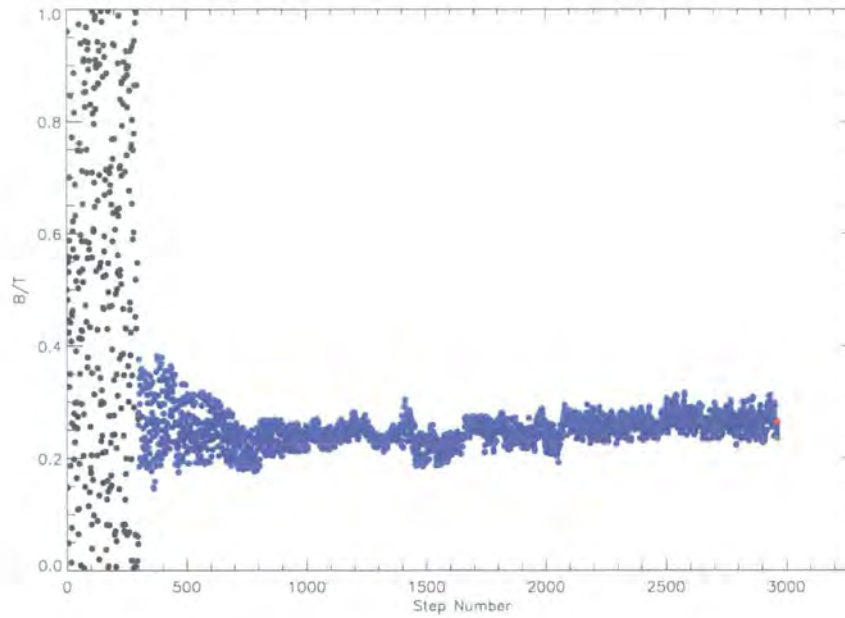

Figure 2.3: Figure illustrates B/T search of the Metropolis algorithm. Initially a large search volume is explored between the limits set in the parameter file (black dots). The likelihood is computed for every set of parameter values and after the initial search is done the parameter set with the highest likelihood is accepted (red dot at 300). This parameter set defines the new sampling origin and smaller random perturbations around this origin are tried (blue dots). The size of the trial perturbation depends upon the number of iterations accepted through a parameter defined as 'temperature'. If the number of accepted iterations is large the 'temperature' is hot (convergence is starting to occur) the size of the trial perturbation is increased and larger perturbations are tried. However, if the 'temperature' is cold the size of the trial perturbation is decreased. The process is repeated until the difference between two likelihood values separated by 100 iterations is less than 3σ of the likelihood fluctuation indicating that the convergence is achieved (red dot at 3000). An extremely important feature of the algorithm is that if it finds a local minimum it will try to get out of it. This model galaxy has $B/T_{true} = 0.234$ (green dot).

and masks them out. The galaxy itself is also detected by the algorithm using a 5σ threshold above the sky background. Pixels which have not been flagged as belonging to any of the detected objects are used in the sky background fitting.

Point Spread Function : Moffat Profile

To correct for the effect of seeing the Fit-Galaxy code generates a Moffat profile star image (Moffat 1969) of a given full-width half-maximum (FWHM) expressed in terms of $\sigma_{PSF} = PSF_{FWHM}/2.35$. This analytic profile (Equation 2.5) is thought to represent the overall PSF shape better than a pure Gaussian which only approximates the core regions. Fit-Galaxy lets σ_{PSF} be a free fitting parameter to allow for any small changes in the PSF between the position of the star and the galaxy position.

$$PSF(r) = const/[1 + (r/\alpha)^2]^{\beta} \tag{2.5}$$

Here α represents the width of the PSF and is related to the $FWHM = 2\alpha\sqrt{2^{1/\beta} - 1}$ (Trujillo et al. 2001). β governs how peaky the PSF profile (the larger β is the more Gaussian-like the profile becomes) is. The standard value used for β is 2.5. The α parameter can be fine-tuned to a particular data-set using the average FWHM for the data (c.f. Chapter 5).

Minimization Technique : Powell's Method

The code requires explicit initialization of the fitting parameters. The initial value of the B/T ratio is always kept at 0.5 to ensure that the fitting procedure always has an equal chance of spanning either of the B/T intervals. The position angles of the disk and bulge components, their characteristic radii and the disk inclination angle are calculated from the image directly. The parameter limits between which the fitting is done are set in the code directly and fitting outside these limits is not possible.

The χ^2 is minimized in a 13-parameter space with seeing being the additional fitting parameter compared to Gim2D. The minimization routine is somewhat dif-

ferent from the one Gim2D uses. Whilst in the latter code every parameter is varied at each step according to the 'temperature' of the fit, in the case of Fit-Galaxy the minimization technique allows only one parameter to be minimized at a time i.e. all but one parameter will be 'frozen' until a minimum for this parameter is found and the process will be repeated for the whole set of parameters until the global minimum is found - the essence of Powell's method (Press et al. 1992). At any particular stage the method keeps track of six function points a, b, u, v, w and x where a, b define the limits between which the parameter is allowed to be fit, x is the very least functional value found so far, w is the point with the second least function value, v is the previous value of w and u is the point at which the function was evaluated most recently. The method uses parabolic interpolation, fitting through the points x, v and w. For a new minimum to be accepted, the parabolic step must (i) fall within (a, b) and (ii) imply a movement from the best current value x that is less than half the movement of the step before last. The method works well in finding a global extrema however, if the number of dimensions is large the search can be a very lengthy process and the method can also be sensitive to parameters being correlated. For a 91×91 pixel image the run time is typically several hours (N.B. if Monte Carlo realisations needed for the error analysis are to be performed the process can take up to several days for 30 realisations). Larger postage stamps are not feasible in terms of the computing time and the means of tackling this problem will be discussed later in Chapter 5.

Fit-Galaxy Outputs

After the convergence is achieved, the best-fit parameters are output into a file as well as the best-fit model image and the residual map obtained by subtracting the model galaxy from the real image and the value of χ^2_ν calculated. Errors on the fitted parameters are obtained using a Monte Carlo approach : the best fitting model for each galaxy is used to create 30 realisations of the model (with random noise added). After the best-fitting parameters are found for each of the model realisations their distribution is used to estimate the uncertainty in the fit.

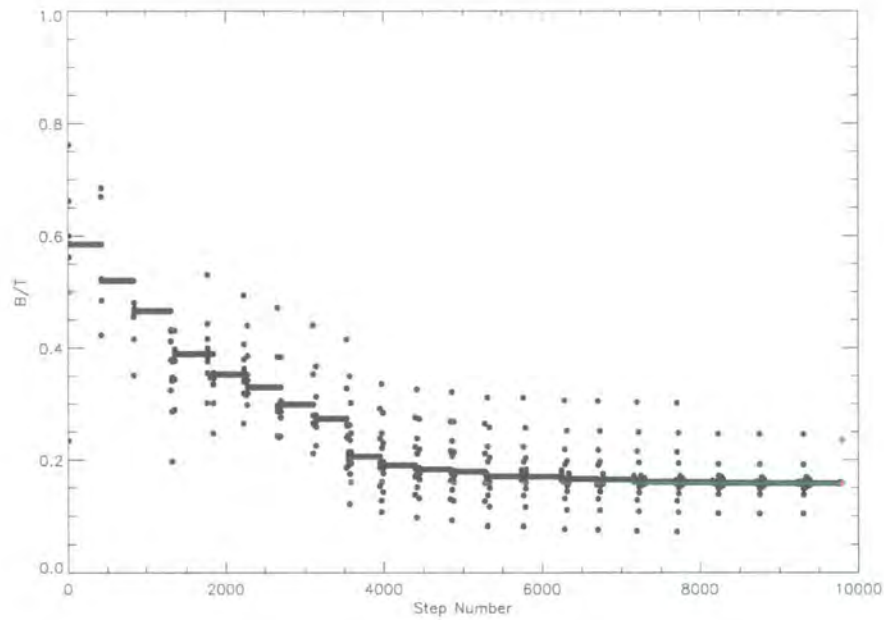

Figure 2.4: Figure illustrates B/T search using Powell's method. The initial B/T is always set to be equal to 0.5 (red dot at 0). Perturbations around this value are tried and are accepted if the trial perturbation has a smaller value of χ^2 (black dots). Points that indicate a constant B/T correspond to the iterations of other fitting parameters. Eventually the search has converged to B/T= 0.19 (red dot at 9750). This model galaxy has $B/T_{true} = 0.234$ (green dot).

2.3 Gim2D vs Fit-Galaxy Comparison

2.3.1 Introduction

The previous section described two independent techniques (codes) for estimating the basic galaxy structural parameters such as their B/T ratios. Although these methods use the same analytic surface brightness profiles to fit the bulge and disk components, the subtle differences in the fitting parameters and the minimization techniques they use are sufficiently different to make their comparison interesting and important.

Before the code comparison is tackled the following differences need to be emphasized :

- both codes assume $n = 4$ to be fixed i.e. the Sérsic index n is not fit for,
- the sky background is always kept fixed when using Gim2D however Gim2D is allowed to recompute and therefore correct the background level before the minimization is started,
- the Fit-Galaxy code always treats the sky background as a free parameter,
- the ellipticities are different : in Gim2D fits $e = 1 - b/a$ whilst Fit-Galaxy fits a/b,
- the seeing is fixed in Gim2D but Fit-Galaxy lets it fluctuate between $\pm 5\%$ of the specified σ_{PSF},
- the position angles in Gim2D are defined with respect to the y-axis of a Cartesian system unlike the Fit-Galaxy code which defines them clockwise from the x-axis (the position angles of bulge and disk components are allowed to vary by both codes since a large difference between these can be a signature of barred structures (Simard et al. 2002)), and,
- the last point to be emphasized is that Gim2D has a much shorter run-time than Fit-Galaxy (approximately 10 times faster).

To quantify the performance of these codes a series of tests were conducted as described in the following text.

2.3.2 Tests : Model Galaxies I

Both codes have a useful feature of an in-built model galaxy making algorithm but for comparison reasons it is important to make them fit the same set of model galaxies. The initial tests and the code-comparison will be done using model galaxies 'internally' created using the Fit-Galaxy code.

A model galaxy, with its parameters chosen at random but between realistic limits (c.f. Table 2.2), is created by matching the total counts measured in a typical real galaxy (c.f. Chapter 5). Poisson noise is added to the model galaxy after it has been convolved with an analytic Moffat PSF of a 'typical' seeing which is subsequently used in the Gim2D PSF deconvolution. The model galaxy can then be fed into both codes as if it were a real one and, since the input parameters for each model galaxy are known, a comparison with the output best-fit values can be made.

Table 2.2: Model Galaxy Parameters.

Parameter	Low Limit	High Limit
B/T	0.0	1.0
$r_{e,d}$ (pixels)	1	12
e_b	0.0	0.8
i (degrees)	0.0	90.0
$PA_{b,d}$ (degrees)	0.0	180.0
FWHM (")	1.4	1.4

Figure 2.5 shows a good recovery of the input B/T ratios by Gim2D and Figure 2.6 demonstrates a good internal consistency of the Fit-Galaxy code in the recovery of the B/T ratios. The figures provide an initial estimate of how well the two codes compare for a set of model galaxies and suggest that both codes (in the case of 100

model galaxies internally created using Fit-Galaxy) recover the input B/T ratios well with the B/T scatter of $\sigma_{rms} \sim 0.10$. The remaining parameter correlations are shown in Figures 2.7 and 2.8.

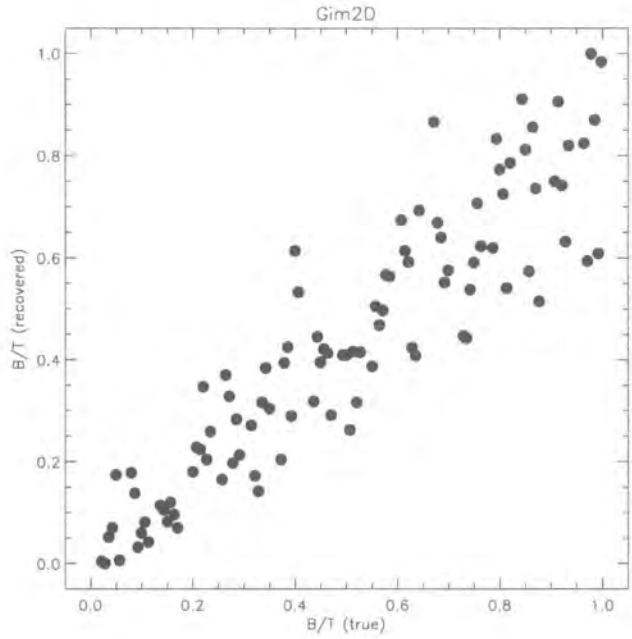

Figure 2.5: Figure demonstrates a good correlation between the input B/T ratios for 100 model galaxies and the best-fit recovered B/T ratios recovered using Gim2D with $\sigma_{rms} = 0.10$. Note that there is an apparent tail-down at high input B/T ratios. After inspection of other model parameters it is found that the characteristic radii of these galaxies are the largest. Also the sky background recomputed by Gim2D for these galaxies is highest and it appears that in these fits the extended surface brightness was 'swapped' for the background.

The next test to be performed is to let both codes fit 'externally' created model galaxies to avoid any in-built biases but also to run the tests on a more realistic data.

2.3.3 Tests : Model Galaxies II

Results from the previous section demonstrate that both Gim2D and Fit-Galaxy codes lead to a reliable 2-dimensional decomposition for a set of 'in-code' built

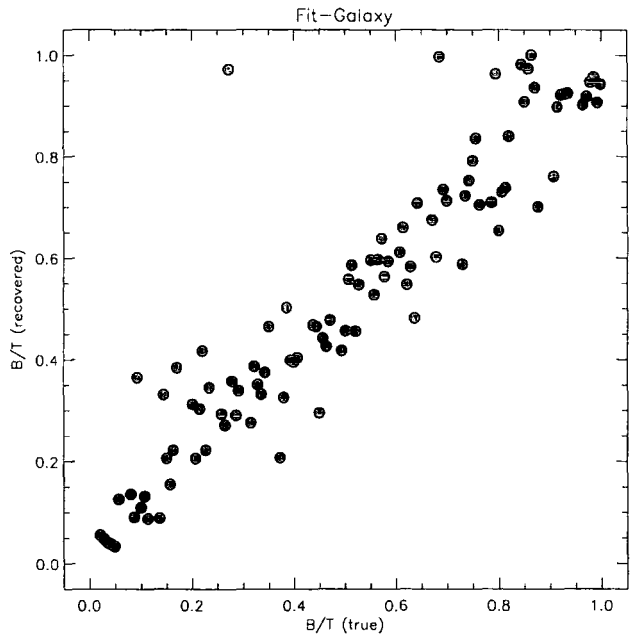

Figure 2.6: The figure demonstrates a good correlation between the input B/T ratios for 100 model galaxies and the best-fit recovered B/T ratios recovered using Fit-Galaxy with $\sigma_{rms} = 0.11$ and demonstrates a good internal consistency.

model galaxies. However, the crucial test to be performed is to run both codes on data which has been modelled in such a way that it resembles real data as closely as possible.

Model galaxies were therefore externally created using the IRAF task MKOBJ. The model galaxy parameters are taken from Table 2.2 and a model galaxy is created of a user-specified size, orientation and ellipticity (in this case defined as b/a) and is also convolved with the user-specified seeing (stellar image of a given FWHM created using MKOBJ). A useful feature of creating galaxies in this way is that a real science frame can be fed into MKOBJ and the model galaxy added to a blank patch of the sky on this science frame. This is the closest to mimicking the real data assuming that the noise characteristics are known and that the counts of a real galaxy within the frame can be measured (and matched). The model galaxies were created in the following way : several Sloan Digital Sky Survey (SDSS) r'-band science frames are taken each of which typically contains $\sim$ 5 SDSS catalogued galaxies. Each science frame is taken from a different patch of the sky (correspond-

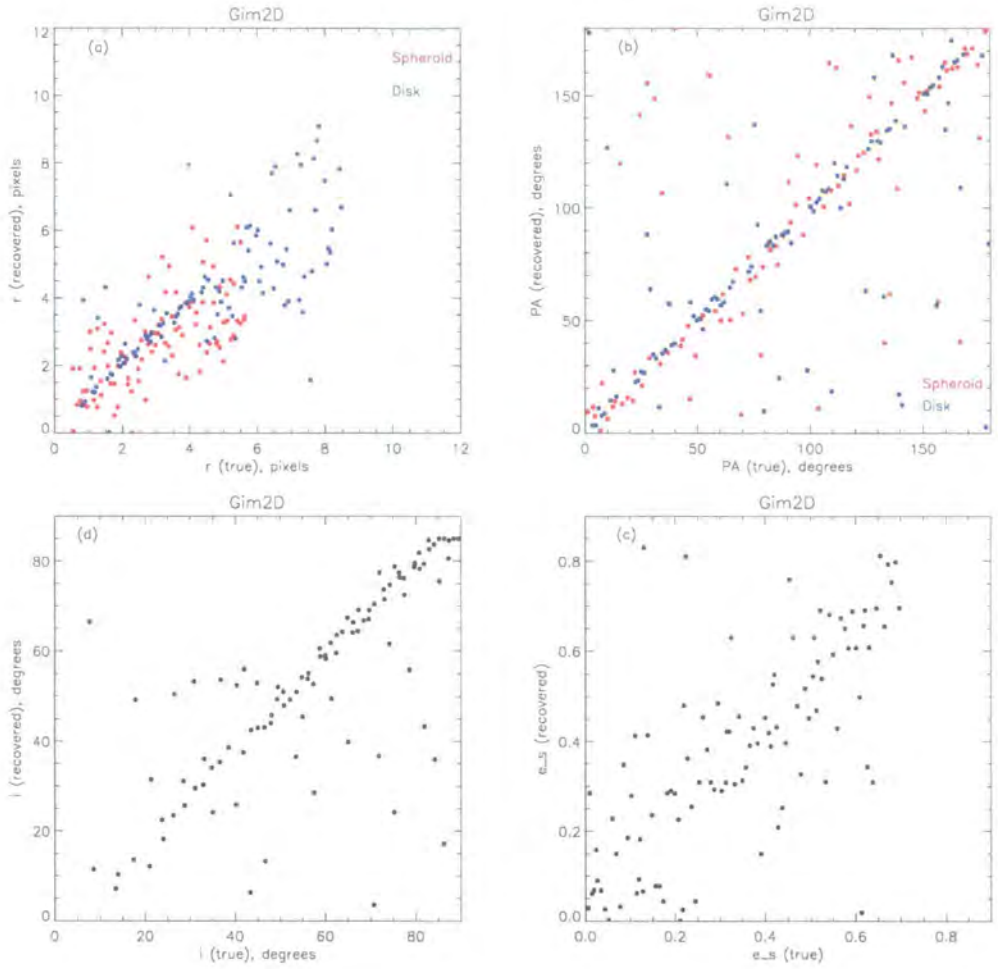

Figure 2.7: Clockwise from the top left-hand corner : correlations of the characteristic radii, position angles, inclination and ellipticity for 100 model galaxies created using the Fit-Galaxy code and decomposed using Gim2D. A feature to notice in (d) is the apparent saturation at $i = 85°$ which is the upper limit that Gim2D allows for the disk inclination. The remaining parameters correlate well although a large scatter is present.

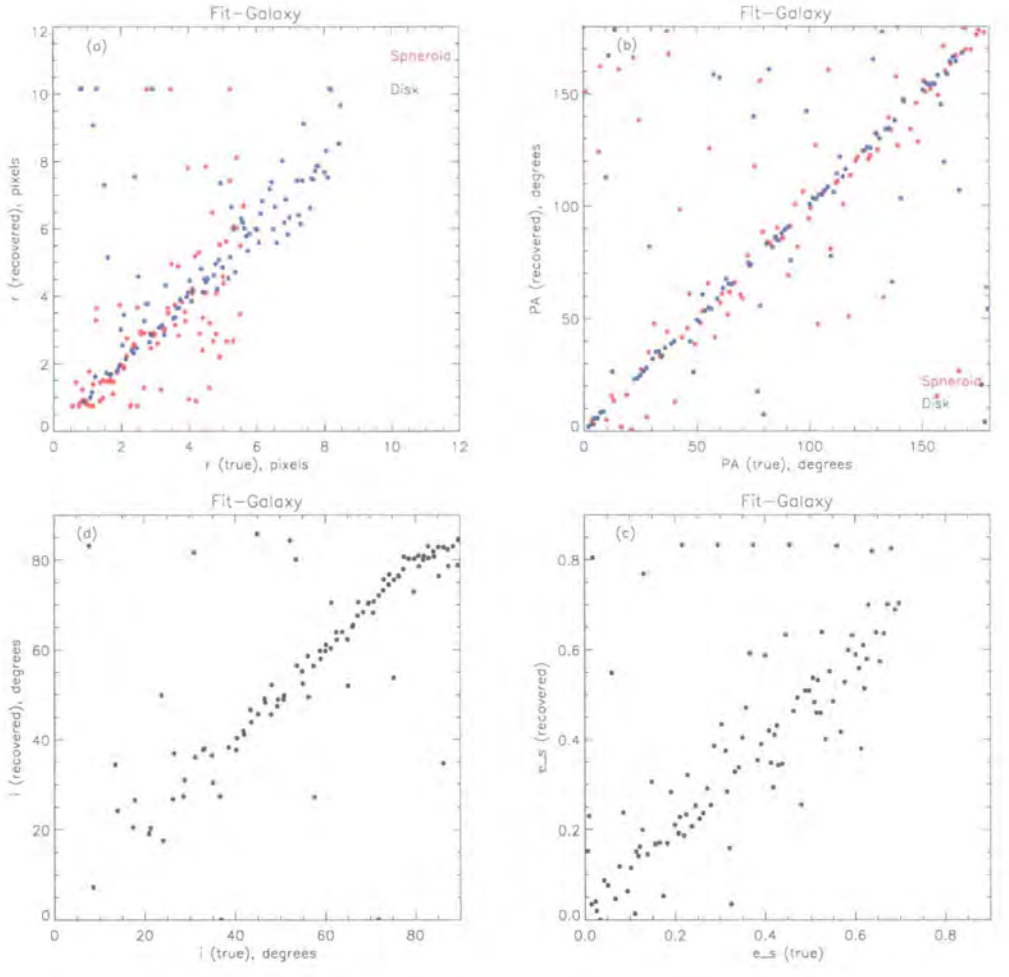

Figure 2.8: Clockwise from the top left-hand corner : correlations of the characteristic radii, position angles, inclination and ellipticity for a 100 model galaxies created and decomposed using the Fit-Galaxy code. The code seems to hit the upper limit on the characteristic radii when the input radii are very small or very large (a). Another feature to be discussed is the number of very elliptical bulges that appear to be found (c). Inspection of the input (and output) parameters leads to conclusion that these are common in galaxies which have very small bulge components. So if a presence of small bulge is detected it will appear highly flattened. The feature to notice in (d) is the apparent saturation at $i \sim 85°$. Even though the Fit-Galaxy code allows the disk to be fully inclined ($i = 90°$) the code appears to be biased away from this upper limit. This feature will be further discussed in Chapter 5.

ing to a different run number[‡]). Counts associated with the SDSS galaxies are measured using the SExtractor $flux_{best}$ parameter. The procedure is applied using galaxies which span a range of apparent magnitudes, making sure that they also appear to vary in shape and in size (this ensures that decompositions are reliable across the magnitude range covered by the SDSS sample). The IRAF task MKOBJ is then used to insert model galaxies across the blank regions of the sky in the original science frame. The postage-stamps for these galaxies are extracted from both the science and SExtractor frames and the decomposition codes run treating the extracted model galaxies as if they were real ones.

The results of the Gim2D decompositions of the model galaxies are shown in the Figure 2.9. The agreement between the input and the output B/T ratios for the pure exponential disks (B/T= 0) is excellent. However, the recovered input B/T ratio for B/T= 0.5 is biased by ΔB/T= 0.1 and for B/T= 1.0 galaxies the bias is ΔB/T= 0.2. The tendency is always to underestimate the amount of bulge or equally overestimate the disk component. Gim2D, as will be shown in Chapter 3, can be fine-tuned to recover the input B/T ratios at ΔB/T= 0.1 across the full B/T range. To do so Gim2D requires the size of the zone around the lowest SExtractor isophote used in the re-calibration of the sky background to be set to $\sim$ 30 pixels (the default value is set to 10 pixels). This ensures that any faint galaxy flux does not contribute to the re-calibrated background flux and therefore bias in the B/T.

The results of the Fit-Galaxy decompositions of the model galaxies are shown in Figure 2.10. For the pure exponential disks the recovered B/T ratios are very good. The tail-down in the recovered B/T ratio becomes noticeable for galaxies which have been created using exponential disk + $r^{1/4}$ law and peaks at B/T = 1.0, i.e. most pure $r^{1/4}$ galaxies have acquired a fictitious disk component. This has been tested as a function of the apparent magnitude and the input scale radii but there appears to be no correlation between these inputs and the output B/T ratios. There appears to be some correlation with the minor/major axis ratios : the

[‡]For a full discussion of the SDSS imaging and spectroscopic catalogued data and the SDSS sample selection criteria please refer to Chapter 5.

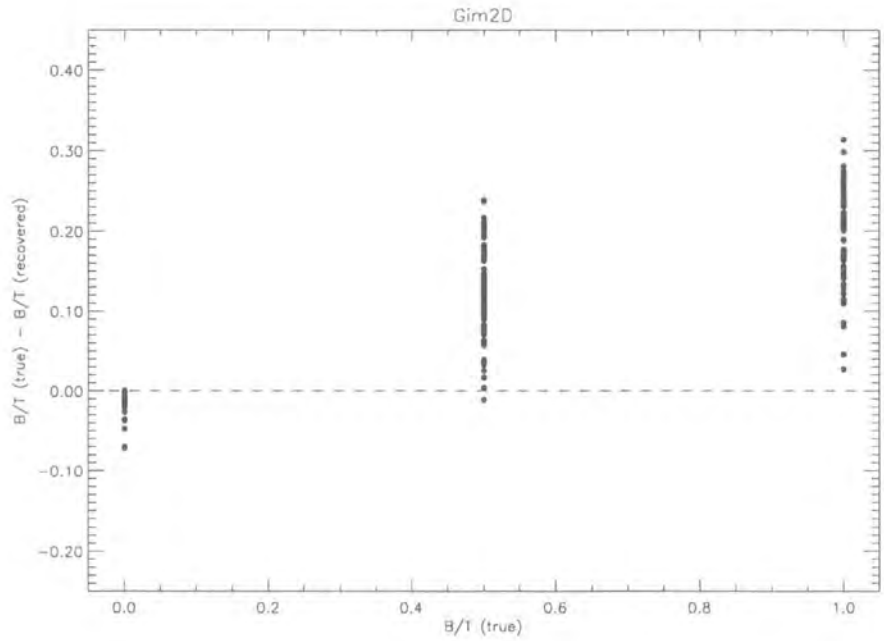

Figure 2.9: Figure demonstrates a reasonable correlation between the input (true) B/T ratios of a set of 250 model galaxies and the best-fit B/T ratios recovered using Gim2D. The recovered mean value offset for B/T= 0.0 is B/T= 0.02. For B/T= 0.5 the recovered mean value offset is B/T= 0.13 and for B/T= 1.0 is B/T= 0.20. Model galaxies span a range of apparent magnitudes, sizes and orientations.

B/T deviation is largest the more elliptical in appearance the galaxy profile looks. The most prominent correlation is between the output B/T ratio and the sky background. The Fit-Galaxy code, as previously mentioned, allows the sky background to fluctuate a little to allow for any uncertainties in the estimated background. The fact that the deviation between the input and the output B/T ratios is largest when the 'fitted' background is smallest implies that the extra disk component is found where in fact the extra counts were due to the sky background. Since there is no sharp cut-off for either of the empirical formalisms this means that 'at the galaxy edges' the surface brightness profile and the sky background are indistinguishable. However, the background remains to be treated as a free parameter in the future decompositions since the code does not offer any other way of correcting for the potential error in the estimate of the underlying background.

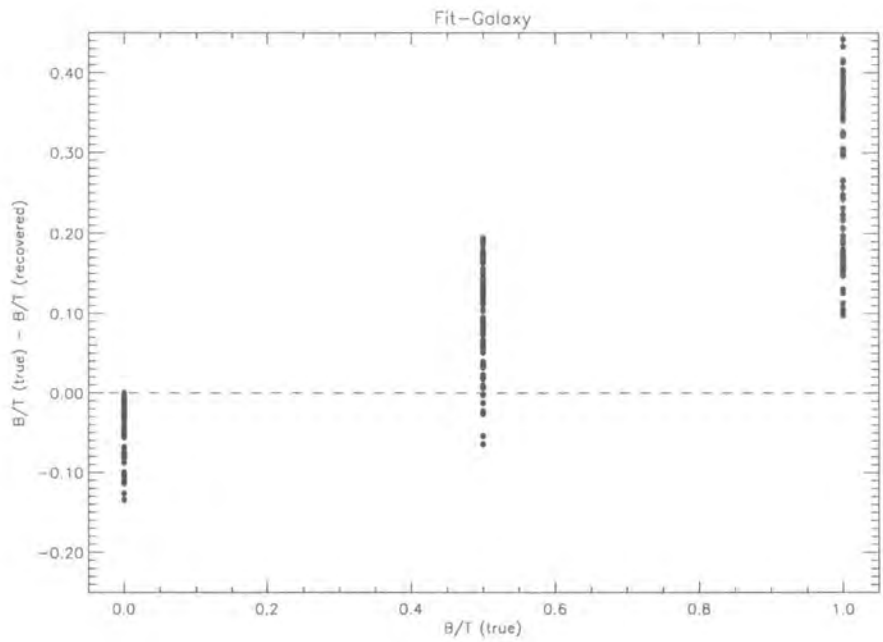

Figure 2.10: Figure demonstrates a reasonable correlation between the input (true) B/T ratios of a set of 250 model galaxies and the best-fit recovered B/T ratios recovered using Fit-Galaxy. The recovered mean value offset for B/T= 0.0 is B/T= 0.05. For B/T= 0.5 the recovered mean value offset is B/T= 0.11 and for B/T= 1.0 is B/T= 0.24. Model galaxies span a range of apparent magnitudes, sizes and orientations.

Gim2D performs marginally better than Fit-Galaxy in the recovery of the input

B/T ratios. However, both codes show similar biases in the overall decompositions. Their relative performance on a set of real galaxies is compared next. This allows a more realistic comparison of the codes using real data but of course there is no a priori correct answer for the recovered B/T ratios.

2.3.4 Tests : Real Galaxies

To enable the real-data comparison a set of SDSS galaxies already decomposed using the Fit-Galaxy code (Chapter 5) are used. This is because it is easier and many times faster to run Gim2D on the SDSS galaxies rather than Fit-Galaxy on the large nearby cluster galaxies decomposed using Gim2D. To ensure equal sampling of the [B/T, apparent magnitude] space the comparison is made on a sub-sample of the SDSS galaxies is selected in bins of 0.5 in apparent magnitude and in bins of 0.2 in B/T ratio. Unsaturated stellar images with a high S/N are extracted from the SDSS galaxy frames and are to be used in the Gim2D PSF deconvolution. The Fit-Galaxy Moffat PSF has been fine tuned to fit the SDSS data well (Chapter 5). Figure 2.11 demonstrates a significant correlation (Spearman rank correlation coefficient of 0.74) between B/T ratios for $\sim$ 350 SDSS galaxies obtained using the Gim2D and Fit-Galaxy codes and shows no systematic differences between the two codes with the remaining parameter correlations shown in Figure 2.12.

2.4 Summary and Conclusions

In this Chapter we have demonstrated that two independent codes, Gim2D and Fit-Galaxy, agree well in their recovery of B/T ratios for a set of model galaxies and real data. However, the model tests indicate similar small biases appear to be present in both codes with a tendency to underestimate the bulge component in galaxies which are mainly bulge-dominated.

In Chapters 3 and 4 Gim2D will be used to obtain quantitative measures of

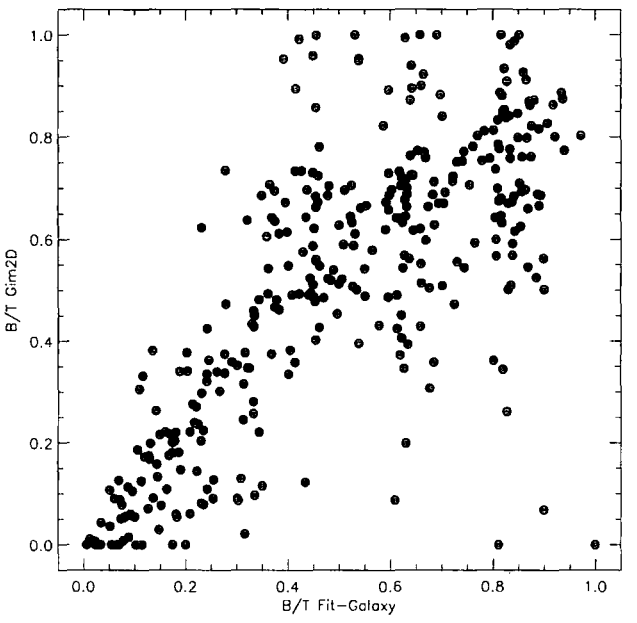

Figure 2.11: Figure shows a correlation between the B/T ratios of a set of 350 SDSS galaxies fit using both Gim2D and Fit-Galaxy. The Spearman rank correlation coefficient of 0.74 indicates a significant correlation. Note that hardly any pure bulges i.e. B/T=0.0 are detected by the Fit-Galaxy code but there appear to be a few detected by Gim2D. This is most likely due to bias in Fit-Galaxy. Most of these galaxies have bulge characteristic radii less than 2 pixels (and so does the only Fit-Galaxy detection at B/T=1.0). However, Gim2D detects these galaxies to have larger characteristic radii. There is a general tail-down in the B/T ratios recovered by Gim2D around $B/T = 1.0$. The scatter for the full sample is $\sigma_{rms} = 0.19$.

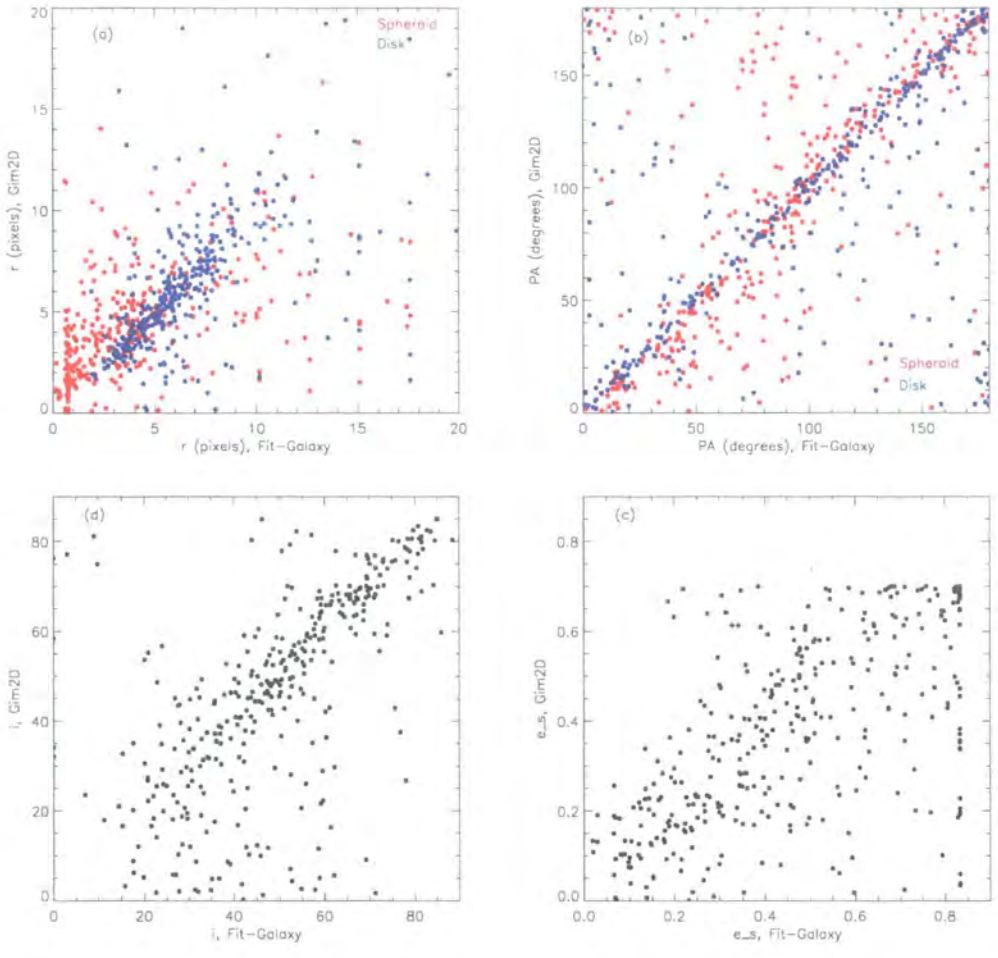

Figure 2.12: Correlation plots of various parameters between Gim2D and Fit-Galaxy codes. There appear to be no systematic differences in the recovered parameters although the scatter is large.

B/T ratios of galaxies in nearby and intermediate redshift clusters. The choice of the code is based upon the fact that the intermediate redshift cluster data were taken with the HST WFPC2 for which Gim2D was purposely written (Simard et al. 2002) but also because the nearby cluster galaxies are very big in the apparent size which makes them almost impossible (in terms of computing time) to be fit using the Fit-Galaxy code. Fit-Galaxy will be used to study the B/T ratios of field galaxies in Chapter 5 since this code has previously been used in a similar but much smaller study (Benson et al. 2002).

Chapter 3

Morphological Properties of Galaxies in Nearby Abell Clusters

In this Chapter the Gim2D code of Simard et al. (2002) is used to obtain quantitative measures of galaxy bulge-to-disk ratios for a sample of present-day ($z \sim 0.04$) cluster galaxies. The quantitative bulge and disk luminosities are used to test for the spiral to S0 evolution in galaxy clusters under assumption that the present-day distribution of spiral galaxies is a good representation of the spiral population believed to be responsible for producing the present-day cluster S0s. The aim of the study presented in this Chapter is to, using quantitative measures of bulge magnitudes, investigate the effect of disk fading of a sample of morphologically classified spiral galaxies to test whether the present-day disk-faded spirals are consistent with being responsible for producing the S0 population seen in the present-day clusters. Comments on the potential mechanisms driving the transformation are given at the end of the Chapter.

3.1 Introduction

Galaxy clusters are the largest and most massive objects in the Universe and are places where the extremes in galaxy evolution happen. Present-day galaxy clusters are mainly populated with elliptical and S0 galaxies (Oemler 1974). The fraction of cluster spirals (S) is found to increase with lookback time accompanied by a corresponding decrease in the fraction of cluster S0s (Dressler et al. 1997). This is

suggestive of some cluster-related process(es) responsible for the apparent spiral to S0 transformation which appears to have taken place between $z \sim 0.5$ and present.

One such transformation process which depends on the global galaxy environment is ram pressure stripping that was first investigated by Gunn & Gott (1972). A galaxy is stripped of its gas as it passes through the cluster if $\rho_e v^2 > 2\pi G \sigma_s \sigma_{ISM}$. The left-hand side of the equation represents the ram-pressure exerted by the external (intra-cluster, ICM) medium of density ρ_e with v being the galaxy velocity. The right-hand side corresponds to the mean force per unit area that holds the gas to the galactic plane, with σ_s and σ_{ISM} the mean surface mass density of stars and inter-stellar medium (ISM) respectively. Gisler (1979) investigated the effects and timescales of the ram pressure mechanism and concluded that if the gas injection rate from evolving stars is large enough a galaxy will be invulnerable to stripping for the largest proportion of its life but can be stripped quite rapidly once the star formation has ceased and the massive stars evolved. Solanes & Salvador-Sole (1992) showed that the morphological segregation between S and S0s observed in regular (relaxed) galaxy clusters is consistent with simulations of the ram pressure stripping effect. However, the principal evidence against the stripping hypothesis for the origin of S0s is the work of Dressler (1980b) who demonstrated that S0 galaxies in present-day clusters have substantially larger bulges than spirals that cannot be accounted for by a simple disk fading mechanism (supported by the similarity of the S and S0 luminosity functions). The main drawback of the Dressler (1980b) study lies in the fact that the bulge magnitudes were only based upon visual estimates.

In this Chapter we further investigate the effect of disk fading using quantitative methods of measuring bulge and disk magnitudes for a sample of Dressler (1980a) cluster galaxies. The bulge and disk magnitudes are inferred from the B/T ratios obtained using the Gim2D code of Simard et al. (2002).

3.2 Observations, Data Reduction and B/D Decompositions

3.2.1 Sample Selection

The clusters for this study were selected from the Dressler (1980a) nearby cluster catalogue with the selection mainly based upon the cluster visibility at the time of year the observations were made. The clusters were also selected to span a range of X-ray luminosities. If a transformation mechanism such as ram pressure stripping by the intracluster medium is of significant importance then a correlation between the galaxy B/T ratios and the corresponding cluster X-ray luminosity should be expected i.e. the X-ray luminous clusters should contain more spheroid dominated systems. A lack of correlation would suggest that local rather than global processes may be at work (Balogh et al. 2002).

3.2.2 Observational Overview

A sample of 13 nearby rich clusters of galaxies was observed in the Sloan Digital Sky Survey g-band. The data was taken using the Wide Field Camera (WFC) positioned at the prime focus of the 2.5m Isaac Newton Telescope, La Palma. The observations were undertaken during the period between January 14^{th} and January 18^{th} 2002. Each of the four WFC EEV CCDs is a 2048×4096 pixel array with the pixel scale of $0.333''$/pixel giving a total camera field of view of approximately $30' \times 30'$.

The photometric conditions and seeing throughout the observing run were variable. The first and second nights were mostly clear and 5 target clusters were observed each night. During the third night the weather conditions were non-photometric and only one principal target was observed - the Coma cluster - however the photometric calibration was still possible since Coma is a well observed cluster. During the fourth night the weather conditions were good for most of the night and further 4 clusters were observed.

Failure of the camera auto-guider several days prior to the observing run meant that the tracking of the telescope was not perfect. This problem manifested itself as elongated (sometimes even double) images of stars/galaxies in the direction of the tracking. To check for a potential tracking error the stellar images were examined as soon as the data was read-out and if any asymmetry was detected the observation was repeated. Only one of the target clusters (Abell 400) had to be fully rejected as the observations of this cluster showed severe tracking problems. The final homogeneous sample of 13 nearby clusters is summarised in Table 3.1.

Table 3.1: Nearby Cluster Sample. The X-ray luminosities are taken from Ledlow et al. (2003).

Cluster	RA	Dec	z	Band	T_{exp} (s)	$L_x \times 10^{43}$ ergs s^{-1}
A0168	01 15	+00 14	0.05	SDSS g	300	1.15
A0376	02 45	+36 51	0.05	SDSS g	300	1.91
A0496	04 33	-13 14	0.03	SDSS g	300	5.97
A0539	05 16	+06 27	0.03	SDSS g	300	N/A
A0592	07 42	+09 22	0.06	SDSS g	300	1.79
A0754	09 07	-09 48	0.05	SDSS g	300	8.48
A0978	10 20	-06 31	0.05	SDSS g	300	0.79
A1069	10 40	-08 35	0.06	SDSS g	300	1.40
A1185	11 10	+28 41	0.03	SDSS g	300	0.72
A1631	12 49	-15 52	0.05	SDSS g	300	0.70
A1644	12 53	-17 48	0.05	SDSS g	300	4.53
A1656	12 59	+27 57	0.02	SDSS g	300	9.18
A2634	23 38	+27 01	0.03	SDSS g	300	1.31

The cluster imaging was conducted using a 4-pointing dither pattern leading to a contiguous area of just under 1 degree square with a 10′ overlap in the centre to check the accuracy of the photometric and decomposition measurements (Section 3.2.9). Each of the dither pointings was further offset by 2″ to cover the gaps between the CCDs as demonstrated in Figure 3.1.

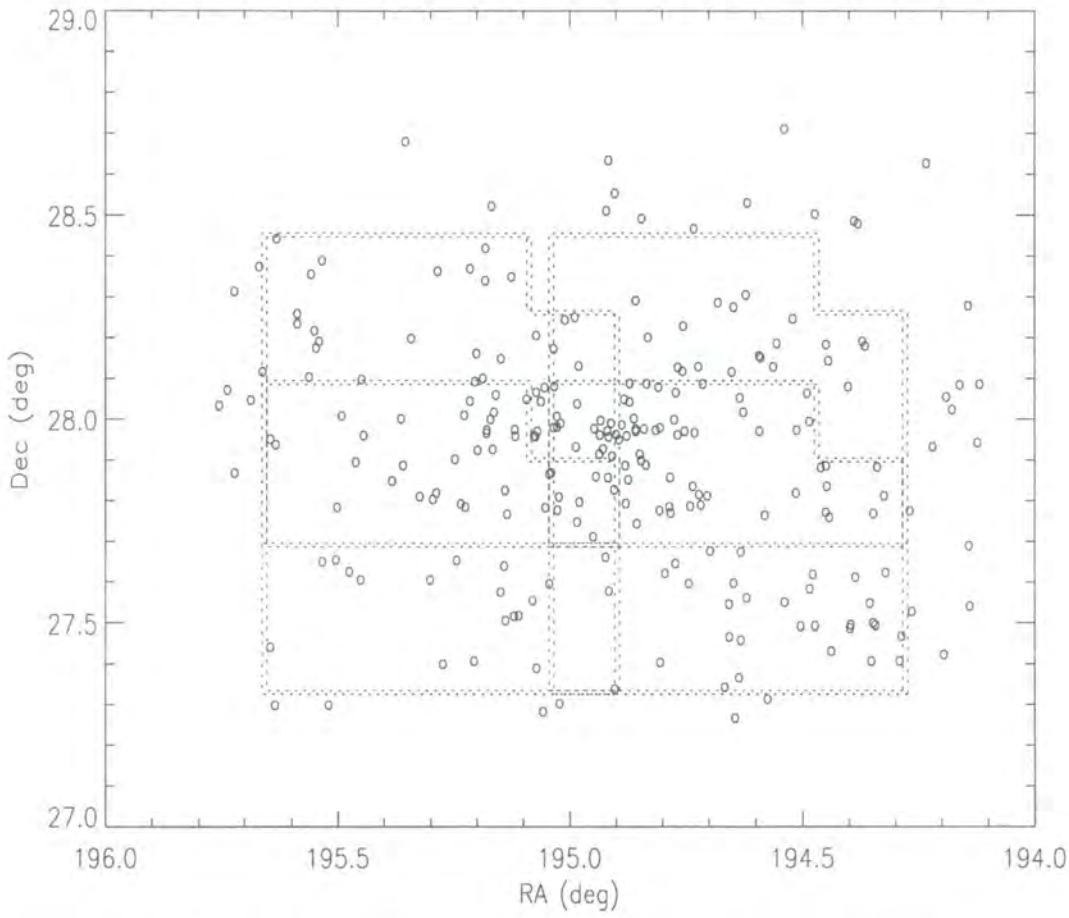

Figure 3.1: A map of the central region of the Coma cluster showing the location of Dressler (1980a) galaxies relative to the area imaged with the WFC. The dashed lines represent the WFC dither pointings and offsets. The total area surveyed is just under 1 degree square.

3.2.3 Data Reduction

CCDs convert the incoming source photons into electron counts and since no CCD is ideal internal electronic signatures will be present in the detected signal. If the observed data is to be used for scientific purposes these instrumental and other noise signatures must be corrected for.

De-biasing

Bias or zero exposure frames represent the intrinsic electronic signal associated with every CCD and should be removed prior to the scientific use of the data. Bias frames are usually taken are at the beginning and the end of each observing night. During the zero-exposure CCDs can pick up interference patterns caused by other electronic sources so all the individual exposures were inspected and rejected if they showed such patterns before the master bias frame is created. The level of the intrinsic electronic signal can also change during the course of the night. To correct for this potential change an artificial overscan region is added to all the data frames. To produce the master bias frame the overscan corrected individual bias frames are median combined using the IRAF task CCDPROC. The median bias frame is then subtracted off every observed data frame which is also overscan-corrected prior to the median bias subtraction.

Linearity Correction

The WFC CCDs suffer from significant non-linearities (most likely arising in the ADC electronics). The non-linearity correction (IRAF task IMCALC) is applied after the data is corrected for the bias. The correction is different for different chips and is determined from measurements taken in March 2000 summarized below* :

$$\mathrm{CCD}_1 = 1.0 \times \mathrm{value} - 2.0E-06 \times \mathrm{value}^2 + 8.0E-12 \times \mathrm{value}^3 \quad (3.1)$$

$$\mathrm{CCD}_2 = 1.0 \times \mathrm{value} - 0.5E-07 \times \mathrm{value}^2 - 4.0E-12 \times \mathrm{value}^3 \quad (3.2)$$

$$\mathrm{CCD}_3 = 1.0 \times \mathrm{value} - 6.0E-07 \times \mathrm{value}^2 \quad (3.3)$$

$$\mathrm{CCD}_4 = 1.0 \times \mathrm{value} - 1.5E-07 \times \mathrm{value}^2 - 2.0E-12 \times \mathrm{value}^3 \quad (3.4)$$

*The measurements are available from http://www.ast.cam.ac.uk/wfcsur/.

Flat-fielding

To enable a correction for the pixel-to-pixel variation in sensitivity, the data frames are usually divided by an image of a uniform source of illumination such as the twilight sky. Several twilight sky exposures were taken at the beginning and the end of every observing night. These were combined to produce a master sky frame which was then used to flat-field the data. This procedure was followed for the nights 1 and 4. Due to poor weather conditions at the beginning and the end of the observing nights 2 and 3 the median sky flat for these nights was constructed by combining the sky frames observed in the nights 1 and 4. After the flat-fielding CCD_3 was shown to suffer from severe vignetting in the lower left-hand corner and any data (partially) detected in this region was excluded from the subsequent analysis.

Photometric Calibration

To enable the target observations to be placed onto a standard photometric system several standard star fields of Landolt (1993) were observed during each night. Typically $10-15$ standard stars were found within the WFC field of view and their accurate photometry was used to zero-point the target observations.

The standard star instrumental magnitudes were measured by performing aperture photometry using the IRAF task PHOT. The instrumental magnitude, m_{inst}, represents the total counts measured in a given aperture using some arbitrary zero-point (ZP) and is related to the apparent magnitude, m, as given in Equation 3.5 below :

$$m = m_{inst} + E(B-V) + C\sec(z) \tag{3.5}$$

where C is the atmospheric extinction and $sec(z) = airmass - 1$ with $airmass$ being a quantity measured at the time of the observation. The value of the atmospheric extinction for a given night is inferred form the slope of m_{inst} vs $sec(z)$ plot shown in Figure 3.2. The colour transformation of Fukugita et al. (1996) was used to relate the standard-star Landolt V-band magnitude to the WFC g-band

magnitude (Equation 3.6) thus enabling their direct comparison with the magnitudes obtained from the aperture photometry. The zero-points were estimated by interpolating the linear fit (solid line) of the standard star magnitudes as a function of time shown in Figures 3.3, 3.4 and 3.5.

$$g = V + 0.56(B - V) - 0.12 \tag{3.6}$$

Despite the weather appearing to be clear the large seeing variation throughout the observing run (FWHM 1″ to 3″) was indicative of rather unstable observing conditions. During a given observing night the zero-point typically changed by less than 0.2 magnitude making the observations of sufficient photometric quality for the proposed analysis. The mean zero points for all clusters but Coma are listed in Table 3.2. The Coma cluster photometry was zero-pointed using Johnson R-band 20″ diameter aperture magnitudes of galaxies supplied by Dr. John Lucey (private communication).

Table 3.2: The mean zero-point values for each of the target clusters.

Cluster	Night	ZP:CCD1	ZP:CCD2	ZP:CCD3	ZP:CCD4
A0376	1	30.92	31.10	31.13	31.13
A0539	1	30.91	31.08	31.11	31.11
A0754	1	30.88	31.03	31.07	31.07
A0978	1	30.91	31.05	31.09	31.09
A1631	1	30.88	31.01	31.05	31.04
A0496	2	30.93	31.08	31.12	31.12
A0592	2	30.96	31.12	31.19	31.16
A1069	2	30.93	31.08	31.18	31.11
A1644	2	30.89	31.04	31.16	31.07
A2634	2	30.94	31.10	31.11	31.14
A1185	4	30.89	31.08	31.13	31.13
A0168	4	30.99	31.12	31.13	31.18

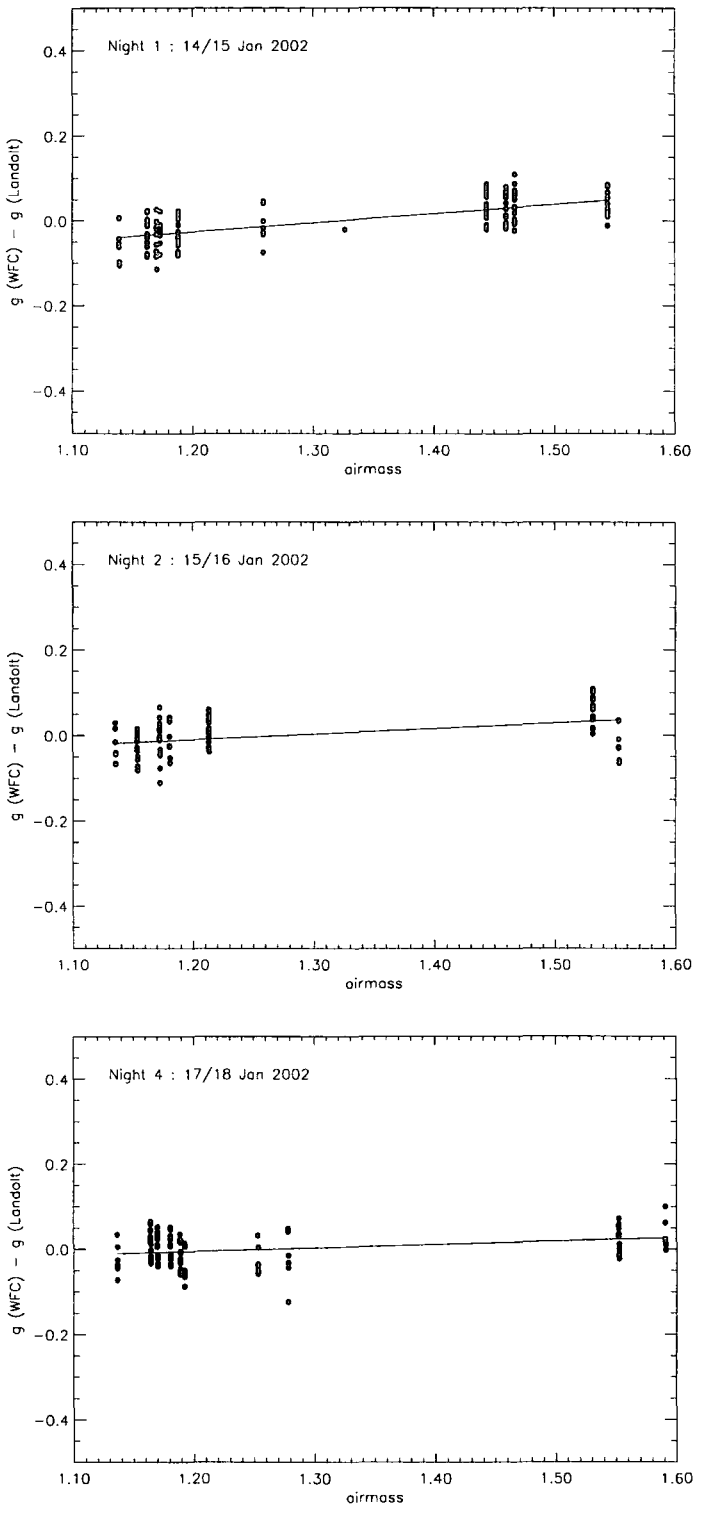

Figure 3.2: The atmospheric extinction estimation. A linear fit to the stellar aperture photometry as a function of *airmass* is performed to enable the extinction correction C to be determined for a given observing night.

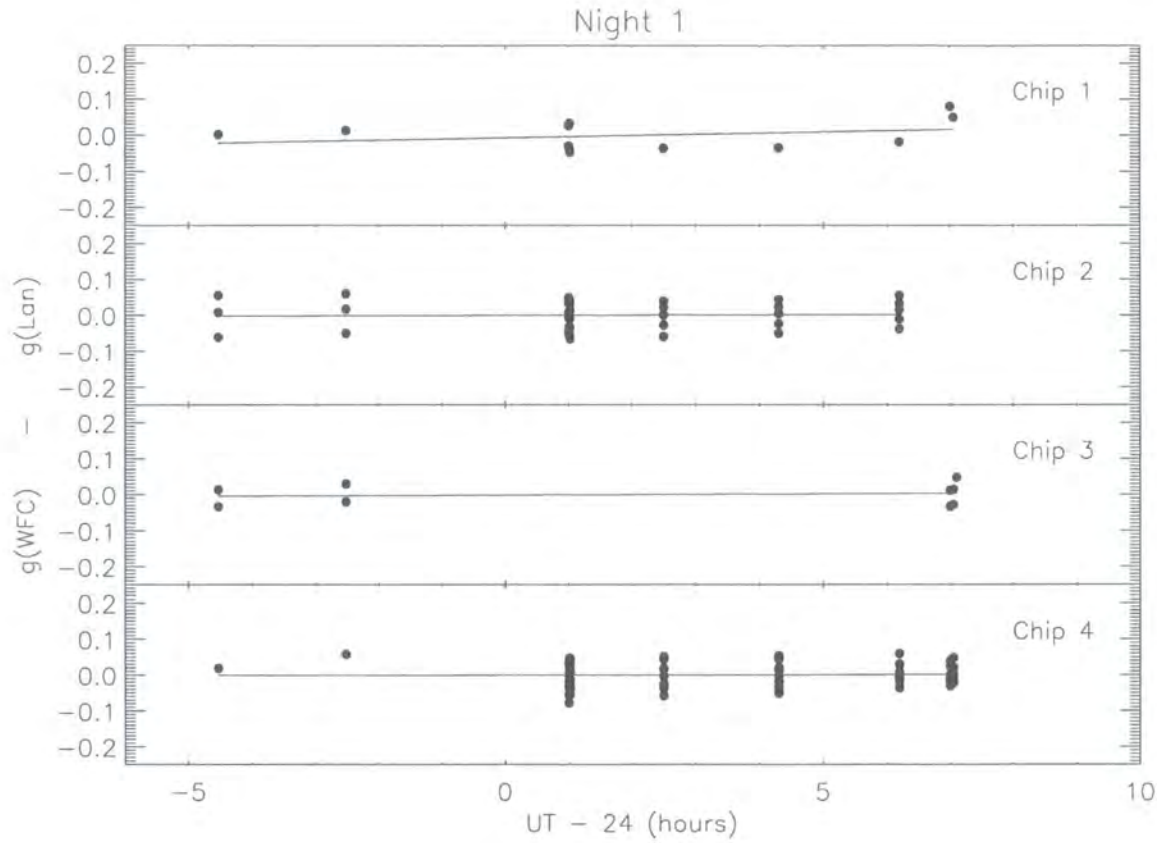

Figure 3.3: The magnitude zero-point offset for the Night 1. The solid line represents the linear fit to the (extinction corrected) standard star photometry as a function of time. The linear fit is used to interpolate the ZP offset characteristic for a given time of observation. Note that the CCDs have slightly different zero-points.

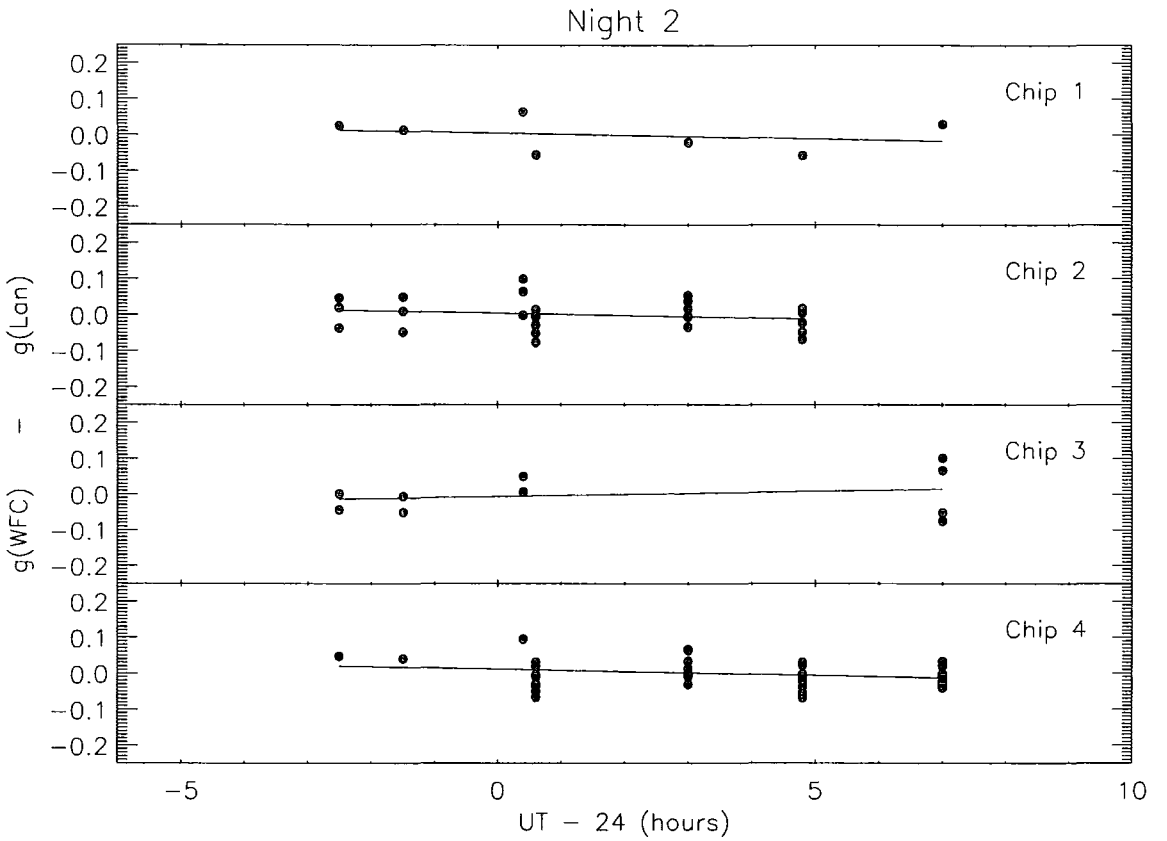

Figure 3.4: The magnitude zero-point offset for the Night 2. The solid line represents the linear fit to the (extinction corrected) standard star photometry as a function of time. The linear fit is used to interpolate the ZP offset characteristic for a given time of observation. Note that the CCDs have slightly different zero-points.

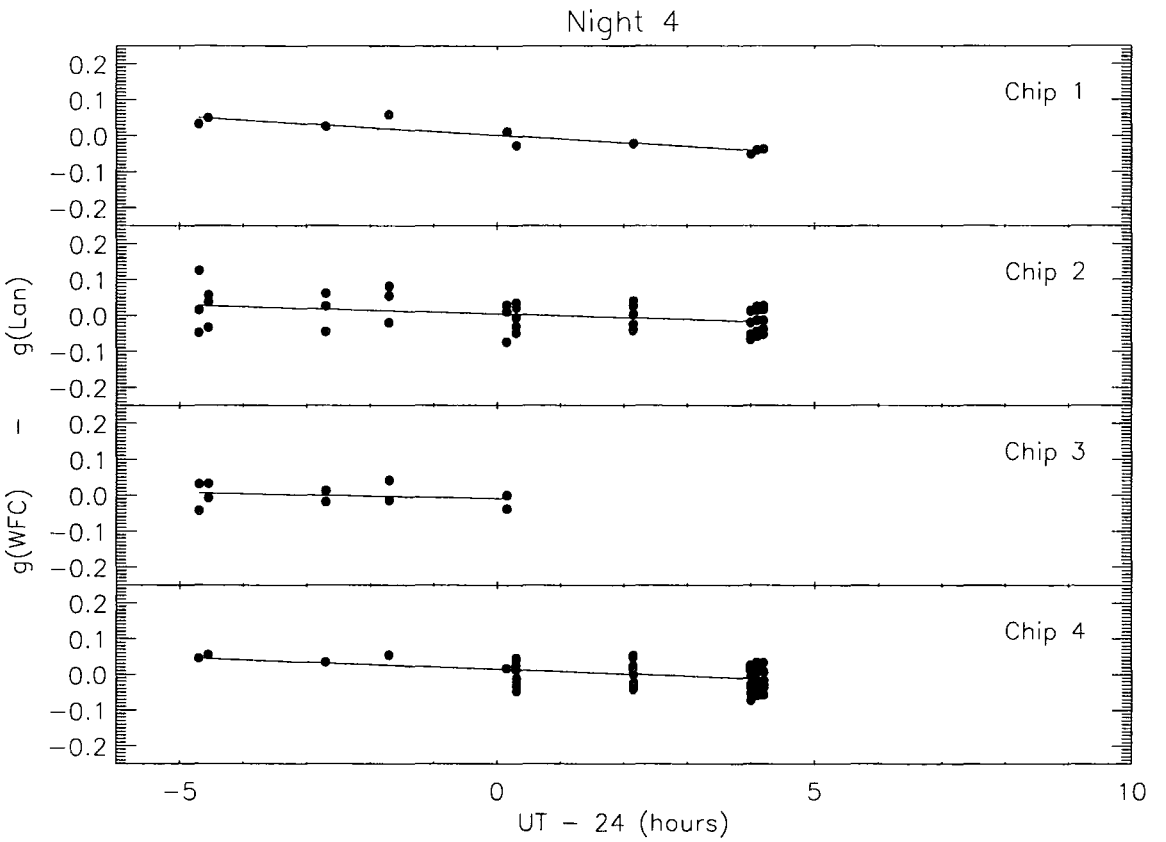

Figure 3.5: The magnitude zero-point offset for the Night 4. The solid line represents the linear fit to the (extinction corrected) standard star photometry as a function of time. The linear fit is used to interpolate the ZP offset characteristic for a given time of observation. Note that the CCDs have slightly different zero-points.

3.2.4 Object Detection and B/T Decompositions

The detection of objects in a given WFC frame was done using the SExtractor v.2.2.2 software (Bertin & Arnouts 1996). SExtractor employs a detection algorithm which deals very efficiently with overlapping objects - a useful feature when dealing with crowded nearby cluster fields. Deblending is seen as a compromise between splitting a single non-blended object into multiple detections and, in case of blended objects, not detecting the overlapping object at all. Deblending in SExtractor is governed through two parameters: $deblend_{nthreshold}$, the number of subthresholds (or branches) into which each object can be divided, and $deblend_{mincont}$, the minimum contrast between the neighbouring regions. After conducting a few trial runs the values of 32 and 0.001 were chosen for $deblend_{nthreshold}$ and $deblend_{mincont}$ respectively. The object detection limit above the sky background is set using the $detect_{threshold}$ parameter. $detect_{threshold} = 3\sigma$ above the LOCAL sky background is estimated to be a reasonable object detection limit and the minimum number of connecting pixels that trigger the detection is set to be $detect_{minarea} = 5$. To distinguish whether a detected object is a star or an extended source SExtractor uses the $class_{star}$ parameter. A low value of this parameter is indicative of an extended object and $class_{star} < 0.03$ was used to confirm that the detected object is indeed a galaxy. The SExtractor mag_{best} parameter was used to measure the total magnitudes for all the detected objects and a 20″ diameter aperture was used to obtain the corresponding aperture magnitudes.

The observed cluster frames were run through SExtractor to produce catalogues of detected object centroid positions, world coordinates, magnitudes, isophotal areas and star-galaxy classification parameters. The centroid positions and world coordinates were used to identify the objects detected by SExtractor with the Dressler (1980a) cluster galaxies. A measure of the galaxy isophotal area is required since Gim2D uses this value to set the size of the postage-stamp prior to decomposition (as explained in Chapter 2). SExtractor also produces a two-dimensional map of all the objects it detects in the form of a segmentation image. The segmentation image is used to obtain the object mask required by Gim2D since pixels that belong to the

same object are flagged with the same integer number in the segmentation image. The background pixels are flagged with a 0 and SExtractor uses these in computing the mean sky background level. Gim2D subtracts this value from the galaxy postage-stamp image to ensure the underlying background level is ~ 0 (Chapter 2) after which it performs the decompositions. Again, as discussed in Chapter 2, a high signal-to-noise unsaturated stellar image is extracted from every WFC frame to be used in the Gim2D PSF de-convolution of galaxies found on the same frame.

3.2.5 Gim2D Tests

In Chapter 2 the performance of the B/T decomposition code Gim2D of Simard et al. (2002) was tested using a set of model galaxies. The tests were conducted using a sample of model galaxies whose counts matched the counts of a field galaxy sample and whose sizes reflected the typical field galaxy sizes. Since the nearby cluster galaxies are much bigger and brighter this needs to be reflected in the test galaxy modelling. As described in Chapter 2, Gim2D relies upon the SExtractor masks to distinguish between the pixels that belong to a galaxy and those that belong to the background and uses the last detected isophote as a boundary between the two. However, Gim2D contains a useful feature which allows the pixels just outside the last isophote (defined as an annulus of a given number of pixels) to be excluded in case these pixels are still contaminated by the galaxy light. For large cluster galaxies several trial B/T decompositions of the model galaxies showed that by setting this 'buffer' zone to 30 pixels most of the potential contamination of the sky-background by the galaxy light is avoided. When the buffer zone is set to a smaller number of pixels the sky background computed by Gim2D is overestimated leading to an underestimate of the galaxy flux and thus to a lower recovered B/T with respect to the true value. If the zone is set to an even larger value, the number of pixels belonging to the background relative to the overall postage-stamp size would be reduced (bearing in mind that the galaxies are large so their postage-stamps need to be kept as small as possible to reduce the computing time). This will lead to an incorrect estimate of the sky background and a poor recovery of the B/T ratio. For

galaxies that belong to crowded regions, the SExtractor background estimates of the sky background also tend to be slightly higher than the average values for the frame. Recomputing the mean background level in Gim2D brings the background back close to the nominal value.

Gim2D : Model Tests Revisited

The results of the decompositions applied to model galaxies of various B/T ratios and spanning a range of magnitudes appropriate to this nearby cluster survey are shown in Figure 3.6. The model galaxies were created using the IRAF task MKOBJ in the manner described in Chapter 2 but with the PSF convolution done using a real stellar image extracted from the given science frame. For the modelling, several science frames were used each of which had a slightly different PSF and was taken at a different telescope pointing. The tests indicate that there is no systematic trend in the recovered B/T ratios with apparent magnitude.

3.2.6 Astrometry

The astrometric solution for the cluster frames was obtained using the Starlink software GAIA. GAIA enables external (NED[†]) and local positional catalogues of objects to be loaded up and plotted over a given science frame. GAIA also allows the individual catalogued object positions to be manually changed so that interactive matching can be achieved. The final astrometric calibration for each of our cluster frames is obtained by manual matching the positions of USNO stars. GAIA updates the FITS headers as soon as the astrometric plate solution is found - in this case the solution is found to be typically better than 5 pixels = 1.65″ - sufficient for the bright galaxy matching proposed here.

[†]NASA Extra-galactic Database.

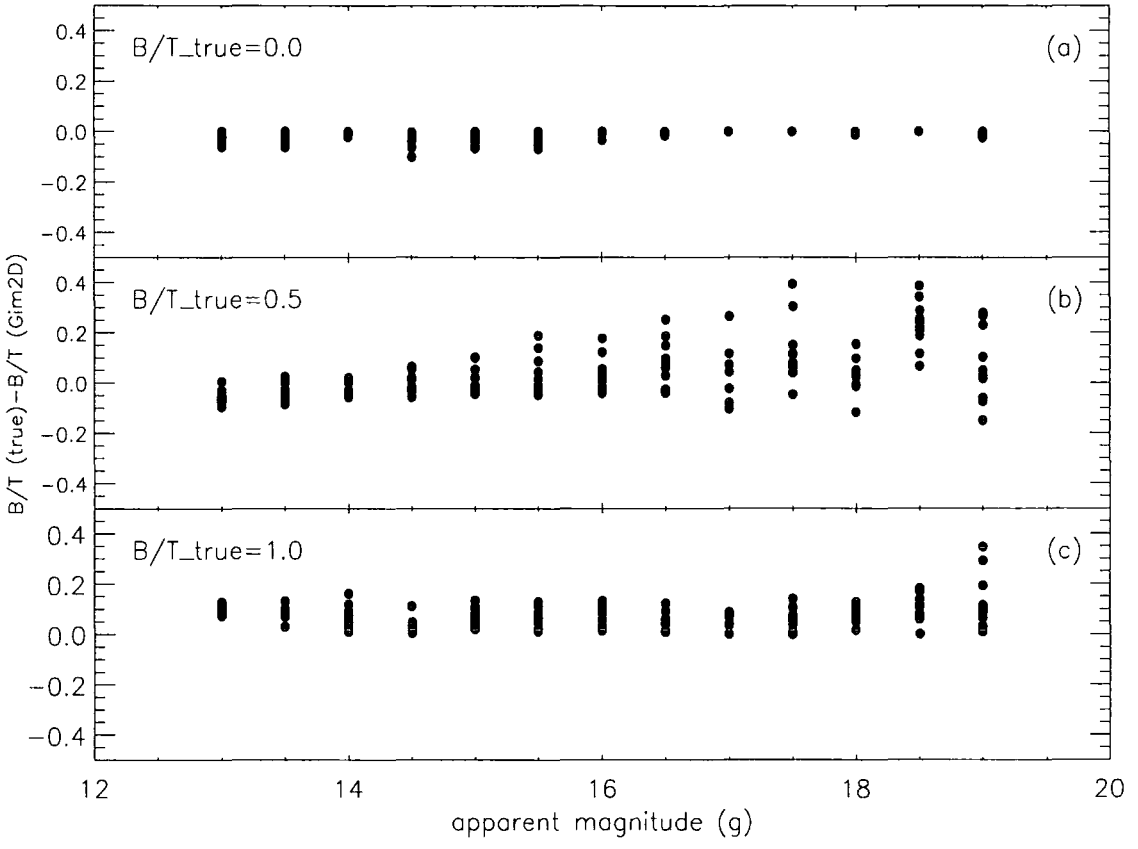

Figure 3.6: The recovery of the input B/T ratio for a set of model galaxies as a function of apparent magnitudes. The model galaxies were created using the method described in Chapter 2. (a) $B/T_{true} = 0.0$, (b) $B/T_{true} = 0.5$ and (c) $B/T_{true} = 1.0$. The figures demonstrate that there is no systematic trend in the recovered B/T ratios with apparent magnitude.

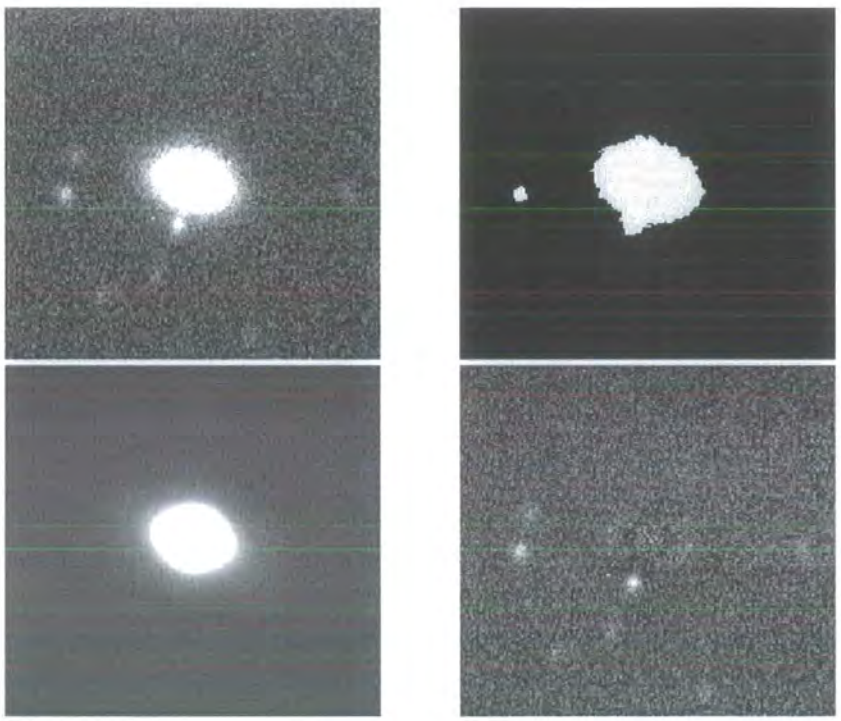

Figure 3.7: An example fit, this galaxy has B/T= 0.5. Shown are : (a) top left : the real galaxy postage stamp image, (b) top right : the segmentation mask, (c) bottom left : the model galaxy created using the best fit values and (d) bottom right : the residual postage stamp obtained by subtracting the model galaxy from the real galaxy image. The reduced $\chi^2_\nu = 1.06$ and the residual image is noise dominated and are indicative of a good fit.

3.2.7 Final WFC Catalogue Outputs

The morphological catalogues of Dressler (1980a) (hereafter D80) suffer from large astrometric errors[‡]. To correct for any astrometric errors in the D80 catalogues GAIA was used to manually match the positions that showed a large offset from the underlying galaxy. Because D80 catalogues contain mainly bright galaxies this process of astrometric correction is relatively safe and straightforward. Each of the catalogues was therefore updated and from now on these are referred to as the WFC D80 catalogues. The matching of the D80 galaxies with SExtractor objects was done using a 5″ tolerance to produce the final output WFC D80 catalogues. The multiple detections (arising from the observations taken in the dithering mode) were averaged over to produce the final catalogue entries for such objects.

3.2.8 Excluded WFC Catalogue Entries

The matched galaxies which were not decomposed due to their centroid position being too close to the chip edge were tagged and are excluded from any subsequent analysis. Also excluded are galaxies which were decomposed but whose underlying surface brightness profile did not appear to be well represented by a combination of a $r^{1/4}$ bulge and an exponential disk as reflected in the χ^2_ν being greater than 2.0 (c.f. Chapter 2).

Sometimes, due to severe overcrowding, the deblending by SExtractor can be very poor. Changing the SExtractor deblending parameter values in most of these cases does not improve the actual deblending and such galaxies were tagged and are excluded from the further analysis. Galaxies which were found to be severely contaminated by other objects such as foreground saturated stars are also excluded from the study. The total number of galaxies excluded is just under 10%.

[‡]D80 are in fact D80 J2000 since the galaxy coordinates have been corrected to J2000.

3.2.9 Galaxy Magnitudes and B/T Ratios

The final WFC catalogue for 13 nearby clusters contains 974 galaxies with g-band photometry and quantitatively measured B/T ratios. The distribution of their apparent magnitudes is plotted in Figure 3.8 and suggests that the sample is complete to $g = 17.0$ magnitude. In the subsequent study $g = 17.0$ is adopted as the magnitude limit for the sample reducing the sample size to 804 galaxies in total.

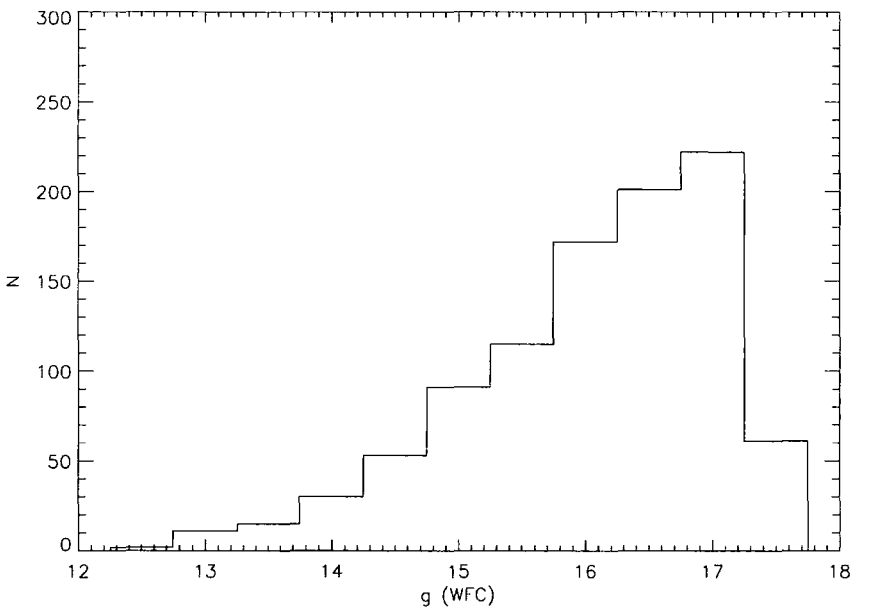

Figure 3.8: The distribution of the galaxy apparent magnitudes for 974 galaxies in the WFC sample whose recovered B/T ratios have $\chi^2_\nu < 2.0$. The histogram plot suggests that the sample is complete down to $g = 17.0$ magnitude.

Before we proceed to investigate the properties of the nearby cluster galaxies in more detail we need to ensure that the various measurements obtained are internally consistent (using the overlaps in the central region) and that they are also consistent with other published work.

Galaxy Magnitudes and B/T Ratios : Internal Consistency

The 10′ overlap area in the centre of our observations allows for an internal check of the WFC galaxy photometry and the recovered B/T ratios. The correlation plot shown in Figure 3.9 demonstrates excellent internal photometry. The B/T correlation plot is shown in Figure 3.10 and demonstrates a good internal recovery of the B/T ratios by Gim2D.

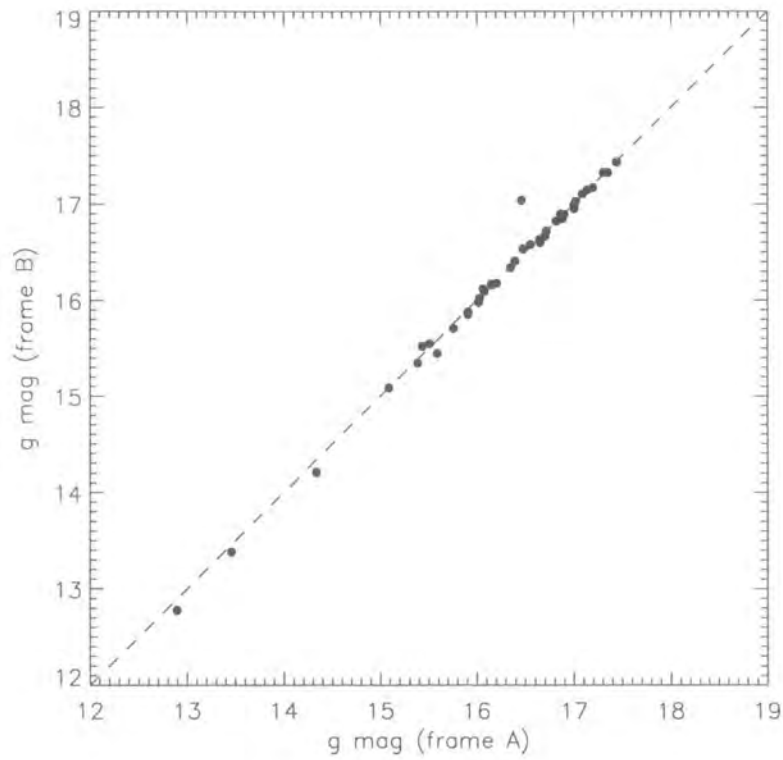

Figure 3.9: The 4-pointing dither pattern with a 10′ overlap area provides observations of the same objects taken with different CCDs and at slightly different times. The correlation between the apparent magnitudes of galaxies found in the region of overlap is plotted and shows an excellent internal photometric consistency. The dashed line corresponds to a one-to-one correlation. Frame A and Frame B refer to the independent images and can correspond to any one of the WFC CCDs (c.f. Figure 3.1).

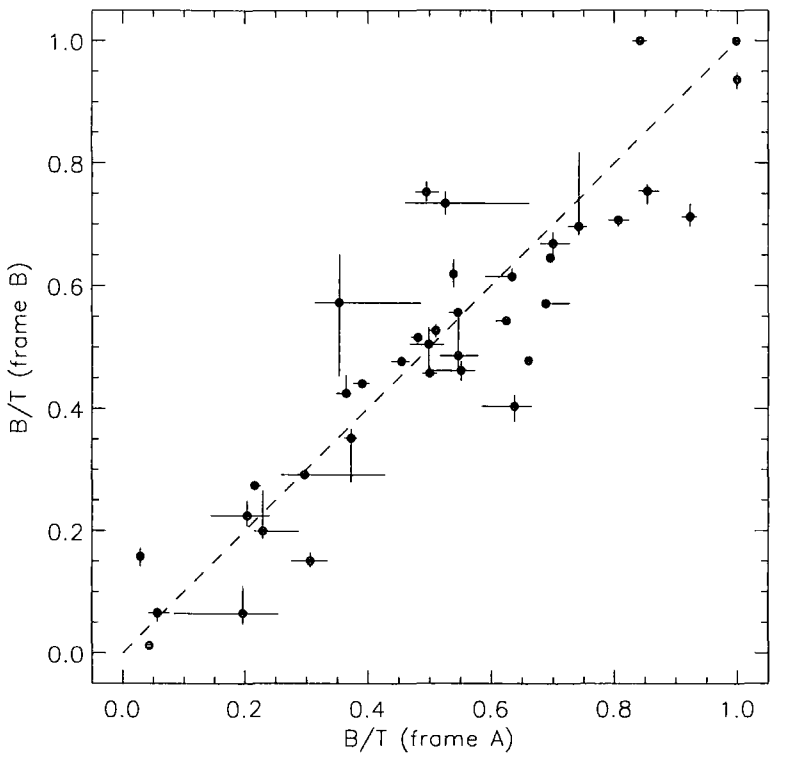

Figure 3.10: The 4-pointing dither pattern with a 10′ overlap area in the centre leads to observations of the same objects with different CCDs and taken at slightly different times. The figure demonstrates a good internal correlation between the recovered B/T ratios for galaxies found in the overlapping regions. Since the observations were conducted at slightly different times and the galaxies observed with different CCDs the scatter is mainly due to the change in the PSF. Frame A and Frame B refer to the independent images and can correspond to any one of the WFC CCDs (c.f. Figure 3.1).

Galaxy Magnitudes : External Consistency

The first independent photometric check was done using the A0168 cluster with the external photometry taken from the Sloan Digital Sky Survey (c.f. Chapter 5). A correlation plot of the WFC g-band 20″ aperture and total magnitudes with that of the SDSS g-band Petrosian magnitude (Petrosian 1976) is shown in Figure 3.11. Figure 3.11 (a) shows the aperture effects to be responsible for the underestimate of the total galaxy light at bright magnitudes. Figure 3.11 (b) demonstrates that the photometric measurements are in a good agreement when total magnitudes are used to obtain WFC galaxy magnitudes. No correction for galactic reddening is applied to the galaxy magnitudes.

Another independent check was done using the A2634 cluster galaxies whose accurate CCD photometry was published by Lucey et al. (1997). Again no galactic reddening correction was applied in the case of the WFC data but has been done in the case of the data taken from Lucey et al. (1997). The average B-band galactic extinction for Lucey et al. (1997) data is $A_B = 0.15$ and is mainly responsible for the systematic 0.09 magnitude offset seen in Figure 3.12.

3.3 Results and Discussion

3.3.1 Local Projected Galaxy Density, Morphology Density Relation and Field Correction

To overcome the uncertainty in the cluster relaxation state and the uncertainty in the exact position of the cluster centre Dressler (1980b) studied the population mix of nearby cluster galaxies as a function of the local projected galaxy density. Dressler (1980b) defined local projected galaxy density to be the surface density out to the 10^{th} nearest projected neighbour in galaxies per Mpc^2 as given in Equation 3.7. The significance of the local projected galaxy density lies in the fact that it has revealed the presence of the morphology-density relation (Dressler 1980b) i.e. a steep increase of the fraction of elliptical and S0 galaxies with local density followed by a corresponding decrease of the fraction of spiral galaxies.

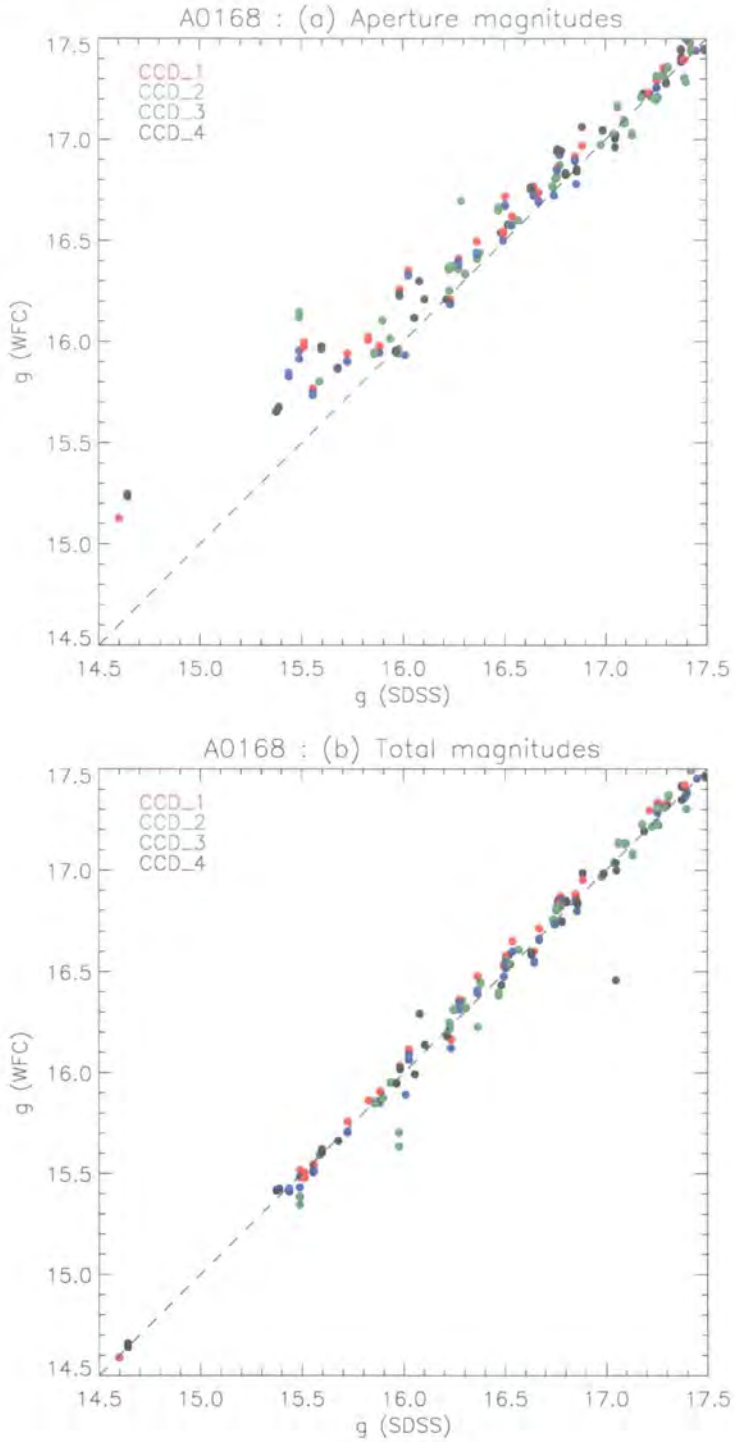

Figure 3.11: The cluster A0168 lies in the region imaged by the Sloan Digital Sky Survey (Chapter 5). The SDSS g-band (reddening uncorrected) galaxy Petrosian magnitudes are correlated with the WFC (a) : aperture magnitudes and (b) : total magnitudes. (a) shows the aperture effects to be responsible for the underestimate of the total galaxy light at bright magnitudes. (b) demonstrates that there is a good agreement between the SDSS and the total WFC magnitudes. NB the plots contain multiple detections.

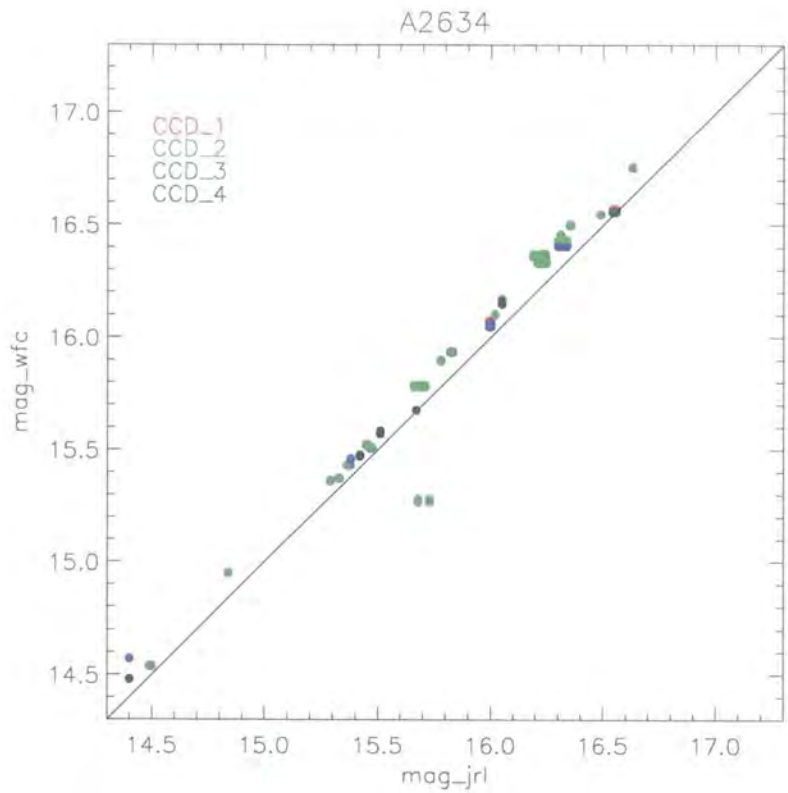

Figure 3.12: The check of the photometric measurements of galaxies in A2634 cluster using the data published by Lucey et al. (1997) translated into the g-band using Fukugita et al. (1995). The WFC g-band magnitudes are also measured using the 20″ diameter apertures as used by Lucey et al. (1997). The WFC data is not corrected for the galactic reddening. The average B-band galactic extinction for Lucey et al. (1997) data is $A_B = 0.15$ and is mainly responsible for the systematic 0.09 magnitude offset seen in this figure.

$$\rho_{proj} = 10/(\pi D_{10}^2) \tag{3.7}$$

Since the WFC data is a subsample of the Dressler (1980a) catalogue it is important to verify that the (field-corrected) morphology-density relation holds for our sample too before any further analysis is commenced. But since redshifts are unavailable for all galaxies in our cluster sample the correction for the field contamination to the 10^{th} nearest neighbour is performed statistically. Dressler (1980a) estimated the field galaxy correction down to the apparent magnitude limit of the sample to be 8 ± 5 galaxies per degree square. To verify the D80 estimates for the average field contamination the data from the Sloan Digital Sky Survey (SDSS) was used[§]. There are $\sim$ 16000 galaxies in the SDSS EDR survey area of 1360 degree square down to the apparent magnitude limit adopted in this study ($g = 17.0$). This gives a typical field value of 12 galaxies per degree square which is within the error of the value quoted by Dressler (1980a) and in good agreement with the number counts published by Yasuda et al. (2001).

To overcome the uncertainty that arises from the incompleteness Dressler (1980b) adopted $M_V = -20.4$, or $M_g = -20.07$ using Fukugita et al. (1995), as the absolute magnitude limit to which the density is computed and this value is retained for the purpose of this study. The D80 field correction is translated into the number of galaxies per Mpc^2 since the exact area imaged depends on the cluster redshift [¶]. To ensure that the number densities for clusters at different redshifts refer to the same limiting absolute magnitude ($M_g = -20.07$) the number densities are multiplied by the factor obtained from Equation 3.8.

$$R = \int_{-\infty}^{-20.07} \phi(M)dM / \int_{-\infty}^{M_{g_{lim}}} \phi(M)dM \tag{3.8}$$

$M_{g_{lim}}$ is the absolute magnitude limit at a cluster redshift that corresponds to the adopted apparent magnitude limit and $\phi(M)$ is the luminosity function assumed to have the Schechter form (Schechter 1976) with $M_g^* = -21.41$ and $\alpha = 1.21$, i.e.

[§]Please refer to Chapter 5 for detailed discussion of the SDSS.

[¶]The value of $H_0 = 50$ kms^{-1} Mpc^{-1} used by Dressler (1980b) is adopted.

the luminosity function parameters of Norberg et al. (2002) with the b_j absolute magnitude translated to the g-band using Fukugita et al. (1995).

The field-corrected morphology-density relation is presented in Figure 3.13. The left-hand side of Figure 3.13 shows the morphology-density relation of Dressler (1980b) and for comparison the right-hand side of Figure 3.13 shows the morphology-density relation for the WFC subsample and demonstrates that the WFC subsample is a good representation of the total sample of Dressler (1980a).

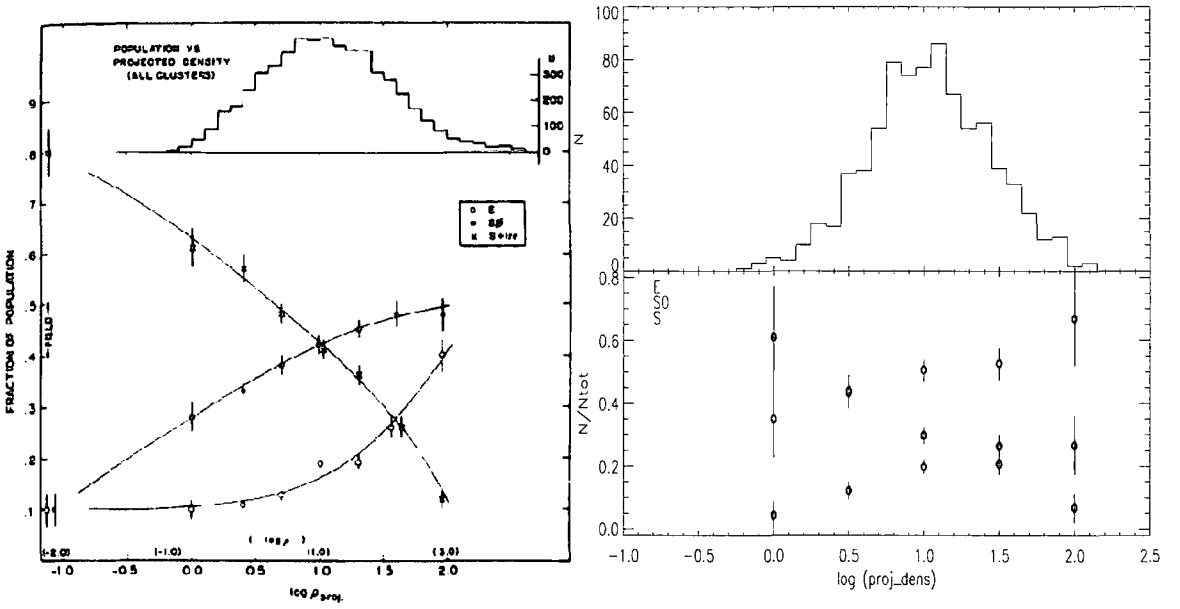

Figure 3.13: Left-hand side shows the morphology-density relation of Dressler (1980b). The right-hand side of the figure shows the morphology-density relation for the WFC subsample demonstrating that the WFC subsample is a good representation of the total sample of Dressler (1980a).

3.3.2 D80 : B/T Distributions

In this section we present the results from the bulge-to-disk decompositions of morphologically classified galaxies from the Dressler (1980a) study. Figure 3.14 shows the distribution of the B/T ratios as a function of morphology visually determined

by Dressler (1980a). The recovered B/T ratio (and therefore the overall bulge luminosity) becomes progressively larger as one moves from spiral to S0 to elliptical galaxies. This is consistent with the study of Dressler (1980a) who found that the visually determined bulge magnitude distribution follows a similar trend.

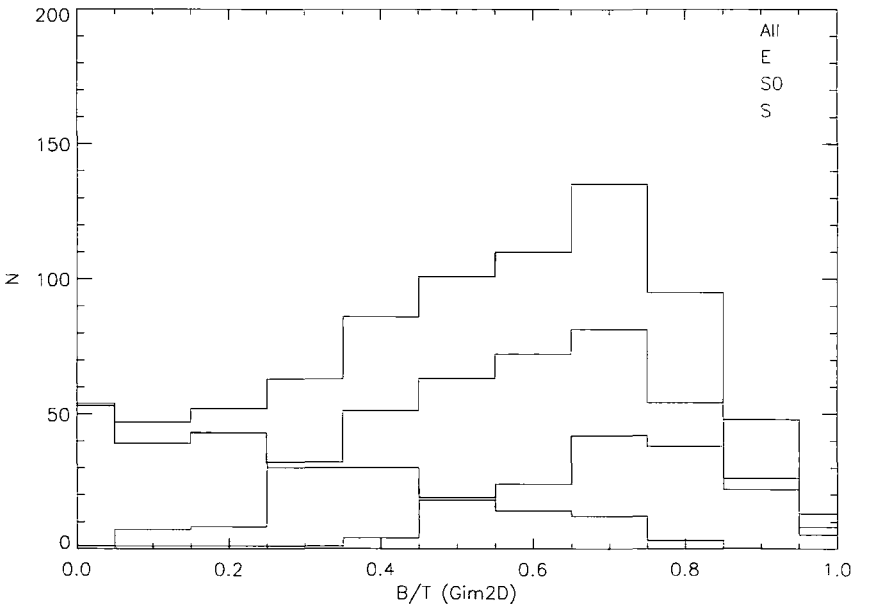

Figure 3.14: The distribution of the B/T ratios for all the WFC galaxies (black histogram). Also plotted is the distribution of the B/T ratios as a function of the morphological type visually determined by Dressler (1980a). Morphologically classified spiral galaxies (S) have predominately low B/T ratios whilst ellipticals (E) have predominately high B/T ratios. The S0 distribution spans a range of B/T ratios but is skewed towards the higher B/T values.

3.3.3 Morphological Field Correction and Luminosity Functions

Before further commencing this study it is important to calculate (and if necessary correct for) the contamination from the underlying field population. The statistical correction is performed using the g-band number counts of Yasuda et al. (2001) to obtain the number of field galaxies detected in the cluster imaging area for a given

apparent magnitude bin. For every cluster the cluster redshift is used to convert the apparent magnitudes into the corresponding absolute magnitudes. The field correction for different morphological types is obtained by using the proportions determined by Dressler (1980a), namely 50/35/15% for S+I/S0/E morphological types. The absolute magnitudes of cluster galaxies are obtained assuming that all galaxies are at the given cluster redshift and their distribution is shown in Figures 3.15 and 3.16 with the apparent magnitude cut of $g = 17.0$ imposed (c.f. Figure 3.8). For the purpose of comparison the contribution of the field is also plotted - the field correction is typically of the order of $\sim 10\%$ and can therefore be neglected in what follows.

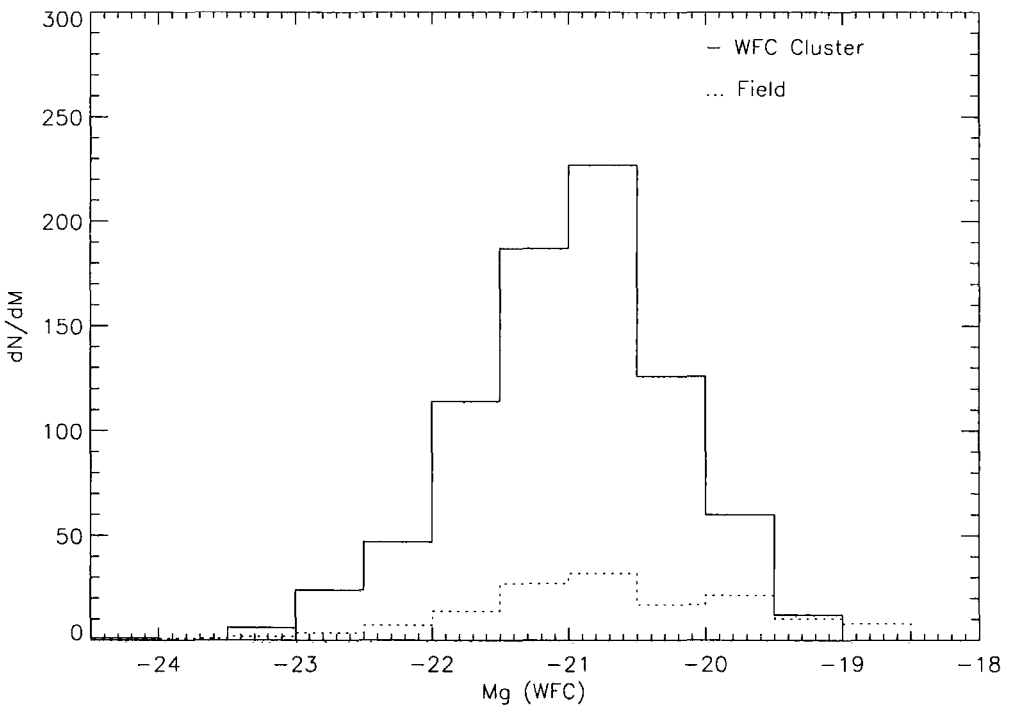

Figure 3.15: The luminosity function of the WFC cluster sample. The solid line shows the distribution of the absolute magnitudes for the WFC galaxies brighter than $g = 17.0$. To obtain the absolute magnitudes galaxies are assumed to be at the given cluster redshift. The dashed line shows the field contamination calculated using the number counts of Yasuda et al. (2001). The field correction is typically of the order of $\sim 10\%$.

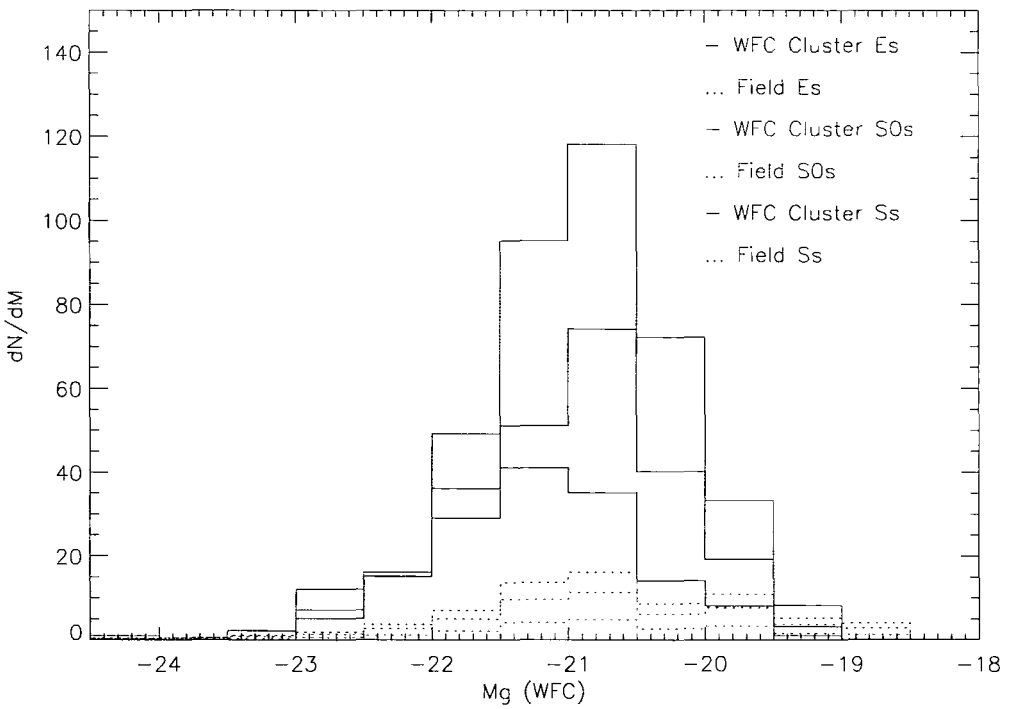

Figure 3.16: The luminosity function of the WFC cluster sample uncorrected for the field contamination and colour coded for different morphological types. The solid lines show the distribution of absolute magnitudes for the WFC galaxies brighter than $g = 17.0$. To obtain the absolute magnitudes all galaxies are assumed to be at the cluster redshift. The dotted lines show the expected field contamination with the morphological mix taken from Dressler (1980b).

3.3.4 Bulge Magnitudes and Local Environment

Dressler (1980b) studied the distribution of bulge magnitudes as a function of the local density for different morphological types and concluded that cluster S0s have bulges that are brighter than those of the corresponding cluster spirals. Dressler (1980b) used this as an argument against ram pressure stripping being the dominant mechanism responsible for the production of S0 galaxies in cluster environments since if S0s are simply swept spirals then their bulge magnitudes should be similar. However, if the disks of spiral galaxies are allowed to fade by some arbitrary amount in a magnitude limited sample, most of the highly disk-dominated galaxies would drop out leaving the more bulge dominated ones behind. Dressler (1980b) found that a 2 magnitude disk fade would be sufficient to bring the two distributions into agreement but this was ruled out because the total luminosity functions of S0s and spirals were almost identical. However, the Dressler (1980b) study relied upon visually estimated bulge magnitudes and we will repeat this analysis using quantitative estimates of bulge luminosities.

The obtained B/T ratios are used to infer the WFC g-band bulge magnitudes for all the galaxies brighter than $g = 17.0$. The bulge magnitude distributions of the present-day cluster spiral and S0s are shown in Figure 3.17 (a) and appear to be very different. Figure 3.17 also shows the effect of disk fading by 1 and 2 magnitudes. The figure implies that a one magnitude disk fade is sufficient to bring the distributions of the bulge magnitudes of cluster spirals and S0s into agreement as more disk dominated galaxies are lost due to the apparent magnitude limit imposed on the sample. The figure also suggests that the fading of the disks of spiral galaxies acts to remove all the faint bulge spirals/S0s from the sample - an effect that should manifest itself in the luminosity functions of spiral and S0s being different. However, as shown in Figure 3.18, the luminosity functions of cluster spirals and S0s appear to be very similar implying that the difference observed between the bulge magnitudes of spirals and S0s cannot be due to the simple apparent magnitude selection effect. The incompleteness at the faint-end of the luminosity function on the other hand prevents this from being conclusive.

We next investigate any trends observed in distributions of the bulge magnitudes with the local galaxy density to try to gain more insight into the process(es) that may be responsible for the observed dissimilarity between the bulge magnitudes of spiral and S0 galaxies. The distributions shown in Figure 3.19 confirm the result of Dressler (1980b) that S0s have systematically brighter bulges than the spiral galaxies. However, the bulge magnitudes for both spiral and S0 morphological type are only a potentially rising function of the local density. The points represent the median values and the error bars are inferred from the corresponding quartile points. The figure also demonstrates that S0s are sometimes found in the regions of low galaxy (and therefore presumably low gas) density where ram pressure stripping should be much less effective (Dressler 1980b). Dressler (1980a) used this as one of the arguments against ram pressure stripping being the dominant environmental process that transforms cluster spirals into S0s.

The effect of disk-fading is further investigated in terms of the derived bulge-to-disk ratios and their relation to the galaxy environment. Figure 3.20 (a) shows the difference between the bulge and total magnitudes for spiral and S0 galaxies with the median values being equal to 1.6 and 0.6 respectively. Shown in Figure 3.20 (b) is the difference between the bulge and total magnitudes for spiral galaxies only, after the galaxy disks were faded by 1 and 2 magnitudes. The median values are equal to 0.7 and 0.2 respectively again suggesting that the one magnitude disk fade could be sufficient to bring the distributions into agreement. The figures also demonstrate that the difference in the B/T ratios is roughly a constant function of local density. In addition Figure 3.21 demonstrates that in the disk fading scenario the overall distribution of the B/T ratio does shift towards larger values.

One problem with the results presented so far is that after the disk-fading is applied the number of spiral galaxies retained in the sample is small and the incompleteness at the faint-end of the luminosity function prevents any conclusive results to be drawn. This problem is tackled next by means of a study of a faded mock spiral galaxy distribution to see if the total number of modelled galaxies are

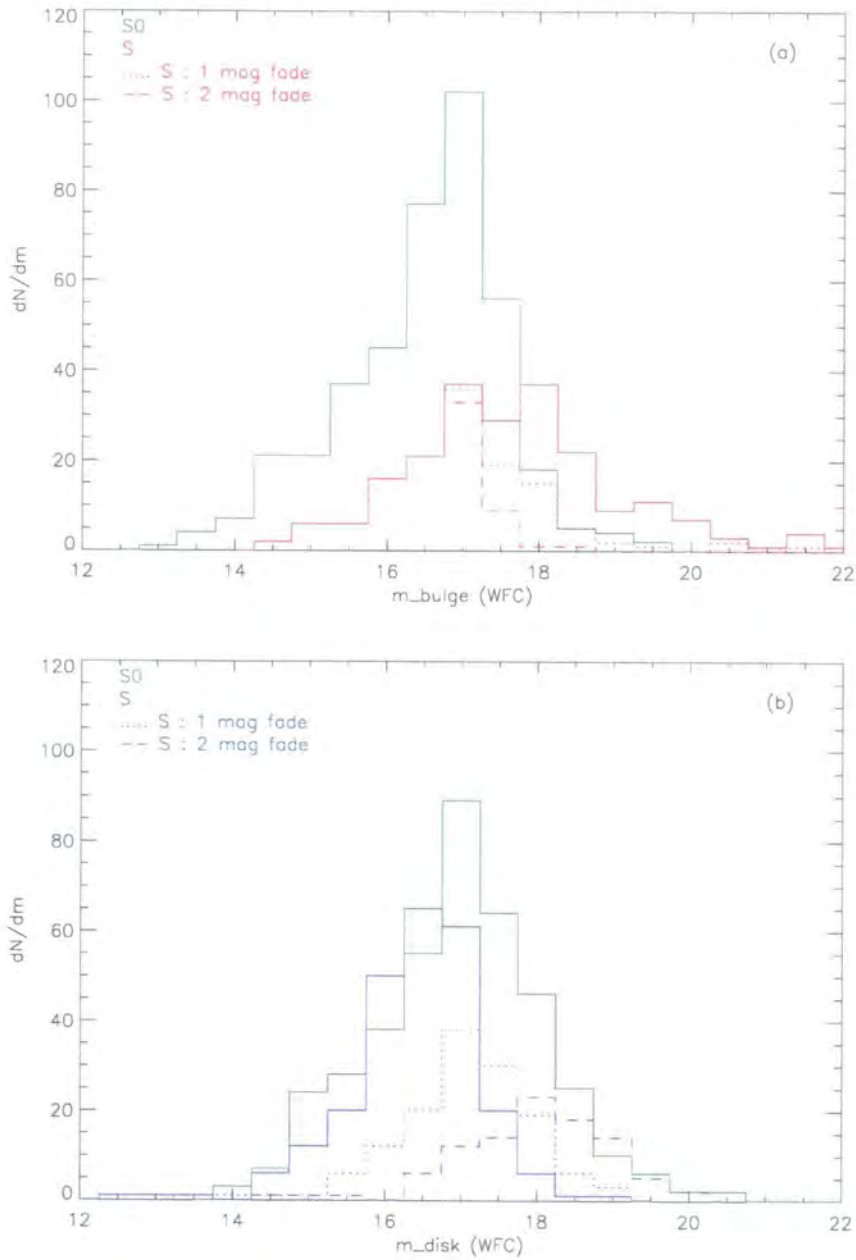

Figure 3.17: Effects of disk fading on the quantitative bulge and disk magnitudes. Figures (a) and (b) demonstrate that a one magnitude disk fade is required to bring the distributions of the present-day spirals into agreement with the distribution of the present-day S0s in clusters.

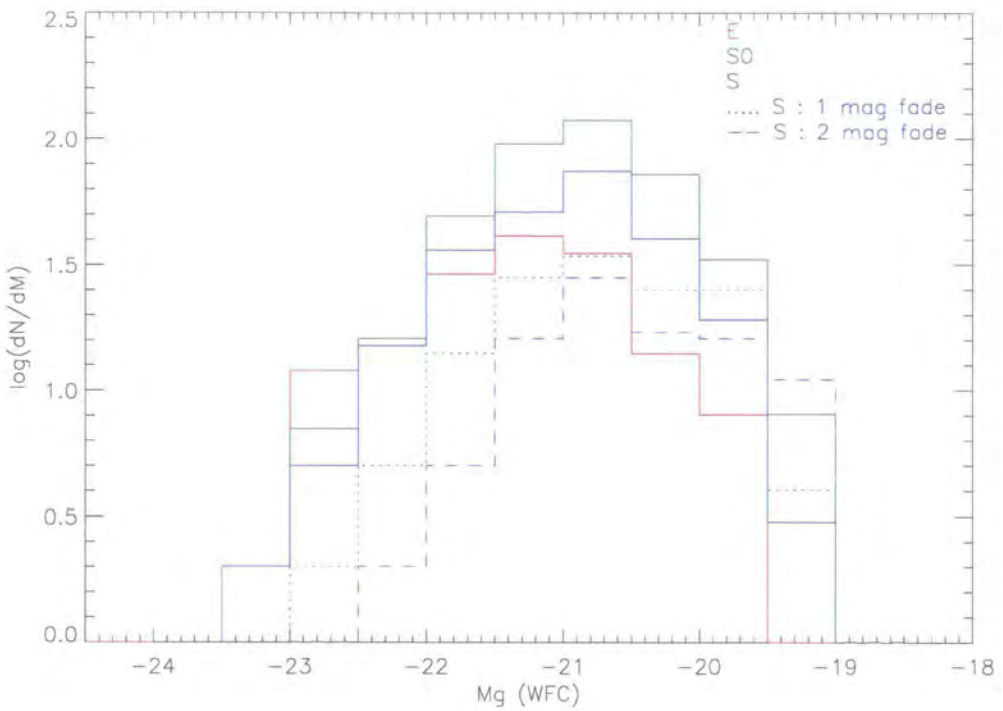

Figure 3.18: The observed luminosity functions of different morphological types in nearby clusters. The luminosity function for S0 and spiral galaxies are in good agreement. The disk fading scenario shows that the LF of spiral galaxies with faded disks is not consistent with the LF of S0s.

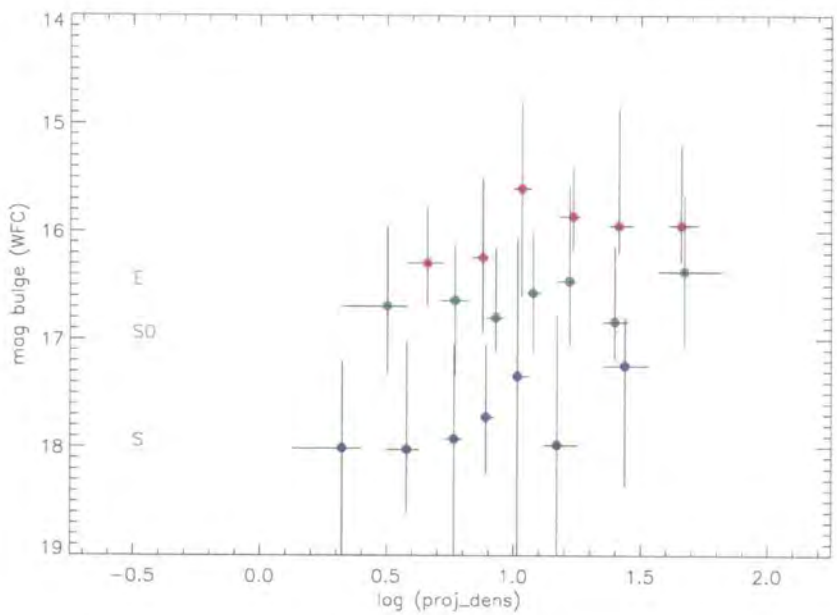

Figure 3.19: The bulge magnitudes as a function of the local projected galaxy density. Displayed are the medians (symbols) and quartile points (error bars). The figure demonstrates that cluster S0s have consistently brighter bulges than the corresponding spiral galaxies.

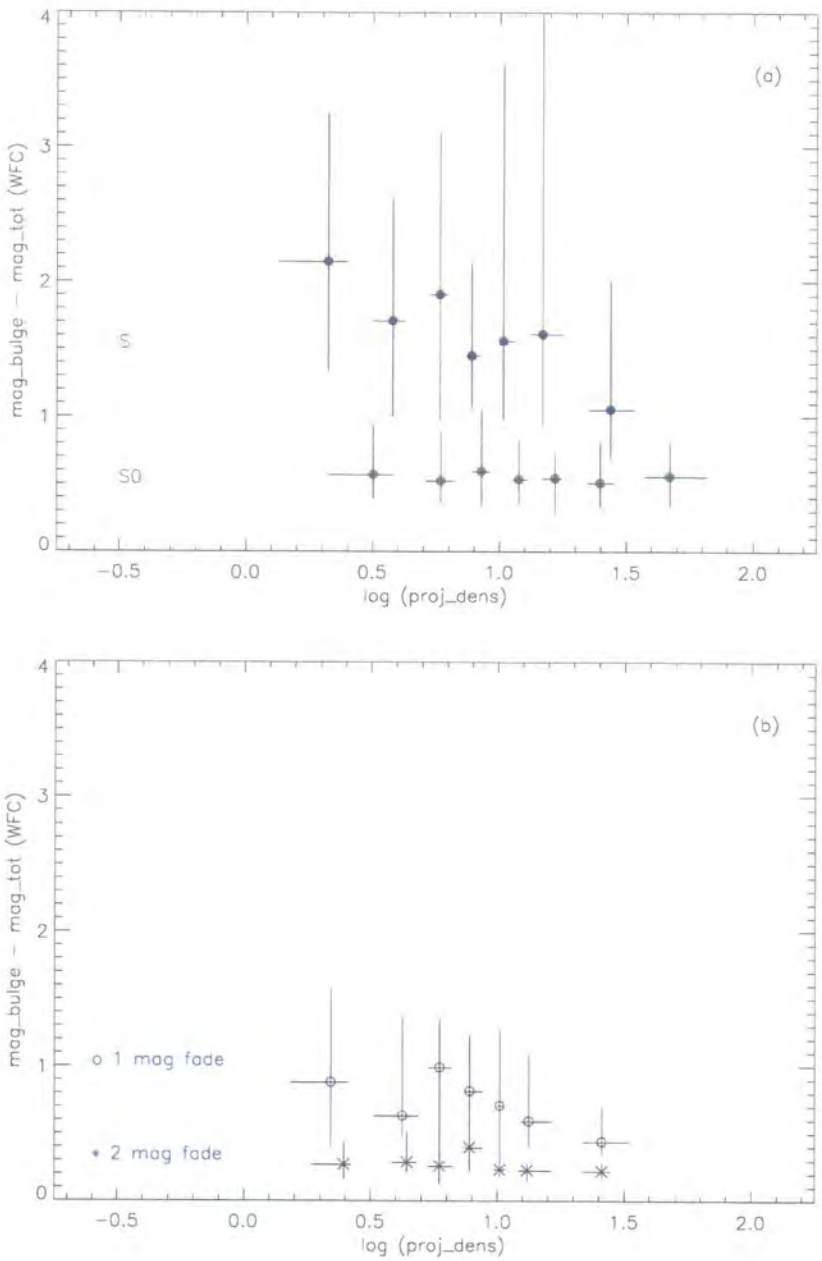

Figure 3.20: The difference between the bulge and total magnitudes as a function of the local projected galaxy density. Displayed are the medians (symbols) and quartile points (error bars). The figure (a) demonstrates the difference in the B/T ratio as a function of local density. The figure (b) shows that a one magnitude disk fade is required to bring the two distributions in agreement.

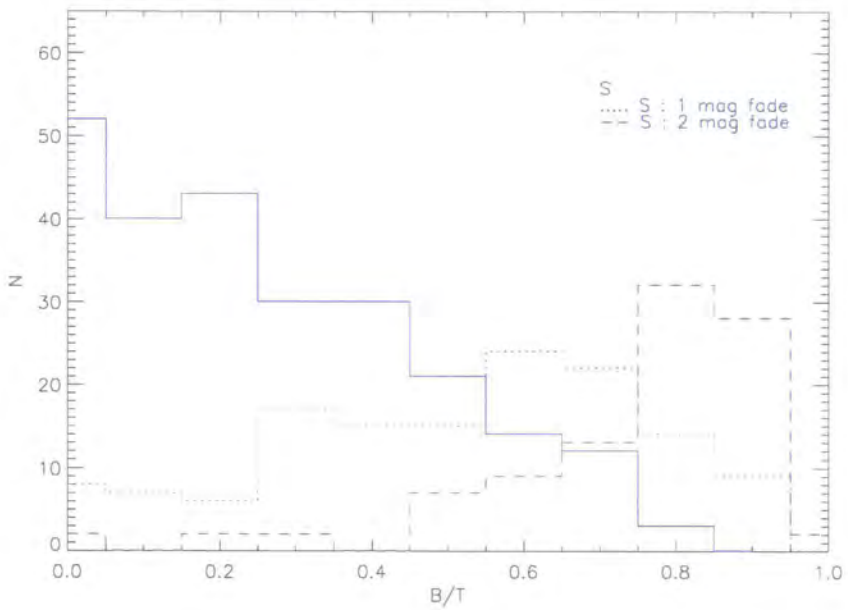

Figure 3.21: Effects of disk fading on B/T. The figure shows the distribution of B/T ratios before and after the disk fading. The B/T ratio does appear to shift to larger values by simply fading the disks and even more so due to the apparent magnitude limit imposed on the sample.

consistent with observations.

3.3.5 Mock Luminosity Function of Spiral Galaxies

In Section 3.3.4 the incompleteness at the faint-end of the luminosity function prevented the argument of disk-fading from being conclusive. To try to quantify the effect the derived distribution of the present-day cluster spirals can be used to create a mock present-day spiral distribution. If the disks of mock spirals are allowed to fade by one magnitude one can test whether the 'faded' spiral distribution is consistent with the present-day S0 distribution, assuming that the present-day population of cluster spirals is representative of the overall cluster spiral galaxy population and that it matches the spiral population that was responsible for creating the present-day cluster S0s. This allows a crude estimate of the luminosity function parameters for spiral galaxies that may be responsible for producing the present-day cluster S0s.

The WFC sample contains a total of 243 galaxies brighter than $g = 17.0$ and morphologically classified as spirals. Assuming that the present-day distribution of spiral galaxies can be described by a Schechter luminosity function (Schechter 1976) the mock spiral distribution can be created by randomly sampling the Schechter luminosity function for a range of $M^* = [-22.0, -21.5, -21.0, -20.5, -20.0]$ and $\alpha = [-1.0, -1.2]$. The Schechter function is random-sampled N times for each cluster down to a given M_{lim} set by the apparent magnitude limit at the cluster redshift where N is the number of spiral galaxies in a given cluster. A B/T ratio is assigned to every galaxy in this mock distribution such that the mock B/T distribution matches the distribution of the observed B/T ratios Figure 3.22 (a). Minimizing the error weighted difference between the observed absolute magnitude distribution and that of the corresponding mock distributions (different M^* and α) gives a crude (1/2 magnitude) estimate of M^* and the corresponding α for the LF of the present-day cluster spirals. The best-fit values are $M^* = -21.5$ and $\alpha = -1.2$ with $\chi^2_\nu = 1.02$ and are in good agreement with the known studies (Norberg et al. 2002). The disks of the mock galaxies are then faded by 1 magnitude and only galaxies

whose 'faded' apparent magnitudes have met the imposed apparent magnitude cut are retained. The absolute magnitude distribution for the best-fit mock luminosity function with faded disks is compared to that of the corresponding absolute magnitude distribution for present-day cluster S0s (normalised such that the distributions agree at the bright end) as shown in Figure 3.22 (b). Figure 3.22 (b) shows the real and mock spiral distributions as well as the real distribution of S0s normalised such that the bright end matches the 'faded' S distribution at the bright end. Even though the real and mock distributions for spirals agree very well the distribution of 'faded' mock spirals does not agree particularly well (especially at the faint-end) with the observed (normalised) distribution of S0s with $\chi^2_\nu = 1.91$. The number of faded mock spirals fainter than $M_g = -20.5$ is $N_S = 68.0 \pm 8.0$ almost 4σ away from the observed present-day distribution of cluster S0s $N_{S0} = 38.0 \pm 6.0$ unlikely to be completely due to the incompleteness of S0s seen at the faint-end.

There remain two possible explanations for the discrepancy between the luminosity functions of present-day cluster spirals and S0s. This difference can be due to either (or both) : (1) the present-day cluster spiral population is not a good representation of the spiral galaxy populations that produced present-day cluster S0s or (2) the simple disk fading mechanism cannot uniquely account for the difference observed between the distributions.

3.3.6 D80 : B/T Distributions and Cluster X-ray Luminosity

The effect of the global cluster environment on the galaxy B/T ratios can be investigated based on the cluster X-ray luminosity. The X-ray luminosity information is used to divide the cluster sample into low $L_x < 1.0 \times 10^{43}$ ergs s^{-1} (A0168, A0978, A1185 and A1631) and high $L_x > 4.0 \times 10^{43}$ ergs s^{-1} (A0496, A0754, A1644 and A1656) luminosity clusters (c.f. Table 3.1). The distribution of B/T ratios for the two samples is shown in Figure 3.23. The figure demonstrates that the X-ray luminous clusters are preferentially populated with galaxies with larger B/T ratios.

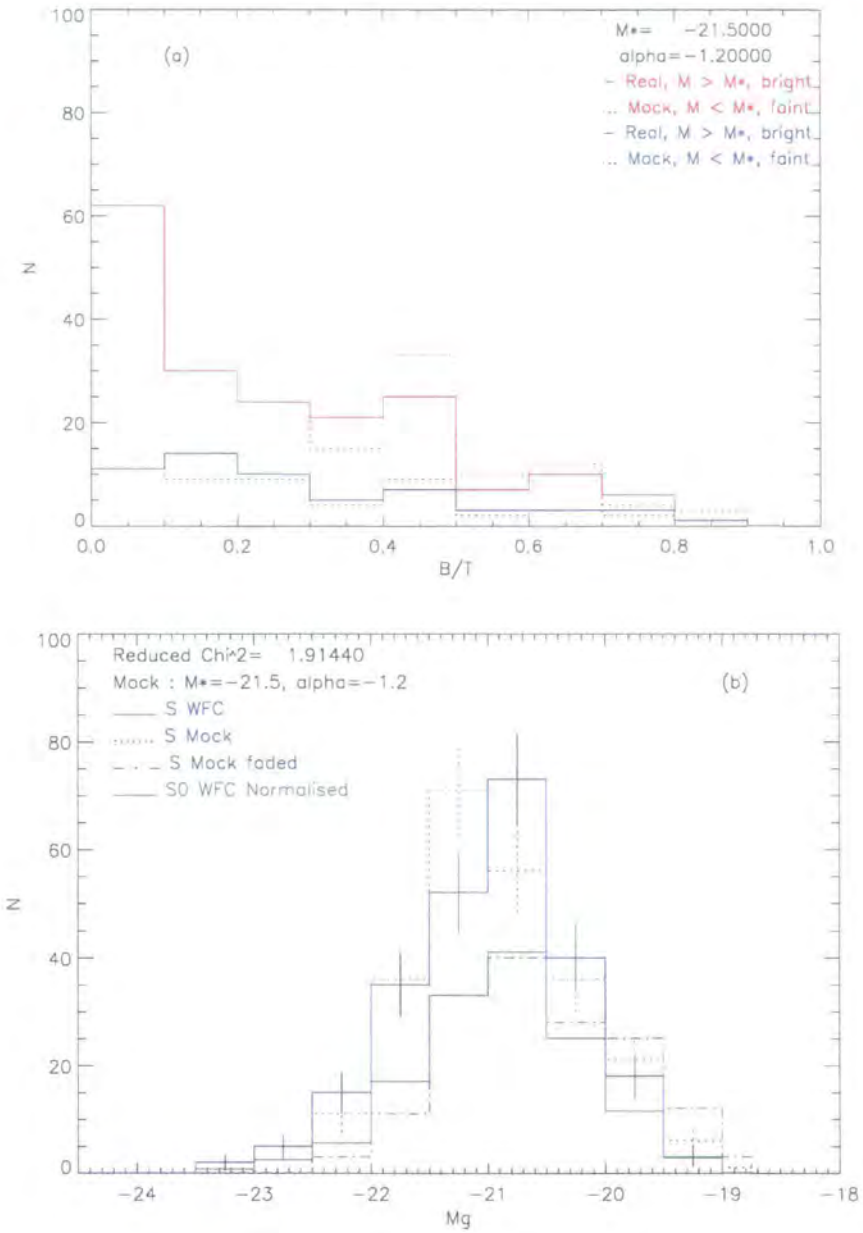

Figure 3.22: Mock galaxy sample and disk fading. (a) The distribution of B/T ratios for real (solid line) and mock (dotted line) galaxies split by their absolute magnitude which shows that the distribution of B/T ratios of mock galaxies closely matches the one of the real galaxies. (b) The luminosity functions of the present-day cluster real and mock spirals (blue solid and dotted lines). Overplot are the Poisson error bars. Also shown is the normalised distribution of present-day cluster S0s (green solid line). The disks of mock galaxies are faded by 1 magnitude and only galaxies which made the apparent magnitude limit are retained in the sample (blue dotted-dashed line). The agreement between the present-day S0 and 'faded' spiral distribution is not particularly good ($\chi^2_\nu = 1.91$, prob= 0.0024) especially at the faint-end.

Dressler (1980b) also found the morphology-density relation of the X-ray luminous clusters ($L_x \geq 10^{44}$ ergs s^{-1}) to show an excess in the fraction of S0 galaxies over the full density range with a corresponding deficiency of spirals in comparison to the average relationship and is suggestive of a global cluster-related mechanism at work.

3.4 Summary and Conclusions

In this Chapter we have presented a wide-field survey of a homogeneous sample of 13 nearby rich clusters undertaken in the SDSS g-band. All galaxies in the sample have visually assigned morphological types and bulge magnitudes taken from Dressler (1980a). The Gim2D code of Simard et al. (2002) was used to obtain quantitative measures of galaxy B/T ratios and the corresponding bulge magnitudes. The comparison was made between visual and quantitative studies to test the whether the present day cluster S0s can be accounted for by a simple disk fading mechanism of the present day spiral galaxies (Dressler 1980b).

The results presented in this Chapter are broadly consistent with the Dressler (1980b) study. The cluster spirals are found to have quantitative B/T ratios on average smaller than the cluster S0s. The bulge magnitudes are also found to be fainter for the spiral types, consistent with S0 galaxies not simply being disk-faded spiral galaxies. However, if the disks of spiral galaxies are allowed to fade by 1 magnitude the spiral galaxies with small B/T ratios are found to predominately drop out of the sample due to the imposed apparent magnitude limit. The luminosity functions of spiral galaxies and S0s being very nearly equal argues against this selection effect being fully responsible for the observed difference between the bulge magnitudes of spirals and S0s. However, the faint-end of the luminosity function suffers for the incompleteness making this argument inconclusive.

Assuming that the present-day luminosity function of cluster spirals is a representative one for the spirals that are believed to have produced the present-day cluster S0s we create a mock spiral galaxy distribution to test for the production of

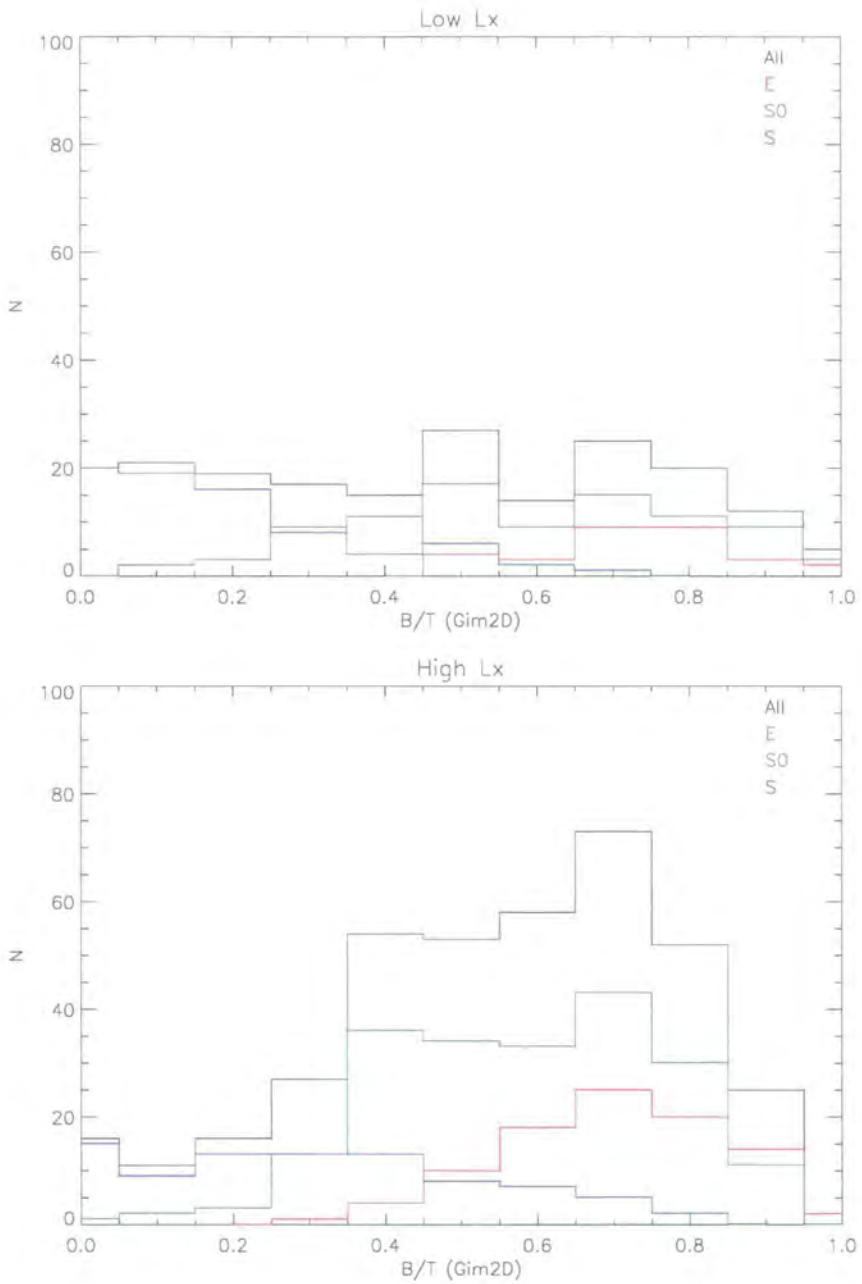

Figure 3.23: Using the X-ray luminosities of Ledlow et al. (2003) the WFC cluster sample is divided into X-ray faint ($L_x < 1.0 \times 10^{43}$ ergs s^{-1}) and X-ray bright ($L_x > 4.0 \times 10^{43}$ ergs s^{-1}) subsamples. The figure demonstrates that the fraction of bulge light are larger for the bright X-ray subsample where the gas density is presumably higher and thus stripping more effective.

cluster S0s by the disk fading mechanism. It is found that the 'faded' mock spiral distribution is not in a particularly good agreement with the normalised present-day S0 distribution since it predicts too many (4σ) faint S0 galaxies and is unlikely to be completely due to the incompleteness of S0s seen at the faint-end. This supports the argument of Dressler (1980b) that there appear to be other processes acting to transform cluster spirals into cluster S0s which are not just global in nature. However, the presence of the global cluster-related processes is supported by the correlation observed between the B/T distributions and the cluster X-ray luminosity.

The main conclusions of this study is that the disk fading mechanism cannot uniquely account for the production of the present-day cluster S0s by simply fading the disks of the present-day cluster spirals. There is some indication that a global process related to the cluster environment may be at work. However, it still remains puzzling that the bulges of cluster S0s are brighter than those of spirals indicating that some mechanism that does not just act to reduce the disk component but also acts to enhance the bulge may be responsible for the spiral to S0 transformation. It is also possible that the assumption that the present-day cluster spiral population is a good representation of the overall spiral galaxy populations that produced present-day cluster S0s is not valid.

Chapter 4

Morphological Properties of Cluster Galaxies at $z \sim 0.5$

In this Chapter the Gim2D code of Simard et al. (2002) is used to obtain quantitative measures of galaxy bulge-to-disk ratios for a sample of intermediate redshift ($z \sim 0.5$) cluster galaxies. The quantitative bulge and disk luminosities are used to test for the evolution of $z \sim 0.5$ spiral galaxies into the present-day S0s in galaxy clusters under assumption that the intermediate redshift distribution of spiral galaxies is a good representation of the spiral population believed to be responsible for producing the present-day cluster S0s (Chapter 3). Comments on the potential mechanisms driving the transformation are given at the end of the Chapter.

4.1 Introduction

The advent of the Hubble Space Telescope (HST) in the mid 1990's made it possible to study properties of cluster galaxies at much higher redshifts than had previously been possible. The first collaboration to conduct an HST survey of galaxy clusters at $z \sim 0.5$ became known as the MORPHS collaboration and has produced a baseline for the study of galaxy evolution between the redshifts of $z \sim 0.5$ and present (Smail et al. 1997, Dressler et al. 1997, Poggianti et al. 1999). The high-resolution HST imaging enabled a unique morphological study of a large number of cluster galaxies at these redshifts. A morphology-density relation for the intermediate redshift ($z \sim 0.5$) clusters was found to hold in regular, centrally concentrated clusters but, contrary to the present-day irregular clusters, morphology-density relation was found to be almost absent (Dressler et al. 1997) in the irregular clusters at inter-

mediate redshifts. Interestingly the overall fraction of S0s in $z \sim 0.5$ clusters was found to be much lower and the corresponding fraction of spirals much higher than in their present-day counterparts. One way of explaining the discrepancy between the galaxy populations in the nearby and intermediate redshift clusters is a possible transformation of the $z \sim 0.5$ spirals into present day S0s via some cluster related process(es). Most of the $z \sim 0.5$ spirals appear to exhibit disturbed disk-like morphologies (Smail et al. 1997) - all very suggestive of some environmental process(es) driving the morphological change of galaxies in clusters between $z \sim 0.5$ and present. In a spectroscopic follow-up of the MORPHS study Poggianti et al. (1999) showed that the intermediate redshift cluster spirals exhibit very little star formation compared to the corresponding field counterparts and that their spectra show that the star formation was abruptly halted in the recent past perhaps quenched by the interactions with the cluster potential.

To test whether the intermediate redshift spiral to present-day S0 transformation hypothesis is correct, a quantitative study of intermediate redshift cluster galaxies has been conducted and the derived B/T ratios used to predict the structural properties of the S0 distribution observed in the present-day clusters presented in Chapter 3.

4.2 MORPHS : Data and Observations

4.2.1 MORPHS : Imaging

The imaging of the MORPHS clusters was obtained using the Wide-Field and Planetary Camera 2 (WFPC2) on the 2.4m Hubble Space Telescope (HST). Each of the three WFPC2 CCDs is a 800 × 800 pixel array with the pixel scale of 0.1″/pixel giving a total camera field of view of approximately 5 square arcminutes. A summary of the 9 observed intermediate redshift clusters ($0.37 < z < 0.56$) is given in Table 4.1. The clusters were selected primarily on the basis that they appear like nearby massive systems (e.g. the Coma cluster) but at higher redshifts. The

clusters were observed through the HST R (F702W) and I (F814W) bands which roughly translate into the rest-frame V-band making this sample comparable to the nearby cluster sample of Dressler (1980b) studied in Chapter 3. The full summary of the HST data, the corresponding reduction and the analysis is presented in Smail et al. (1997).

Table 4.1: MORPHS Cluster Sample and Properties.

Cluster	RA	Dec	z	WFPC2	T_{exp} (ks)	$L_x \times 10^{44}$ ergs s^{-1}
A370	02 40 01	-01 36 45	0.37	F814W	12.6	2.73
CL0939+47	09 43 02	+46 58 57	0.41	F702W	21.0	1.05
CL0939+47 (2)	09 43 02	+46 56 07	0.41	F814W	6.3	1.05
CL0303+17	03 06 15	+17 19 17	0.42	F702W	12.6	1.05
3C 295	14 11 19	+52 12 21	0.46	F702W	12.6	3.20
CL0412-65	04 12 51	-65 50 17	0.51	F814W	14.7	0.08
CL1601+42	16 03 10	+42 45 35	0.54	F702W	16.8	0.35
CL0016+16	00 18 33	+16 25 46	0.55	F814W	16.8	5.88
CL0054-27	00 56 54	-27 40 31	0.56	F814W	16.8	0.25

4.2.2 MORPHS : Catalogues

The study of Smail et al. (1997) has produced catalogues of the intermediate redshift cluster galaxies with reliable morphological classifications (Hubble and T-type) down to $R_{F702W} = 23.5$ and $I_{F814W} = 23.0$, where reliable is defined to be when the difference in visual morphological classification between different classifiers is better than $\sim 20\%$ (Smail et al. 1997). The correction from R_{F702W} to I_{F814W} band was done using the morphological type dependent galaxy colours at $z \sim 0.5$ (Smail et al. 1997).

The visually obtained galaxy T-types of Smail et al. (1997) were used to separate the galaxies into three main morphological classes : (a) Ellipticals have T-type=

$-5, -4$; (b) S0s have T-type= $-3, -2, 0$; and (c) Spiral galaxies have T-type= $1, .., 7$. This broad classification is adopted in the study proposed here.

4.2.3 Object Detection and Identification

The object detection was performed using the SExtractor v.2.2.2 software (Bertin & Arnouts 1996). A low 1.5σ detection above the sky background was found necessary to ensure that all the flux that belongs to a galaxy is correctly identified (using the decompositions of model galaxies). The SExtractor deblending parameters as described in Chapter 3 were retained. The standard procedure described in Chapters 2 and 3 is followed for the postage stamp extraction for the real data and for the object masks produced by SExtractor. In this study, the catalogues of Smail et al. (1997) are used to identify the MORPHS galaxies with the objects detected by SExtractor, enabling the magnitudes and morphologies of Smail et al. (1997) to be retained for all the galaxies. An example of the imaging of the cluster CL0016 field and with morphologically classified galaxies (circled) is shown in Figure 4.1.

The aim of this study is to investigate the evolution of the morphological properties of galaxies with redshift. Gim2D is therefore purposely run on the morphologically classified galaxy sample to obtain a quantitative measure of the amount of light that resides in the bulge and disk components as a function of morphology. This enables a direct quantitative comparison between the intermediate and present day galaxy B/T distributions for different morphological types to investigate how the B/T and other properties change with redshift as galaxies evolve.

4.2.4 Tiny Tim PSF

The post-refurbishment HST imaging suffers from an undersampled PSF and Tiny Tim V6.1 software written by Krist (1995) is used to create an oversampled PSF to provide a better analytic match to the real PSF. A PSF of $FWHM = 0.07''$ and a full box size of $FWHM = 2.4''$ is created with an oversampling factor of 5, the value recommended to use for Gim2D decompositions by Simard et al. (2002).

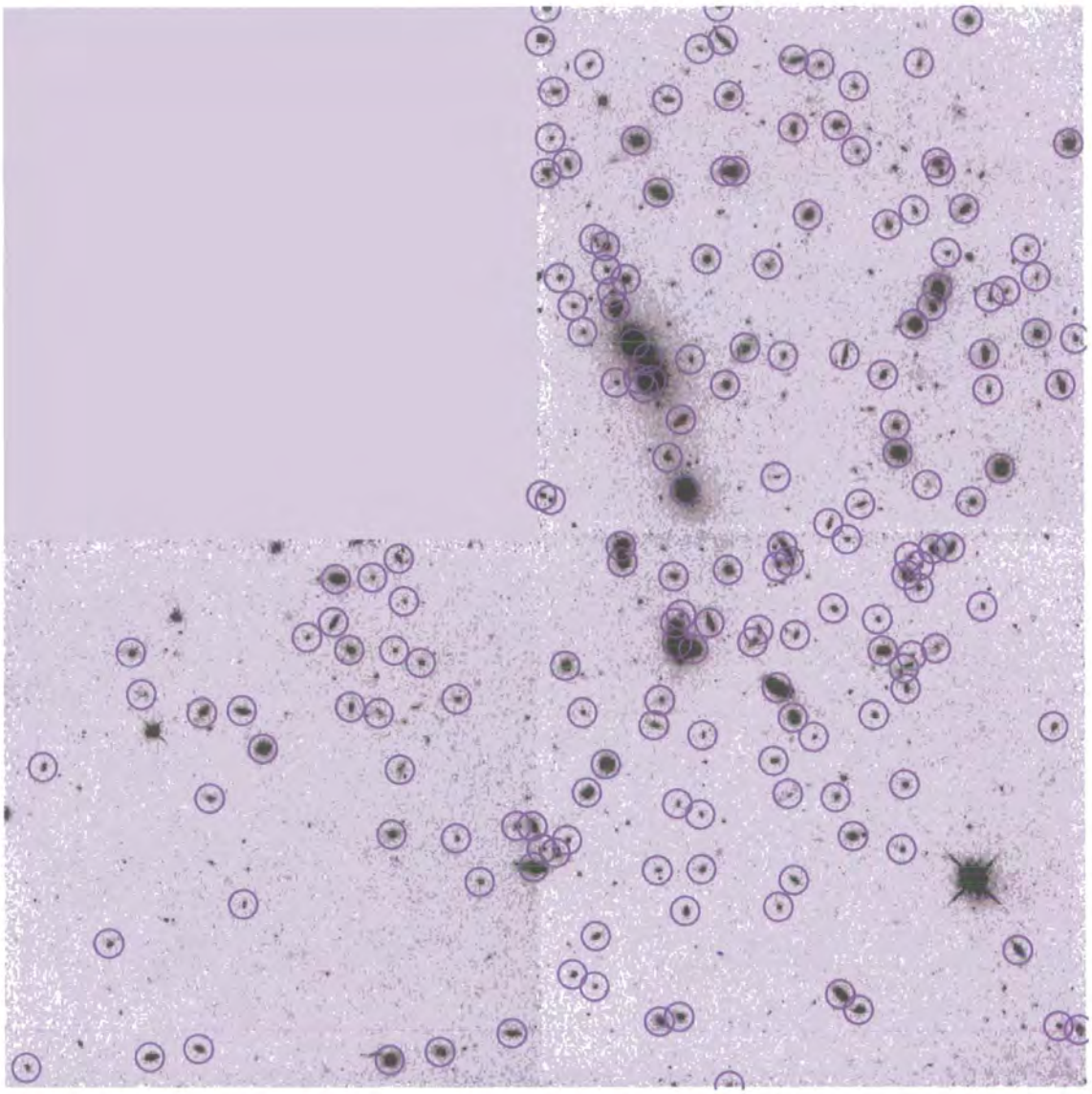

Figure 4.1: The WFPC2 image of the cluster CL0016. Circled are all the galaxies that have been morphologically classified by the MORPHS collaboration and are subsequently decomposed using Gim2D thus providing both visual morphological and quantitative information on the cluster members.

4.2.5 Gim2D Tests

Before running the decomposition software on the real data its performance for an appropriate data-set needs to be tested using a set of model galaxies (c.f. Chapters 2 and 3). The model galaxies were created in the same way as described in Chapter 2 : a MKOBJ model galaxy is placed onto a blank patch of sky in a given WFPC2 cluster frame and at the same time convolved with a Tiny Tim PSF. Since Gim2D was purposely written for the HST data and since it has already been demonstrated that Gim2D recovers the model parameters well (Chapters 2 and 3) the tests are done by modelling only 5 galaxies in each of the apparent magnitude bins. The results of the decompositions applied to a set of model galaxies with a range of B/T ratios are shown in Figure 4.2. The recovery of the input B/T ratio is ± 0.11 for the faintest bin and is consistent with the typical B/T error down to the given apparent magnitude limit (Chapter 2).

4.3 Results and Discussion

4.3.1 Decomposition Results

As in Chapters 2 and 3 the value of the reduced χ^2 was also used here to quantify the goodness-of-fit of the data. The examples of a good fit are shown in Figures 4.3 and 4.4 for which $\chi^2_\nu \sim 1.0$ and the residual image is noise dominated. It is estimated that $\sim 10\%$ of the data is lost due to either $\chi^2_\nu > 2.0$ or galaxies being too close to the edge of the frame for the decomposition to be performed. The final sample consists of 1057 morphologically classified galaxies brighter than $I = 23.0$ the adopted morphological completeness limit.

4.3.2 Absolute Magnitudes and K-correction

The MORPHS clusters span a relatively large redshift range and depending on their redshift are imaged in either R (F702W) or I (F814W) band. Since the observations

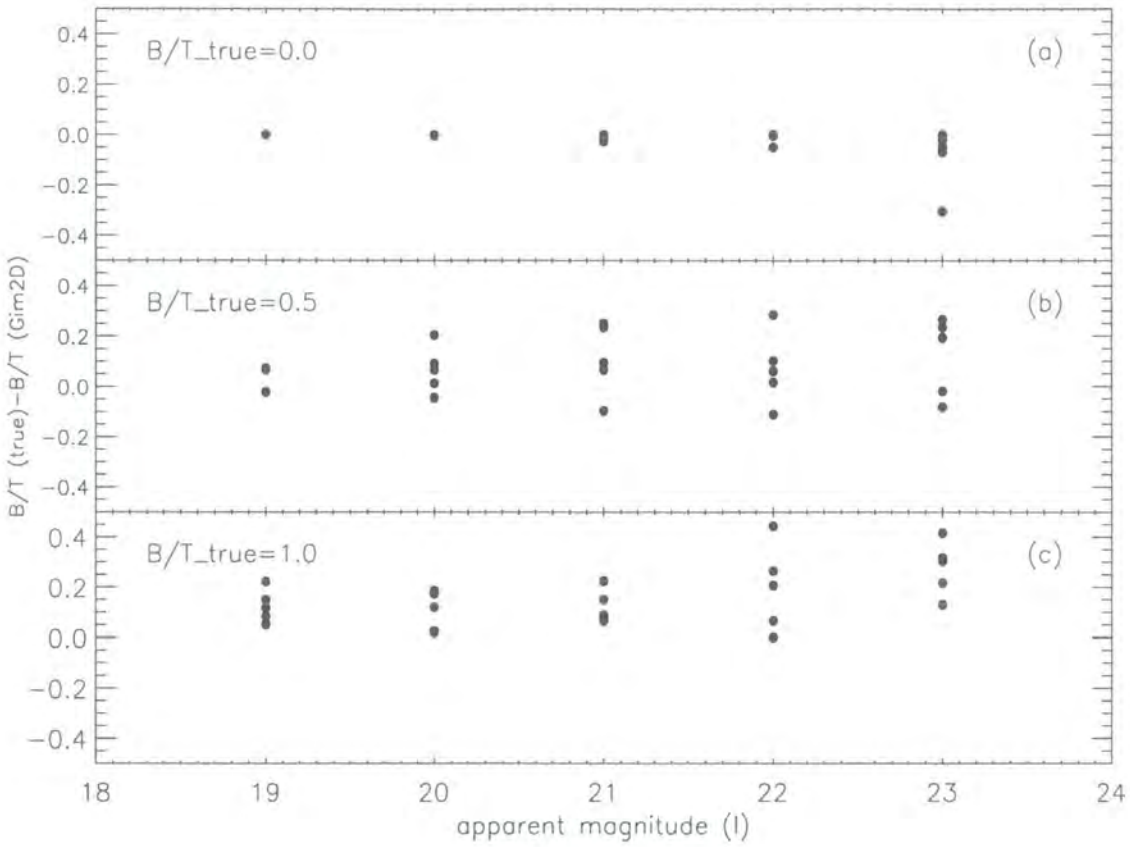

Figure 4.2: The recovery of the input B/T ratio for a set of model galaxies as a function of apparent magnitude. The model galaxies were created using the method described in Chapter 2. (a) $B/T_{true} = 0.0$, (b) $B/T_{true} = 0.5$ and (c) $B/T_{true} = 1.0$. The figures demonstrate that there is no systematic trend in the recovered B/T ratios with apparent magnitude. The offset in panel (c) is similar to that observed for bright galaxies modelled at low redshift and is a recognised feature of the Gim2D code (Chapters 2 and 3).

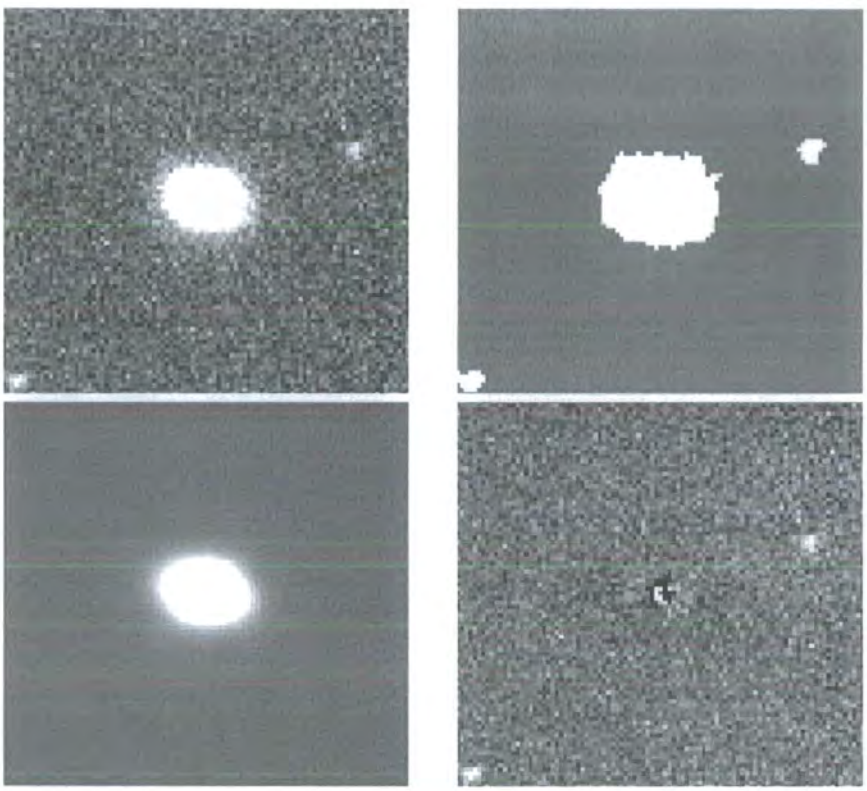

Figure 4.3: An example fit, this galaxy has B/T= 0.5. The shown are : (a) top left : the real galaxy postage stamp image, (b) top right : the segmentation mask, (c) bottom left : the model galaxy created using the best fit values and (d) bottom right : the residual postage stamp obtained by subtracting the model galaxy from the real galaxy image. The residual image is noise dominated and is indicative of a good fit.

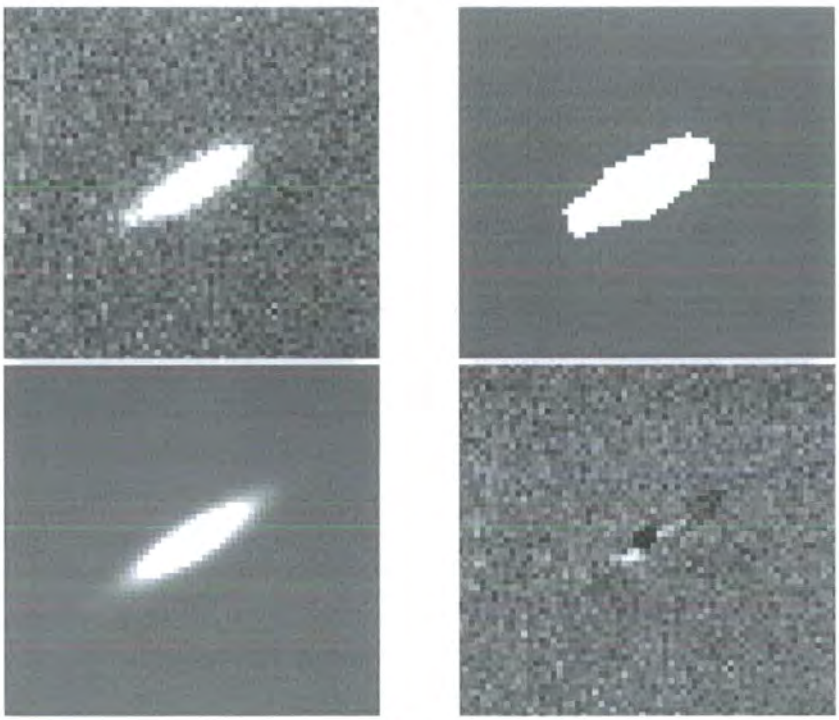

Figure 4.4: An example fit, this galaxy has B/T= 0.0. The shown are : (a) top left : the real galaxy postage stamp image, (b) top right : the segmentation mask, (c) bottom left : the model galaxy created using the best fit values and (d) bottom right : the residual postage stamp obtained by subtracting the model galaxy from the real galaxy image. The residual image is noise dominated and is indicative of a good fit.

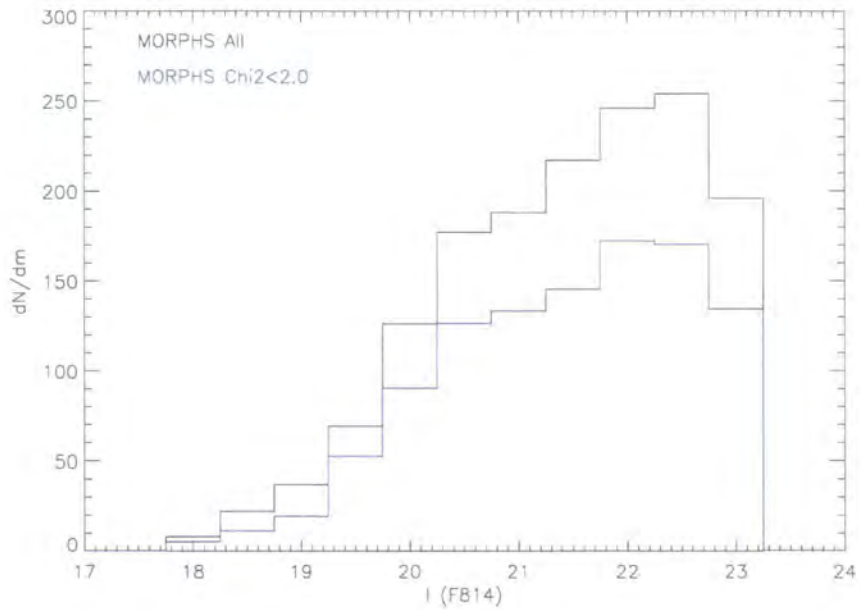

Figure 4.5: The figure shows a histogram plot of the I-band apparent magnitude distribution of 1057 MORPHS galaxies. The sample contains only galaxies with Gim2D fits that have $\chi^2_\nu < 2.0$ and have the I-band apparent magnitudes brighter than $I = 23.0$ for which the visual morphological classification is taken to be reliable (Smail et al. 1997).

of galaxies at different redshifts mean that different parts of the rest-frame galaxy spectrum is observed, a K-correction to the galaxy absolute magnitudes needs to be applied. Both R (F702W) and I (F814W) bands roughly translate into the rest-frame V-band. No evolutionary correction is applied to the galaxy absolute magnitudes since this study is mainly interested in the spiral galaxy populations for which this correction is expected to be small. The correction for the galactic reddening for the MORPHS clusters is small too and is therefore ignored (Smail et al. 1997).

The K-corrected rest-frame V-band galaxy absolute magnitudes were obtained by using a set of template $V - I$ colours appropriate to an $M_* = -21.8$ galaxy at various redshifts and for different spectral energy distributions (SED), Smail et al. (1997). This allows for a morphologically-dependent K-correction to be applied to all the galaxies. The colour correction from the V to g-band useful for later comparison with the nearby cluster data was done using the Fukugita et al. (1995) colours of galaxies at $z \sim 0$ assuming an Sbc SED. This assumption is justifiable since this study is only interested in the spiral galaxy population in clusters at intermediate redshifts.

4.3.3 WFC Revisited

In this Chapter we investigate whether the population of spiral galaxies found in the intermediate-redshift clusters could be the progenitors of the present-day cluster S0s. There are several ways the intermediate-nearby cluster comparison can be made. The reason for this is that the intermediate redshift clusters are objects that are already as evolved as the present-day Coma cluster (Dressler et al. 1997) and that these clusters are expected to eventually evolve into clusters much bigger than Coma. In the study of the morphology-density relation for the intermediate redshift clusters, Dressler et al. (1997) found local galaxy density on average to be higher than that for the nearby cluster sample (Dressler 1980b). Dressler et al. (1997) made the comparison between the nearby and intermediate cluster populations based upon the regions that overlap in the local projected galaxy density.

However, this means that galaxies nearer to the cluster edges of the intermediate redshift sample are compared with the galaxies in the more central regions of the nearby cluster sample. These intermediate redshift galaxies may in time find themselves falling into the cluster central regions but during this process their properties are very likely to change i.e. it is still not clear what the best way to make the comparison is.

For the purpose of this study we choose to compare galaxies found within a fixed physical size from the centre of the cluster. Assuming a ΛCDM cosmology and $H_0 = 50$ kms^{-1} Mpc^{-1} the WFPC2 field of view at the median redshift of the sample translates into 1.2 Mpc in physical size (c.f. 4 Mpc the field of view of the WFC at $z = 0.04$). Therefore, for the intermediate-nearby cluster comparison, the nearby cluster sample is also restricted to this physical size i.e. only galaxies confined to a box of 1.2 Mpc on a side are taken into consideration (the box is centred on the cluster centre coordinates obtained from NED). The distribution of the absolute magnitudes for this central area-selected WFC sample is shown in Figure 4.6. The figure demonstrates that the relative fraction of spiral galaxies, as well as the overall number of galaxies, has decreased but the number of cluster S0s (which are to be compared with the $z \sim 0.5$ spirals) still remains relatively large (total of 132).

4.3.4 MORPHS : Distributions

Some of the obtained galaxy structural parameters of interest for this study are presented in this section. Figure 4.5 demonstrates that the intermediate redshift sample is reasonably complete to $I = 23.0$ and that the $\chi^2_\nu < 2.0$ selection does not appear to bias the sample in this apparent magnitude regime. Figures 4.7 (a) and (b) show the distribution of the field uncorrected B/T ratios as a function of the morphological type for the $z \sim 0.5$ and nearby cluster (1.2 Mpc selected) samples respectively. The distributions reveal a large number of spiral galaxies at $z \sim 0.5$ compared to the present-day (1.2 Mpc selected) and is consistent with the differ-

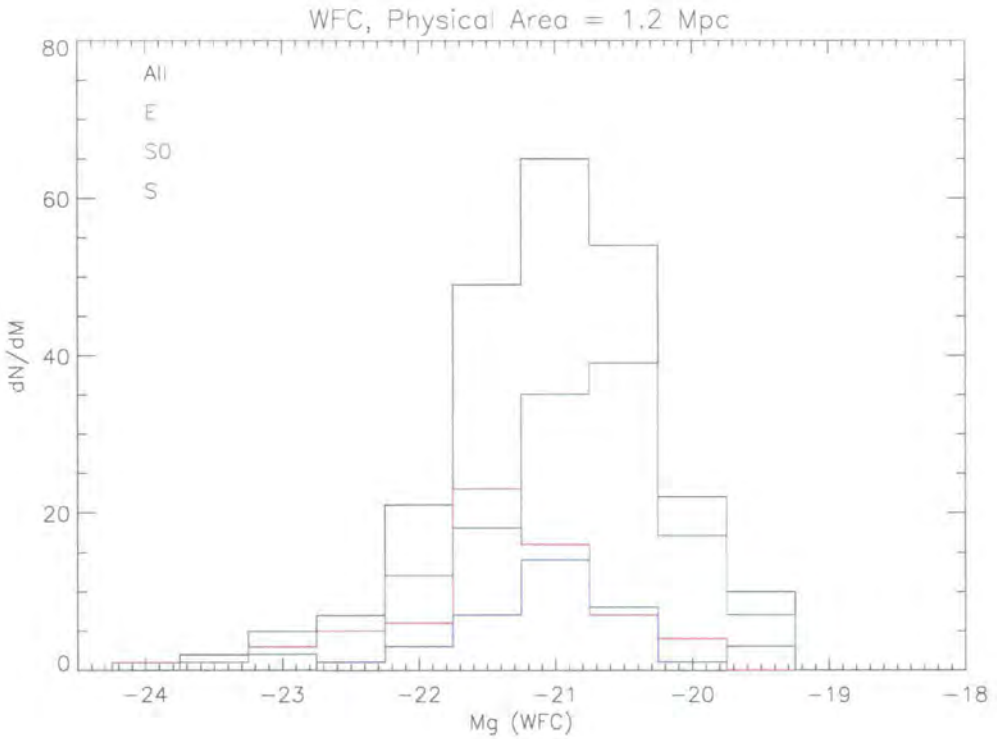

Figure 4.6: The luminosity function for the nearby cluster sample taken from the central 1.2 Mpc cluster region imaged with the WFC. The luminosity function of S0s suggests that the nearby cluster sample is fairly complete down to $M_g = -20.5$. This absolute magnitude limit is adopted in the study of the intermediate redshift cluster populations.

ence in the morphology-density relation observed by Dressler et al. (1997). It also appears that many of the $z \sim 0.5$ spirals are pure exponential disks.

4.3.5 MORPHS : Field Correction

Before further commencing this study it is important to calculate and correct for the contamination from the underlying field population. On average there are ~ 60 field galaxies per WFPC2 pointing with a rough breakdown per morphological type : E, 10%; S0, 10%; Sab, 23%; Scdm, 32% and Irr/Mer, 25%; (Smail et al. 1997). The morphological field correction was obtained using the fits to the HST Medium Deep Survey I-band number counts kindly provided by Prof. Ian Smail (private communication, and obtained using the Griffiths et al. (1994) data). The field correction is applied to the final sample of galaxies brighter than $M_g = -20.5$ which corresponds to the completeness limit of the S0 distribution of the nearby cluster data (central area-selected, Figure 4.6). Although the underlying distribution of B/T ratios as a function of morphology for the field sample is not known, this does not represent a major problem since this study is only interested in the spiral galaxy populations which are known to have predominantly low B/T ratios.

To calculate the field correction the I-band number counts were first used to calculate the fractional contribution of field galaxies to each absolute magnitude bin. For this absolute magnitude bin a distribution of B/T ratios is obtained. The assumption made here is that the field contribution is independent of the B/T distribution i.e. each B/T bin will have a fraction of field galaxies and the fractional field contribution is averaged over all the B/T bins. The excess (field) galaxies are excluded by random sampling each of the [M, B/T] bins.

4.3.6 MORPHS vs WFC : Populations Summary

Table 4.2 shows fractional contributions of the different morphological types using the defined selection criteria. The table indicates that the samples are good repre-

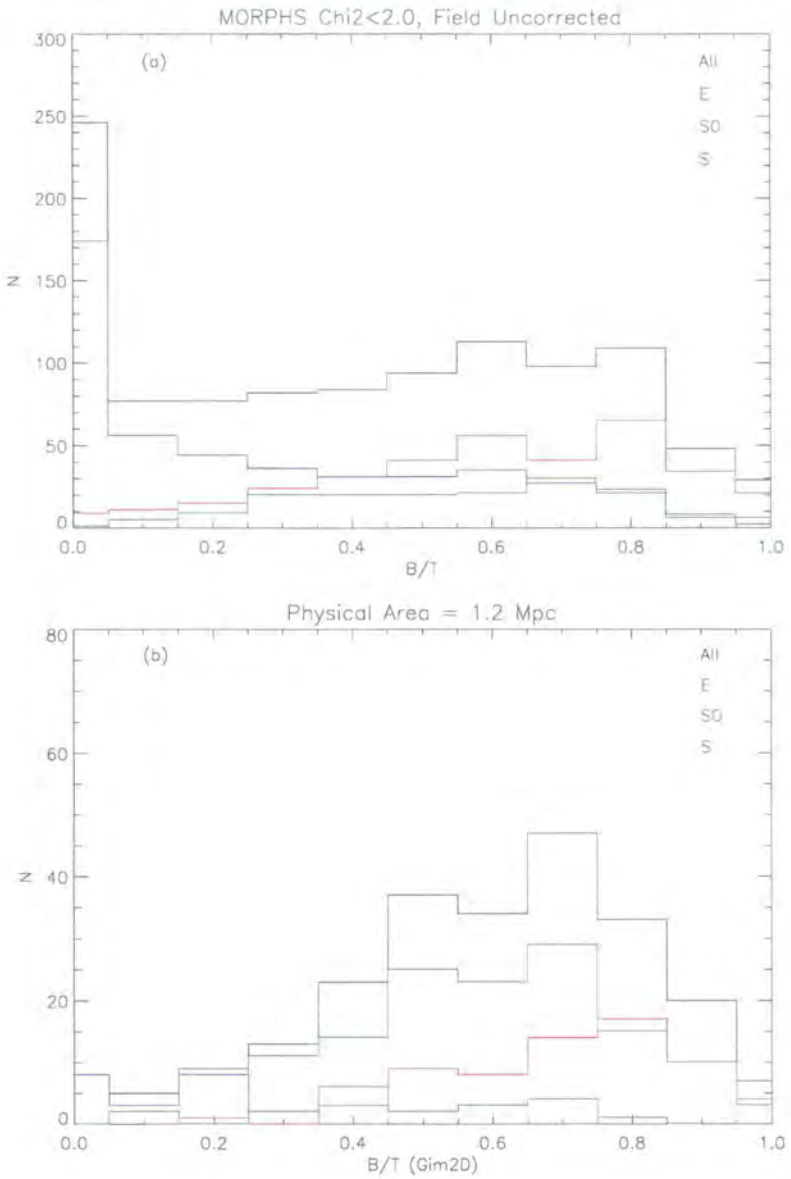

Figure 4.7: (a) The distribution of the B/T ratios for the MORPHS galaxies (black histogram). Also plotted are the distributions of the B/T ratios as a function of the morphological type visually classified as explained in Smail et al. (1997). Morphologically classified spiral galaxies (S) have predominately low B/T ratios whilst ellipticals (E) have predominately high B/T ratios. The S0 distribution spans a range of B/T ratios but is skewed towards the higher B/T values. Note that $z \sim 0.5$ clusters appear to be more spiral rich than the nearby rich clusters of galaxies (Chapter 3) reflected by the dominance of galaxies with low B/T. NB the data is not field corrected. (b) The distribution of the B/T ratios for all the WFC galaxies (black histogram). Also plotted are the distributions of the B/T ratios as a function of the morphological type visually classified as explained in Dressler (1980a) and taken from within the central 1.2 Mpc region of the nearby cluster sample. Note that most of the cluster spirals are lost due to the central region selection.

sentations of the overall galaxy populations.

Table 4.2: WFC and MORPHS Populations.

Sample	N	E(%)	S0(%)	S(%)
WFC All	1445	0.17	0.47	0.36
WFC Chi + App Mag Selected	804	0.20	0.50	0.30
WFC Chi, App Mag + Area Selected	236	0.28	0.56	0.16
WFC Chi, App/Abs Mag + Area Selected	203	0.26	0.46	0.14
MORPHS All	1541	0.34	0.14	0.44
MORPHS Chi + Abs Mag Selected	358	0.31	0.21	0.47

4.3.7 MORPHS vs WFC : Morphological B/T Distributions

The change in the galaxy structural properties between the field-corrected MORPHS $z \sim 0.5$ sample and the WFC 1.2 Mpc selected $z \sim 0$ sample is studied in terms of the B/T distributions obtained for different morphological types and down to $M_g = -20.5$. The results are plotted in Figure 4.8. The distributions appear to agree reasonably well. The relatively small number of galaxies in some bins prevents this from being conclusive. The Kolmogorov-Smirnov (KS) test shown in Table 4.3 however shows little agreement between the distributions. This arises from the KS test being dominated by the difference in the cumulative distributions.

The disagreement between the B/T distributions could be caused by the effect of seeing since the WFC PSF and the MORPHS PSF are very different with respect to the apparent galaxy size. This can be tested by investigating the ratio of the physical size of the galaxy with respect to the seeing. The results are illustrated in Figure 4.9 and suggest that most galaxies have characteristic radii that are larger than the seeing for both WFC and MORPHS samples. Therefore, the seeing does not influence the recovery of the galaxy size relative to the apparent PSF size. Fur-

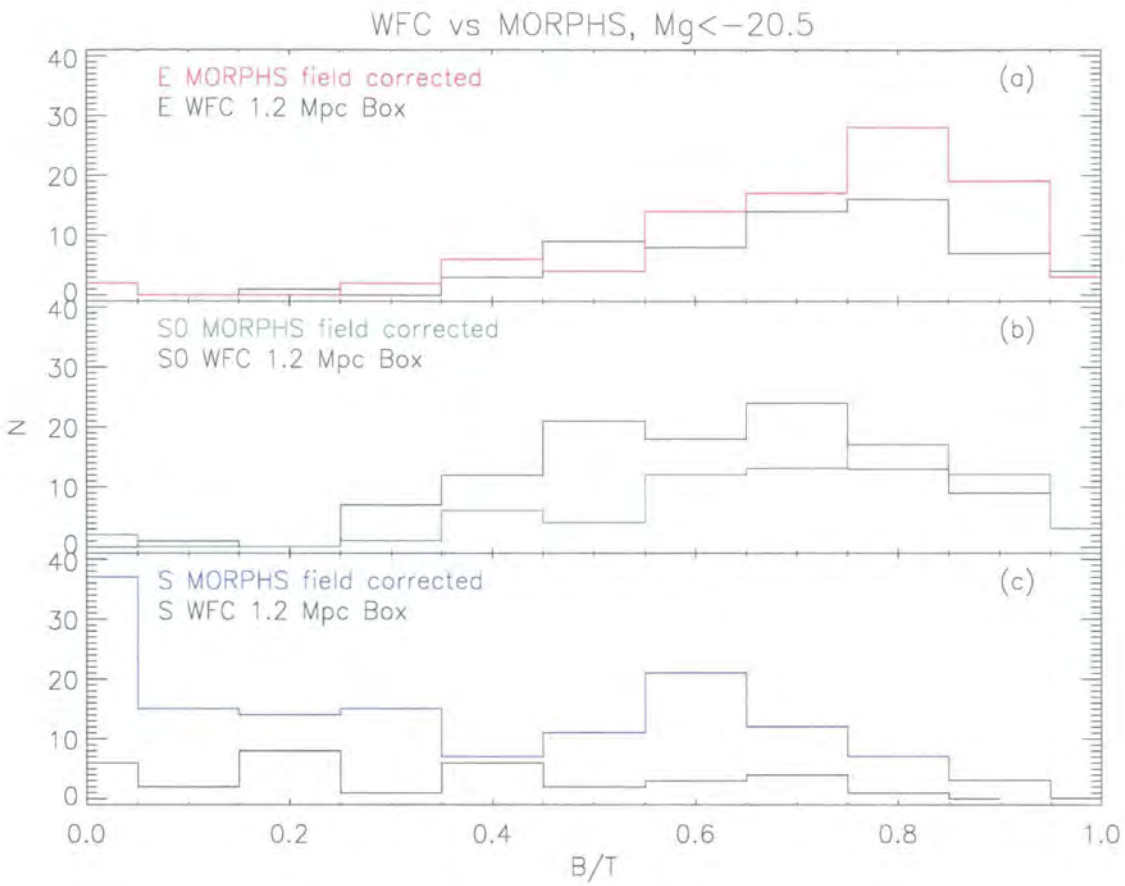

Figure 4.8: The figure shows a comparison between the field corrected B/T distributions of MORPHS spirals as a function of morphology and down to $M_g = -20.5$ and the corresponding WFC spirals. The B/T distributions do not agree well for the same morphological types observed at $z \sim 0$ and $z \sim 0.5$. The Kolmogorov-Smirnov statistics is given in Table 4.3.

Table 4.3: WFC vs MORPHS : Kolmogorov-Smirnov Statistics.

Sample WFC vs MORPHS	Maximum Deviation Between Between Cumulative Distributions	Significance Level of K-S Statistic
E	0.151783	0.33
S0	0.247619	0.01
S	0.123773	0.78

thermore, a comparison can be made between panels (a) and (b) to determine the resolution effect on the recovery of the fundamental structural properties of galaxies. It appears that eventhough the nearby sample is much closer, the PSF size is relatively large thus making the structural components of the intermediate redshift sample better resolved. This effect goes in the opposite direction of what is being questioned here - whether the resolution problems between the intermediate and nearby samples are to blame for the difference in their B/T distributions.

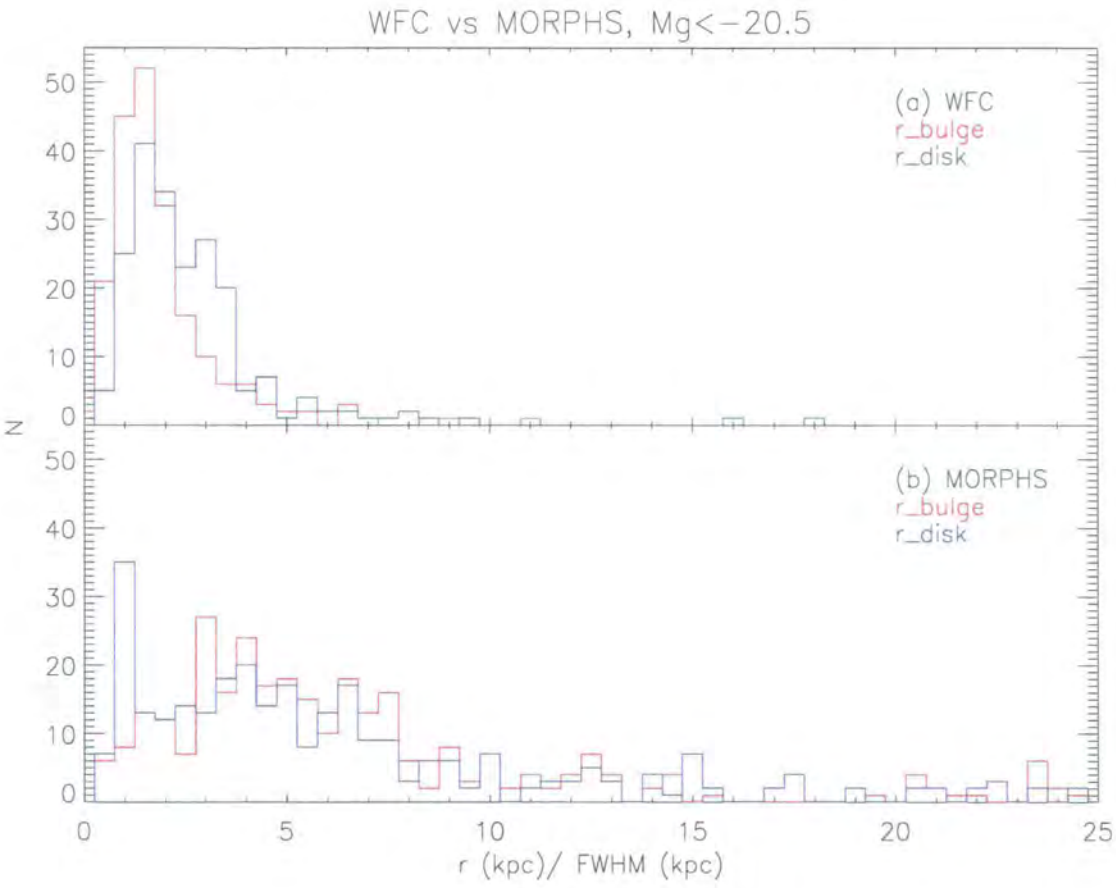

Figure 4.9: The effect of seeing/PSF on the characteristic radii measurements. The figure indicates that the seeing does not influence the recovery of the galaxy size relative to the PSF size and therefore cannot be the cause of the discrepancy between their B/T distributions.

4.3.8 Disk Fading

In Chapter 3 we showed that a 1 magnitude disk fade in the g-band is enough to bring the distributions of the B/T ratios of the nearby cluster spirals and S0s into agreement. However, it was subsequently shown that if the present-day cluster spirals are taken to be the progenitors of the present-day S0s the simple fading of the disks of the present-day cluster spirals by 1 magnitude does not reproduce the correct distribution of B/T for the present-day S0s.

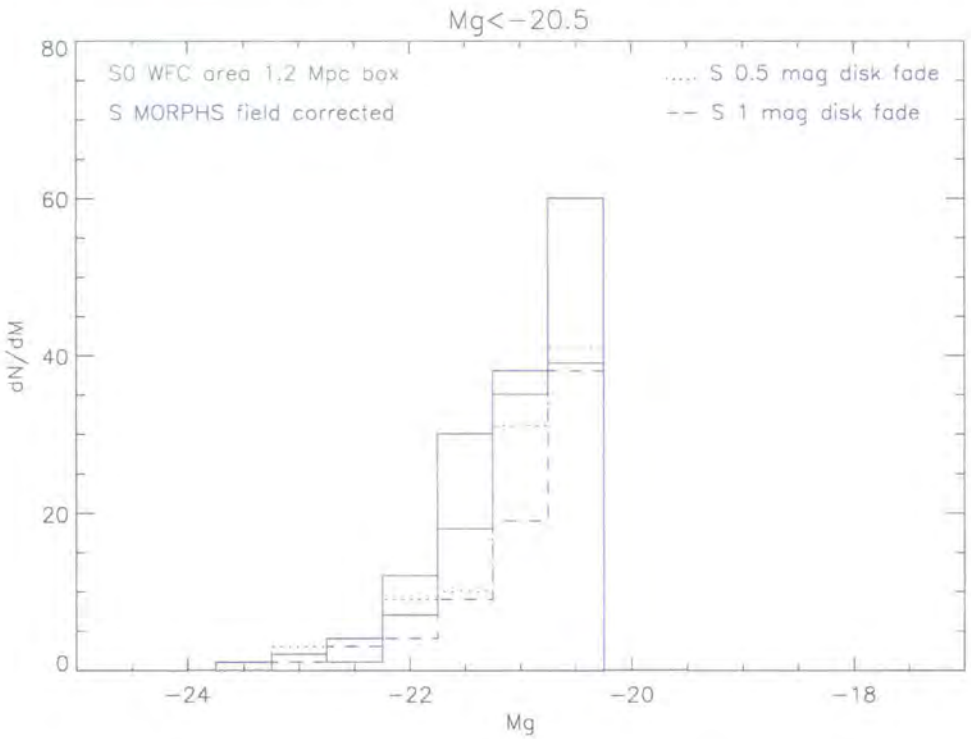

Figure 4.10: The luminosity functions of the nearby cluster sample S0s taken from the central 1.2 Mpc cluster region and the intermediate redshift spirals. The completeness limit of $M_g = -20.5$ is adopted. Also plotted are the luminosity functions of the intermediate redshift spiral galaxies after their disks were faded by 0.5 and 1.0 magnitude and the absolute magnitude selection limit of $M_g = -20.5$ imposed.

Here we propose to apply the method of disk fading to the morphologically classified spiral galaxies found in the intermediate redshift clusters to test whether these galaxies are consistent with being the progenitors of the present-day cluster

S0 galaxies as suggested by some studies (Dressler et al. 1997, Poggianti et al. 1999).

Table 4.4: WFC vs MORPHS : Kolmogorov-Smirnov Statistics.

Sample S0 WFC vs S MORPHS	Maximum Deviation Between Between Cumulative Distributions	Significance Level of K-S Statistic
original	0.50	0.000
fade=0.5	0.29	0.000
fade=1.0	0.27	0.002
fade=1.5	0.44	0.000

The luminosity functions for the 1.2 Mpc selected nearby cluster S0s and the field-corrected MORPHS spirals are shown in Figure 4.10. Also shown are the luminosity functions of the intermediate redshift spiral galaxies after their disks were faded by 0.5 and 1.0 magnitude. Figure 4.11 shows the original distribution of B/T ratios for S0 and spirals and demonstrates that the distributions of B/T ratios for S0s do not match the distributions of the spiral galaxies after their disks were faded by 0.5, 1.0 or even 1.5 magnitudes. A KS test (c.f. Table 4.4) also indicates that there is a significant difference between the B/T distribution for the S0s and all the B/T distributions for the faded spirals irrespective of the amount of disk fading (up to 1.5 magnitude). For a one magnitude fade (as suggested by the study of the nearby clusters) there still remains a significant number of pure disk galaxies not seen in the S0 population indicating that if an evolutionary mechanism is to transform the $z \sim 0.5$ spirals into present-day S0s it should act to predominantly remove the disk dominated galaxies from the nearby samples (also suggestive of some other processes being at work). However, it should be noted that there is a possibility that fading of the disk will cause some of the galaxies with brighter bulges to be classified as S0s and in extreme cases they may even be classified as ellipticals after the disk fading.

The results of the simple disk fading can also be used as a constraint to predict

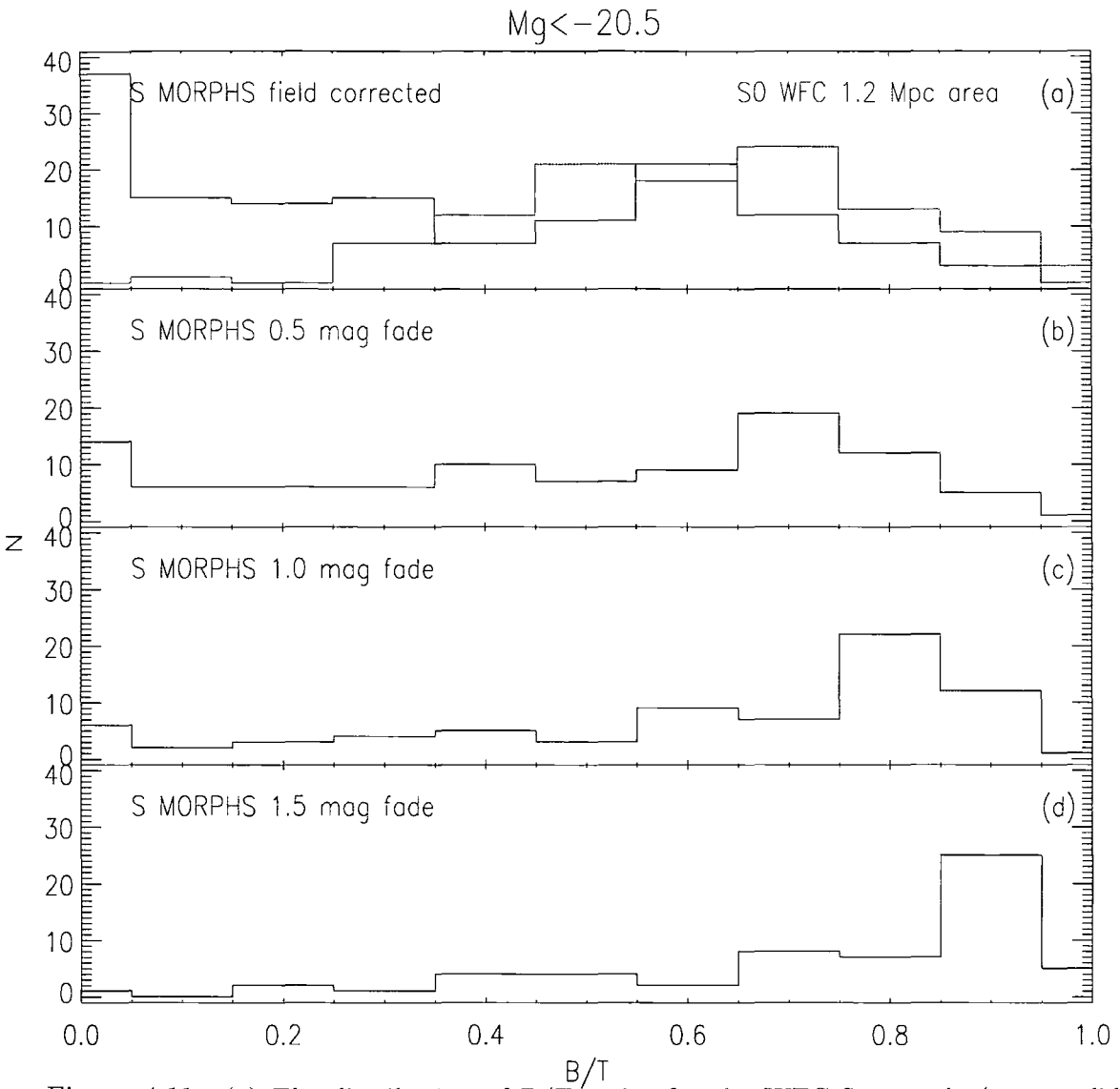

Figure 4.11: (a) The distribution of B/T ratios for the WFC S0 sample (green solid line) within the physical size of 1.2 Mpc. Also plotted is the distribution of MORPHS spirals (blue solid line) corrected for the field contamination as described in text. (b) 0.5 magnitude (c) 1.0 magnitude and (d) 1.5 magnitude disk-fade applied to the MORPHS spiral galaxies with the absolute magnitude cut of $M_g < -20.5$ retained. The Kolmogorov-Smirnov test (Press et al. 1992) indicates that there is a significant difference between the B/T distribution for S0s and the B/T distributions of all the faded spirals (Table 4.4). However, there is a possibility that fading of the disk will cause some of the galaxies with brighter bulges to be classified as S0s and in extreme cases they may even be classified as ellipticals after the disk fading.

how many spiral galaxies would have been required to populate the intermediate redshift clusters in order to produce the number of S0 that are observed today. Figure 4.12 demonstrates that, depending on the exact amount of disk fading assumed, the intermediate redshift spiral population would have to be several times higher than observed value to produce the distribution of the present-day S0s.

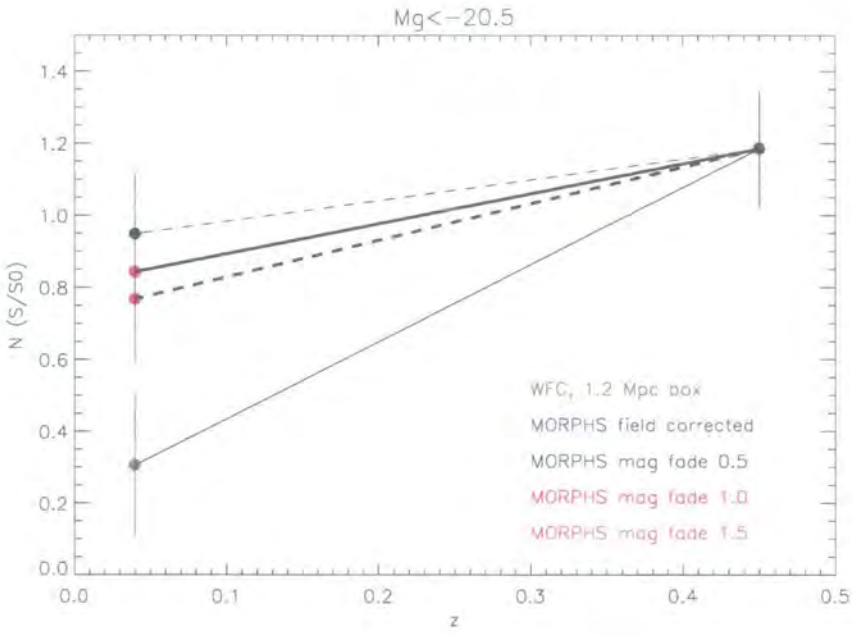

Figure 4.12: Plotted in the figure is the S/S0 ratio for the nearby cluster sample (green dot) and the intermediate redshift cluster sample (blue dot). The figure demonstrates that, depending on the exact amount of disk fading assumed (0.5, 1.0 or 1.5 magnitude), the intermediate redshift spiral population should be several times higher (black, pink and red dots) to produce the present-day S0 distribution. The error bars are obtained assuming Poisson statistics.

This result is consistent with the study by Kodama & Smail (2001) who use a simple phenomenological approach to test for a possible morphological transformation from field spirals to cluster S0s. Their study suggests that if simple disk fading methods are responsible for the spiral to S0 transformation then a large number of field spirals must have accreted onto the cluster from $z \sim 0.5$ to present. In addition most of the small bulge late type spirals must have undergone morphological changes to increase the bulge luminosity to explain the S/S0 fraction seen

in present-day clusters. These authors comment that it is plausible that the small bulge late type spirals have to be pre-processed before entering the cluster since the model suggests that the process responsible for the morphological transformation takes a relatively long time ($\sim 1 - 3$ Gyr). The hypothesis that many of the progenitors of present-day S0s have been accreted onto the clusters since $z \sim 0.5$ is broadly consistent with the large number of spirals that are required to produce the present-day S0s population according to Figure 4.12.

4.4 Summary and Conclusions

In this Chapter a study of the spiral galaxy populations in the intermediate ($z \sim 0.5$) redshift clusters has been conducted using a quantitative method of measuring galaxy bulge-to-disk ratios. The previous work of the MORPHS collaboration suggested that this spiral galaxy population might be the progenitor of the S0 galaxies found to occupy present-day clusters (Dressler et al. 1997). Motivated by the suggestion that $z \sim 0.5$ are the progenitors of the present-day cluster S0s a simple disk fading mechanism is applied to the $z \sim 0.5$ spiral population. A 1.0 ± 0.5 magnitude fade is applied to the disks of the spiral galaxies down to the absolute magnitude limit of $M_g = -20.5$ to test whether this simple mechanism can reproduce the distribution of B/T ratios observed in the nearby S0s. The results suggest that, if disk fading is the only mechanism to be acting, the population of spiral galaxies observed in the intermediate redshift clusters should be at least several times larger than the observed value. One explanation might be that the bulk of this spiral population has to be accreted onto these clusters between $z \sim 0.5$ and $z \sim 0$. Alternatively other cluster-related processes may act to remove bright disk-dominated spirals and either make them sufficiently faint to drop out of the sample or have some other means of transforming them to eventually make them evolve into galaxies that have the structural parameters similar to those of present-day S0s.

Chapter 5

Morphological Properties of Galaxies in the SDSS

In this Chapter the Fit-Galaxy code of Benson et al. (2002) is used to obtain quantitative measures of bulge-to-disk ratios for a sample of galaxies observed in the Sloan Digital Sky Survey. The quantitative bulge and disk luminosities are used to investigate the amount of baryonic matter that resides in the galaxy bulge and disk components and can be used to constrain the current theoretical models for galaxy formation and evolution.

5.1 Introduction

Our present understanding of galaxy formation comprises two main competing models both of which account for the formation of bulges in a very different way. In the monolithic collapse model bulges form during the initial collapse of a protogalaxy whilst a slow accretion of the remaining gas forms disks at later times (Eggen, Lyden-Bell & Sandage 1962). In the hierarchical galaxy formation scenario bulges are believed to form from mergers of existing galaxies with their formation still continuing into the present epoch (Barnes & Hernquist 1992). Detailed theoretical predictions for the statistical morphological properties of galaxies and their evolution have been calculated for the hierarchical scenario appropriate to the cold dark matter cosmology (Baugh et al. 1996a, Baugh et al. 1996b). The relative luminosities and stellar masses of bulges and disks are amongst the properties predicted by the models. The observed ratio of the bulge to disk luminosity density and stellar mass as measured at different absolute magnitudes and in different environments

should prove a powerful tool for constraining some of the competing models of galaxy formation and evolution.

One of the first attempts to determine the relative contributions of bulges and disks to the luminosity density of the universe was made by Schechter & Dressler (1987). This study comprised of a magnitude limited sample of $\sim$ 200 field galaxies down to $V = 16.5$ and whose bulge-to-disk ratios were obtained by visual inspection. Schechter & Dressler (1987) derived the distributions of bulge-to-disk ratios as a function of absolute magnitude for field and cluster galaxies from Dressler (1980a) and found the overall bulge-to-disk ratio to be higher in the environments of high density (i.e. galaxy clusters) than in the environments of low density (i.e. the field). For this magnitude limited sample of galaxies (whose bulge/disk decompositions were very crude but uniformly applied to both field and cluster samples) Schechter & Dressler (1987) concluded that disks appear to contribute roughly twice as much as bulges to the mean luminosity density of the universe. Since a large fraction of the disk luminosity comes from young stars whose contributions to the mean mass density is relatively small, Schechter & Dressler (1987) concluded that the relative contributions of bulge and disk components to the mean mass density of the universe are very nearly equal.

In a more recent study Benson et al. (2002) used a more quantitative method to obtain the galaxy bulge-to-total (B/T) ratios (c.f. Chapter 2). Benson et al. (2002) studied a magnitude-limited sample of $\sim$ 100 field galaxies down to $I = 16.0$ and found the luminosity functions of bulges and disks to be remarkably similar and that the bulges and disks contribute almost equally to the total stellar mass density in the universe. However, the authors do comment on large uncertainties due to the small sample size.

In this Chapter the quantitative method of Benson et al. (2002) is used to estimate the total luminosity and mass densities of bulges and disks but for a much larger sample of galaxies. The Sloan Digital Sky Survey r-band imaging (Stoughton et al. 2002) is used to implement the quantitative means developed by Benson et al.

(2002) to obtain B/T ratios for a sample of $\sim$ 9000 galaxies. Since the bulge-to-disk luminosity ratios of galaxies as a function of environment represent an important constraint on the mechanisms for the formation and evolution of bulges and disks (Schechter & Dressler 1987) the effects of the local galaxy environment on the overall derived galaxy properties will also be discussed.

Unless otherwise stated a cosmological model with $\Omega_0 = 0.3$, $\Lambda_0 = 0.7$ is adopted and the Hubble constant of $H_0 = 100$ h kms^{-1} Mpc^{-1}.

5.2 Sloan Digital Sky Survey : Data

5.2.1 Introduction

The Sloan Digital Sky Survey (SDSS) is the largest imaging and spectroscopic survey to date. The SDSS Early Data Release (EDR) was made publicly available in 2001 and comprises of a 462 square degree area imaged in five pass-bands (u, g, r, i and z) and also covered spectroscopically. The SDSS EDR galaxy catalogue is spectroscopically complete down to $r = 17.7$ with various galaxy parameter measurements readily available (Stoughton et al. 2002). The imaging data is taken with a dedicated 2.5m telescope in the drift-scan (time-delay) integration mode with an effective exposure time of 54s. The data used in this study consists of the r-band imaging frames with the bias, flat field, cosmic ray and pixel defect corrections applied (Lupton et al. 2001). Each imaging frame is a 2048 $\times$ 1489 pixel array with the pixel size of $0.394''/pixel$.

5.2.2 SDSS Apparent Magnitude Limit

The study of Benson et al. (2002) used the I-band imaging of the field galaxy sample of Gardner et al. (1996) to obtain a measure of galaxy B/T ratios. The data of Gardner et al. (1996) was obtained to study the K-band luminosity function which is not ideal for studying B/T ratios since the K-band selected galaxies are biased towards old, evolved stellar populations. However, Benson et al. (2002) have shown that the data can be used to reliably recover B/T ratios for galaxies brighter than

$I_{Gar} = 16.0$ with the recovered B/T accuracy of $\sigma_{rms} \sim 0.1$.

The SDSS imaging is taken with a larger telescope but using shorter exposure times than that of Gardner et al. (1996). To match their signal-to-noise ratios we calculate that this produces a change in the apparent magnitude of $I_{SDSS} - I_{Gar} = 0.4$ down to which the decomposition code is taken to be reliable*. Using the mean galaxy colours of Fukugita et al. (1995) the transformation between the I_{SDSS} and r bands is $r - I_{SDSS} = 0.9$ making the total difference equal to $r - I_{Gar} = 1.3$ magnitude. The first galaxy selection criteria is therefore set to $r \leq 17.3$ and is based upon the limiting apparent magnitude for the reliable bulge-to-disk decompositions (Benson et al. 2002).

5.2.3 SDSS Data Selection and Galaxy Catalogue

The SDSS EDR equatorial strip observations of galaxies with $r \leq 17.3$ are shown in Figure 5.1 and colour coded according to the different SDSS runs (94, 125, 752 and 756). The black points represent all the imaging taken in 'poor' seeing conditions ($PSF_{FWHM} > 1.55''$). The seeing value at the time of observation sets the second galaxy selection criterion since for reliable bulge-to-disk decompositions the seeing should be less than a typical galaxy half-light radii (Beijersbergen et al. 1999).

The final galaxy selection criterion is based on redshift. To avoid the uncertainties in the redshift measurements due to the local galaxy infall a low redshift cut ($z = 0.02$) is imposed while the high redshift cut is imposed because of the tail-down in the redshift distribution for the total SDSS galaxy sample at $z = 0.3$.

In summary the SDSS EDR galaxy selection criteria used in this study are :

- included are all the SDSS EDR galaxies with the r-band magnitudes $(r - r_{redd}) \leq 17.3$, where r_{redd} is the correction for the Galactic extinction,
- seeing $< 1.55''$, and,
- $0.02 < z < 0.3$.

*The change in the apparent magnitude is governed by the change in the signal-to-noise ratio.

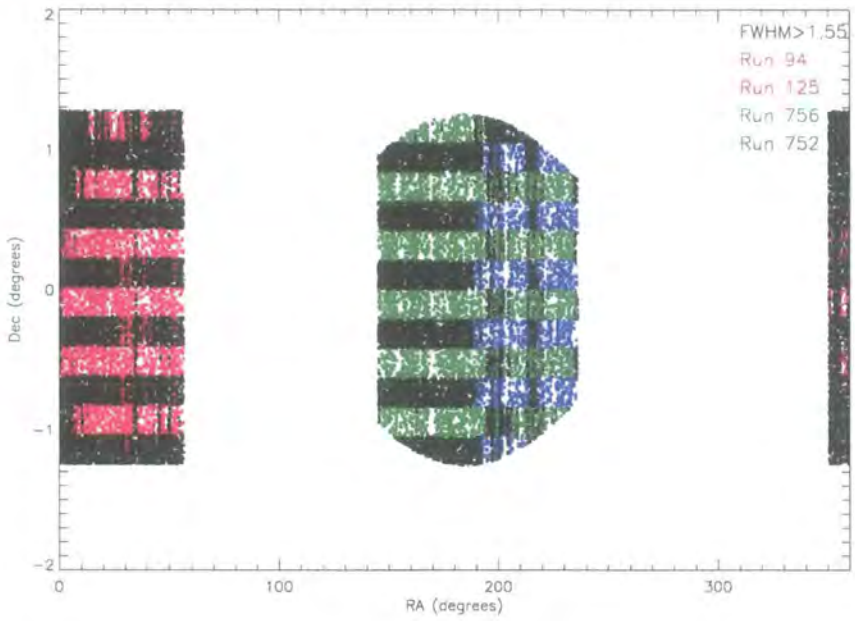

Figure 5.1: SDSS galaxies that meet the defined selection criteria. Black points correspond to all galaxies whose seeing is greater than 1.55″.

The selection leads to a total of 8839 SDSS EDR galaxies whose relevant SDSS pipeline measured parameters (Lupton et al. 2001) were extracted and catalogued. Some of the catalogued parameters are summarized in Table 5.1 and their relevance explained in a little more detail below :

- Galaxy and Run ID's. Necessary to identify the CCD frames that contain galaxy/galaxies of interest,
- Right Ascension and Declination (degrees). Used to identify the catalogued galaxies within a given CCD frame,
- Petrosian magnitudes (u, g, r, i and z bands) and Petrosian radii (R_P, seconds of arc, r-band only) as defined in Appendix A.2. The magnitudes are used to infer galaxy colours and the radii are used to define the postage-stamp size for a given galaxy (see Chapter 2, Section 2.2.1),
- Reddening (u, g, r, i and z bands). Used to correct the Petrosian magnitudes for the Galactic extinction,
- Redshift. Used in computing absolute magnitudes,

- Average CCD Gain. Used by the decomposition routine, and,
- Seeing (the mean value of stellar FWHM in seconds of arc, r-band only). The Fit-Galaxy code uses this value as the initial estimate of the seeing parameter.

Table 5.1: A sample of the main catalogue parameters.

ID	RA (deg)	Dec (deg)	$r_P - r_{redd}$	$R_P('')$	$FWHM('')$	z
100	2.6311	-0.0429	17.24	8.9	1.5	0.039
101	2.6639	-0.0529	14.36	14.9	1.5	0.039
102	2.3471	-0.0561	16.99	4.3	1.4	0.076
103	2.3398	-0.0704	16.68	11.9	1.4	0.058
104	2.2699	-0.0005	16.90	8.0	1.4	0.085
105	2.2338	-0.1939	16.31	6.8	1.4	0.138
106	2.3138	-0.1303	16.87	4.8	1.4	0.116
107	2.1515	-0.0513	16.48	9.3	1.4	0.076
108	2.0482	-0.0493	17.09	4.3	1.4	0.101
109	2.0822	-0.0007	17.20	3.9	1.4	0.079
110	2.1158	-0.0005	16.99	3.3	1.4	0.158

5.2.4 Object Detection and Astrometry

The object detection was performed using SExtractor v.2.2.2 software (Bertin & Arnouts 1996). The SExtractor world coordinates of the object centroid positions (x, y) were used to identify the catalogued galaxies within the SDSS frames. The Fit-Galaxy code (Chapter 2, Section 2.2.3) was run on the extracted postage stamps whose size was set equal to $(2 \times R_p) \times (2 \times R_p)$ large enough to contain many background pixels but sufficiently small to ensure a reasonable run-time (c.f. Chapter 2). Prior to decomposition the SExtractor estimate of the local sky background was subtracted from every postage-stamp to ensure the background level was close to zero (c.f. Chapter 2). The subtracted SExtractor estimate of the local sky background is kept in a file as a necessary ingredient to be used in the galaxy decomposition by Fit-Galaxy.

5.2.5 SDSS Point Spread Function

Before commencing the decomposition procedure we need to ensure that the PSF analytic model assumed by the Fit-Galaxy code (Chapter 2, Section 2.2.3) is a realistic representation of the SDSS PSF.

To demonstrate that the SDSS stars are well represented by the analytic Moffat profile assumed by the Fit-Galaxy code IRAF task IMEXAMINE was used to fit radial Moffat profiles to a sample of stars imaged on different SDSS frames and at different positions within every frame. Figure 5.2 shows radial fits (solid line) to stellar light profiles (points) obtained using $\beta = 4.5$ and demonstrates a Moffat star with $\beta = 4.5$ to be a good analytic representation of the SDSS PSF. Unfortunately most of the galaxies were fit assuming $\beta = 2.5$ since the β-parameter fine-tuning was done only after most of the galaxies were run through the decomposition algorithm. To quantify how much this affects the recovery of the B/T ratios a sample of galaxies were re-fit with the Moffat PSF with $\beta = 4.5$. The correlation between the recovered B/T ratios is shown in Figure 5.3 and demonstrates a good recovery of the B/T ratios for the two different values of Moffat β. The correlation has $\sigma_{rms} = 0.05$ and a Spearman rank correlation coefficient of 0.94.

PSF Variation

The Fit-Galaxy code assumes the starting value for the PSF to be equal to the SDSS measured value for the seeing and allows the value to fluctuate by $\pm 5\%$ (Chapter 2, Section 2.2.3). The $\pm 5\%$ variation is obtained from the mapping of the seeing across a typical SDSS frame as shown in Figure 5.4. The figure demonstrates that for stars imaged at various positions of a given SDSS frame the FWHM does not change by more than $\pm 5\%$. The allowed small change in the seeing ensures that the Fit-Galaxy code can find the representative value for the seeing at the galaxy position.

However, it is important to test how consistently the Fit-Galaxy code recovers

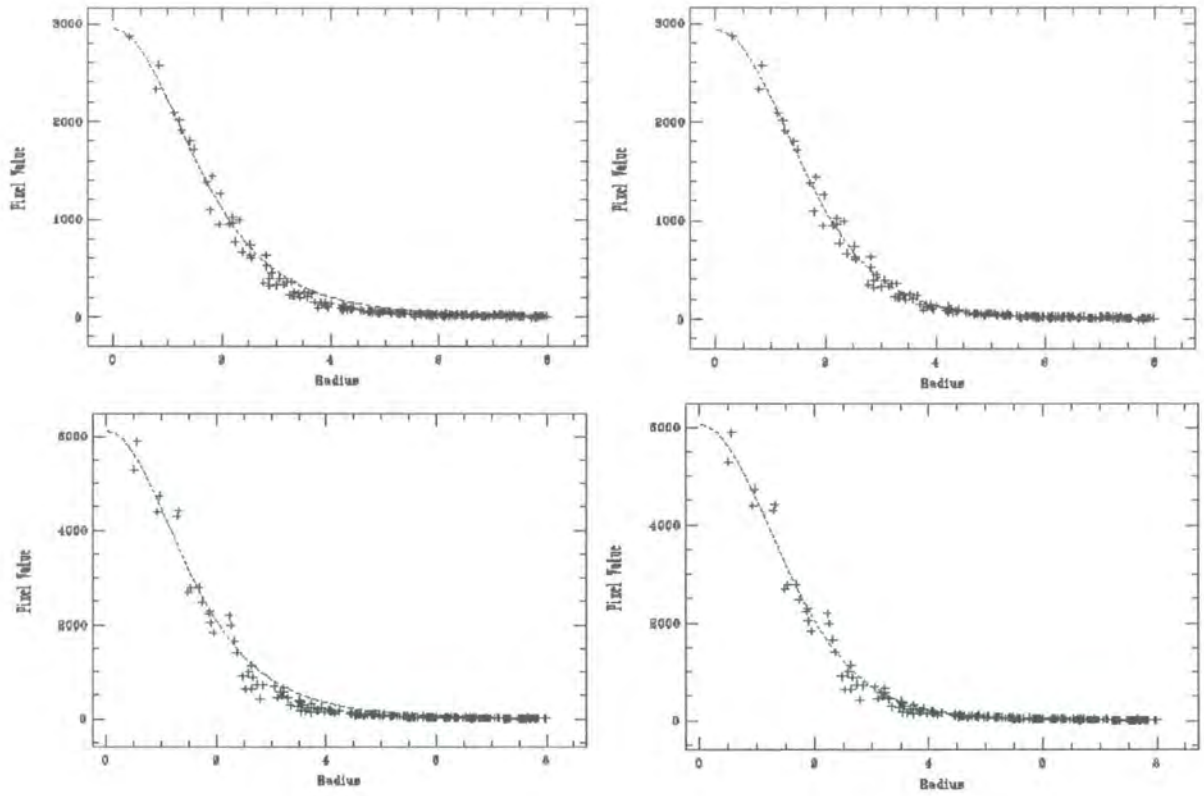

Figure 5.2: The radial Moffat profile fits to the real SDSS stars found at various positions within several SDSS frames. Left : fits to stellar profiles using $\beta = 2.5$. Right : fits to stellar profiles using $\beta = 4.5$. The stars appear to be better represented by the assumed analytic profile when $\beta = 4.5$. Radius is in pixels and Pixel Value in counts.

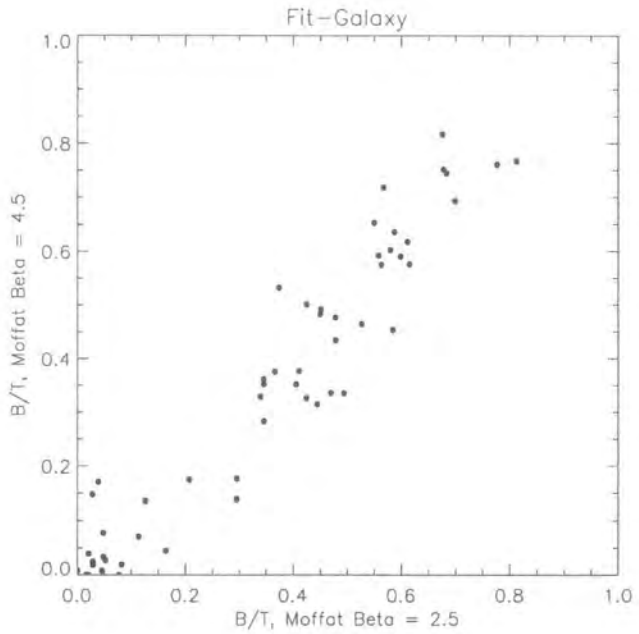

Figure 5.3: The B/T ratios obtained when the Moffat parameter β is set to $\beta = 2.5$ and $\beta = 4.5$. The scatter is less than the typical expected B/T error (Chapter 2) implying that using $\beta = 2.5$ will not have much of an effect on the recovered B/T ratios. The Spearman rank correlation coefficient of 0.94 indicates a significant correlation.

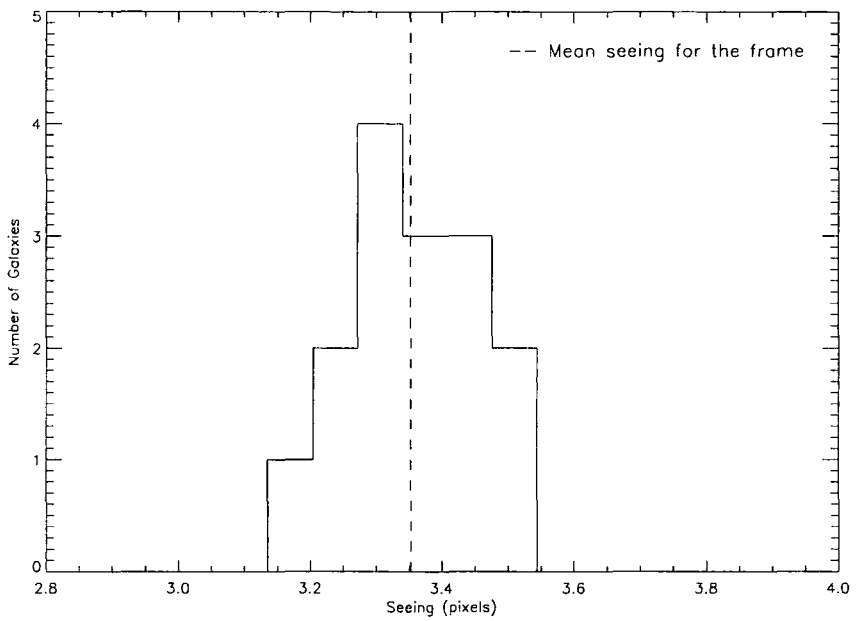

Figure 5.4: The variation of the PSF across an SDSS frame. The dashed line represents the mean value of seeing for the frame. The seeing appears not to vary by more than $\pm 5\%$ from the mean value. A similar inspection of other frames showed this to hold in general.

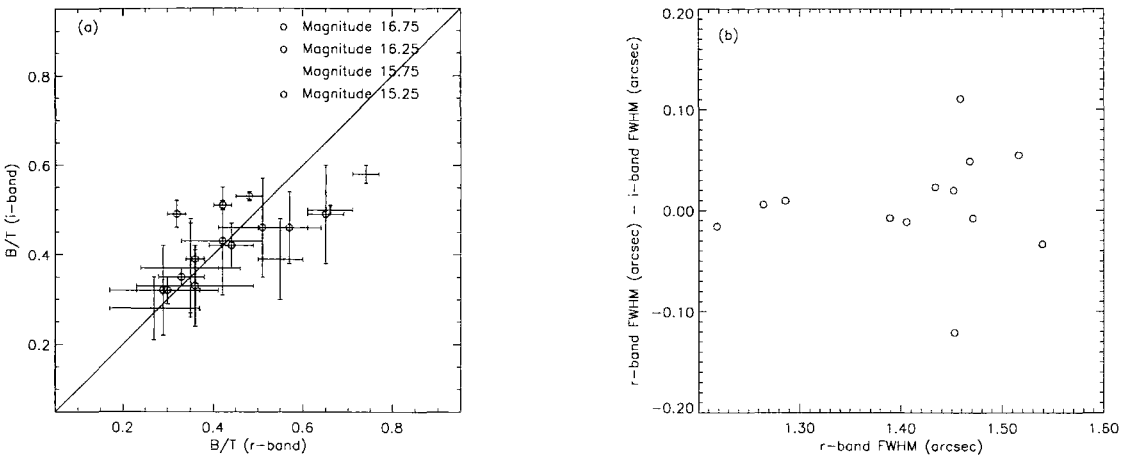

Figure 5.5: (a) Correlation between B/T ratios obtained for same galaxies in r and i bands. This correlation demonstrates that B/T are accurately determined for different representative PSFs and across the apparent magnitude range. The recovered B/T ratios show no obvious dependence on galaxy apparent magnitudes indicating that the decompositions are not affected by the change in the signal to noise ratio. (b) The difference in the output Fit-Galaxy seeing for same set of galaxies observed in r and i bands and demonstrates that the Fit-Galaxy code appears to recover the representative PSF for a given galaxy well and without biasing the recovered B/T ratios.

the 'correct' representative PSF for a given galaxy and quantify the effect in terms of the recovered B/T ratios. The observed galaxy properties are expected to vary little between the r and i bands but the PSF signatures associated with these observations will be somewhat different. Figure 5.5 shows a good correlation between the B/T ratios obtained for the same set of galaxies imaged in the two bands. The code does appear to find consistent B/T ratios across a range of apparent magnitudes and independent of seeing. Error bars are obtained form 30 Monte Carlo realizations of each of the model fits.

5.3 SDSS : Fit-Galaxy Decompositions and Galaxy Morphologies

5.3.1 Fit-Galaxy Decomposition Outputs

Figure 5.6 demonstrates a typical fit to a galaxy light profile. The figure shows the postage-stamps of a real galaxy, a noise-free model generated from the best-fit parameters along with the individual model disk and bulge components. If the model is a good representation of the data the reduced χ^2 is expected to be $\chi^2_\nu \sim 1.0$ (Appendix B). In this study a galaxy is taken to be sufficiently well represented by the model if $\chi^2_\nu < 2.0$ and if there are no obvious structures left in the residual image. An example of a well fit galaxy is shown in Figure 5.7. The cross-hatched areas represent potential contaminations from overlapping objects as determined by the Fit-Galaxy masking procedure (5σ detection above the sky background) and are excluded from the fitting. The inset in Figure 5.7 shows a histogram of $dP/d(B/T)$ - the distribution of the bulge-to-total ratio from 30 Monte Carlo realisations with the vertical dashed line indicating the best-fit B/T value for this galaxy.

5.3.2 Code Speed Limitations and Galaxy Binning

The Fit-Galaxy code is not very time efficient since the number of parameters used in the minimization routine is large (c.f. Chapter 2). However, since galaxy decompositions were run as a set of serial jobs on the Durham 64-node CDML cluster[†] this improved time to process the full data-set. The run-time is also strongly dependent on the size of the galaxy postage-stamp. A 31×31 pixel image is typically fit in several minutes but as the postage-stamp increases to 91×91 pixels the typical fitting time increases to several hours. Thus fitting any galaxy whose postage-stamp exceeds this value becomes a major problem in terms of the computing time.

The SDSS galaxy sample contains less than 200 galaxies whose postage-stamp size exceeds 91 pixels on a side. To reduce the decomposition run time these large

[†]Please see http://icc.dur.ac.uk/Computing/CDMLCluster/CDMLCluster.html for the CDML cluster node specifications.

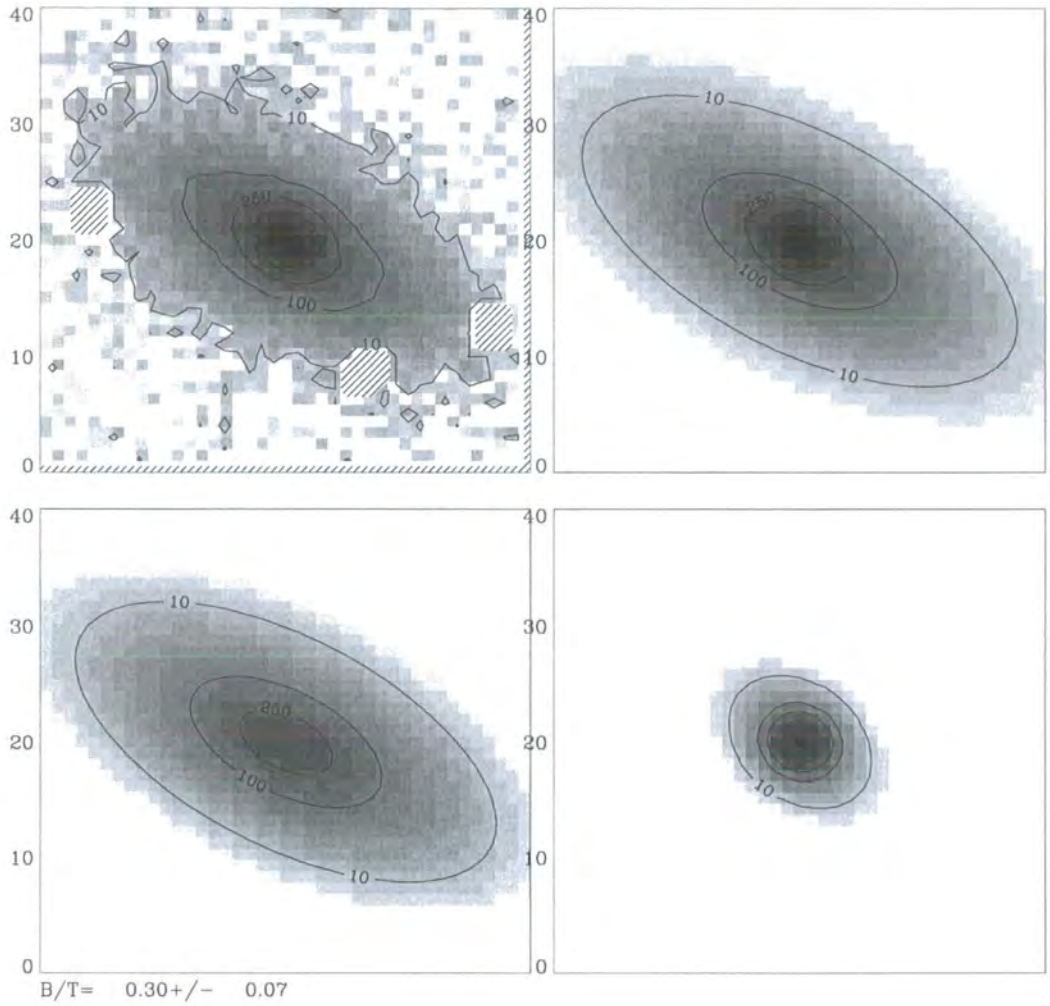

Figure 5.6: Top: Real (left) and model (right) images. Bottom: Disk (left) and bulge (right) component fits. The cross-hatched regions represent potential contaminations from overlapping objects and are excluded from the fitting. The contours indicate the pixel values in ADU.

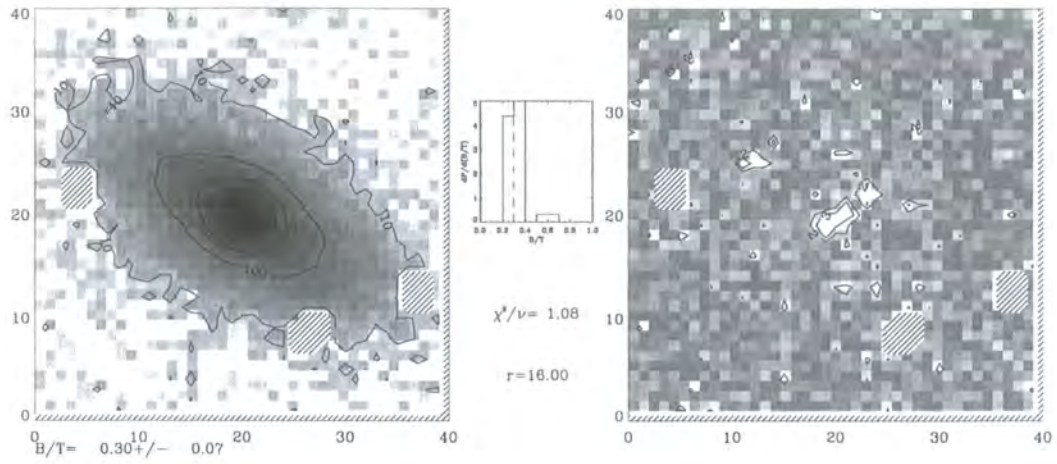

Figure 5.7: Real (left) and residual (right) images. The inset shows the distribution of B/T ratios from 30 Monte Carlo realisations with the vertical dashed line indicating the best-fit B/T. The value of χ^2_ν is acceptably small with the residual image also showing a good fit to the data.

postage-stamps are binned 2×2 which also ensures that the large nearby bright galaxies are sampled at the resolution comparable to the resolution of the more distant members. However, to make sure that the galaxy binning does not lead to an incorrect recovery of the galaxy B/T ratios a series of tests was conducted as discussed next.

To test the reliability of the method, several model galaxies were created using the standard procedure (Chapter 2, Section 2.3.3) and decomposed. Prior to decomposition the model galaxies are binned using the IRAF task BLKAVG and the Fit-Galaxy code was used perform the fitting ensuring that the pixel for the binned image is set to $2\times$ the normal pixel size ($2 \times 0.396''$) and that the noise properties in this 'super-pixel' were changed appropriately. Figures 5.8 and 5.9 show fits to model galaxies created using the exponential disk and $r^{1/4}$ laws after the original model images were binned by 2×2. In the case of the pure exponential galaxy the fit to the model is perfect. The fit to the pure $r^{1/4}$ galaxy, however, shows a similar bias seen in the unbinned model galaxies (Chapter 2) as suggested by the low value of the recovered B/T= 0.8 and implies that the binning in itself

is not responsible for the observed B/T bias. The 2×2 binning was therefore applied to all the SDSS galaxies whose postage-stamps are greater than 91×91 pixels.

The binning seems to work very well if the binned galaxy does not appear to exhibit very much internal structure (such as the model galaxies). However, for a galaxy which exhibits a significant internal structure a fit with $\chi^2_\nu > 2.0$ is more typical. Whether decomposing such galaxies even when unbinned would lead to a good fit is somewhat unclear and is demonstrated in Figures 5.10 and 5.11. The top images in both figures show the residuals of the unbinned galaxy of size 101×101 pixels whose postage stamp has been cut by 5 pixels on either side to allow for a reasonable computing time. The bottom images correspond to the residual images of the binned versions of the same galaxy. The galaxy in Figure 5.10 appears to exhibit a lot more internal structure than the galaxy in Figure 5.11 as is clearly indicated in terms of both the recovered χ^2_ν and the residual image. This supports the claim that galaxies which exhibit internal structure are poorly fit irrespective of whether they are binned or not. The recovered B/T ratios for the unbinned and binned data do appear to be different but the observed B/T difference lies within the typical error estimate for the B/T ratios. We can therefore conclude that the B/T distribution of the final SDSS galaxy sample, which contains the decompositions from the binned data, will not be biased by the binning of these big, bright nearby objects (most of which are expected to contribute to the faint-end of the luminosity function - see Section 5.4).

5.3.3 SDSS Data and the Goodness-of-Fit

The selected SDSS sample of 8839 galaxies is too large for each of the residual images to be inspected by eye to ensure a satisfactory decomposition as suggested by the $\chi^2_\nu < 2.0$. However, a randomly selected sample of galaxy residuals were eye-examined to ensure that they indeed are predominately noise-dominated. The $\chi^2_\nu < 2.0$ criteria was therefore adopted to define a 'well-fit' data set of a total of 7493 galaxies. To ensure that no selection biases are introduced by the rejection of galaxies with $\chi^2_\nu > 2.0$ the basic distributions for these galaxies are studied as a

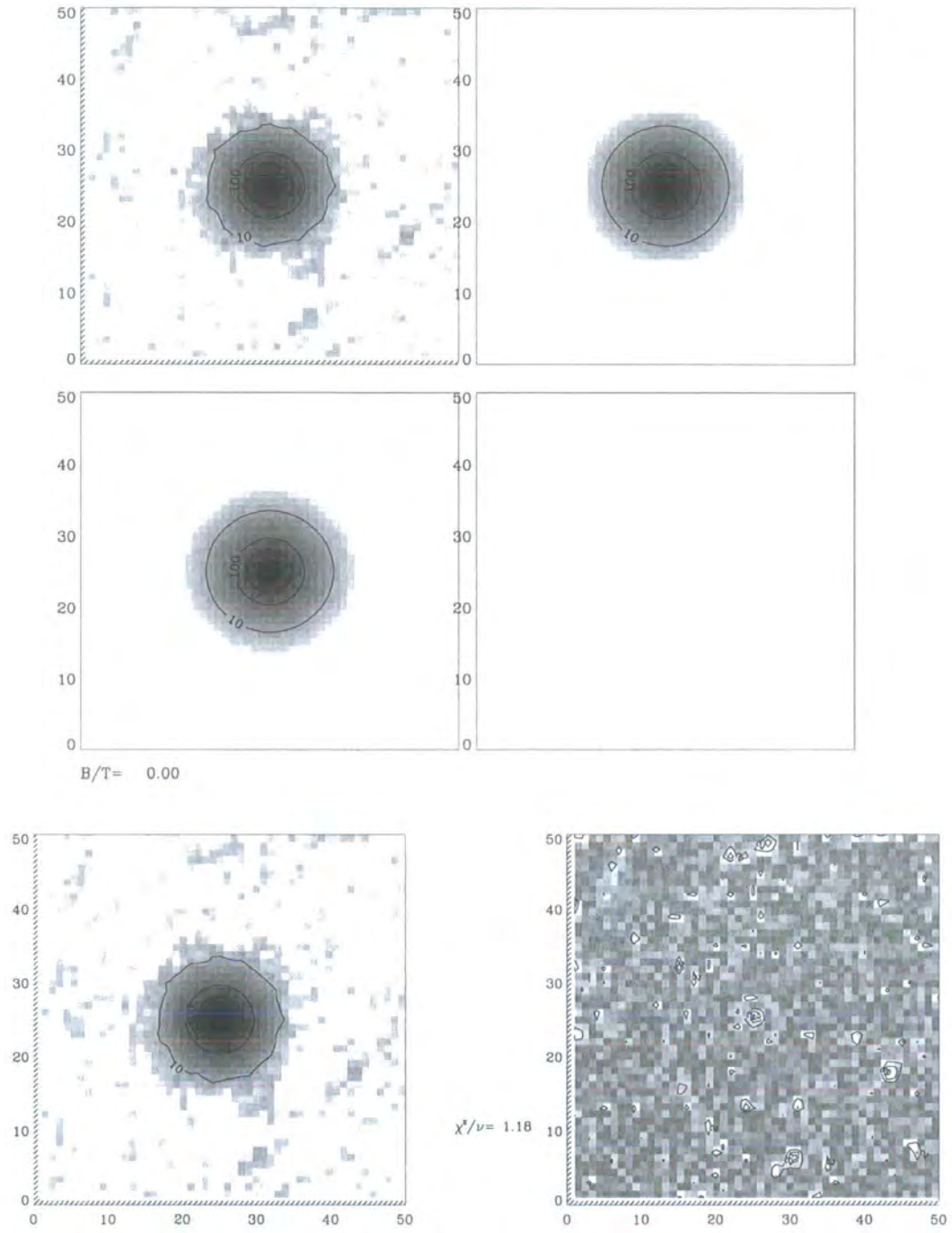

Figure 5.8: Fit to a pure exponential model galaxy after the original 101 × 101 model image is binned 2×2. The recovered B/T= 0 and it also corresponds to a pure exponential galaxy. The good fit is inferred from both the $\chi^2_\nu \sim 1$ and the noise-dominated residual image.

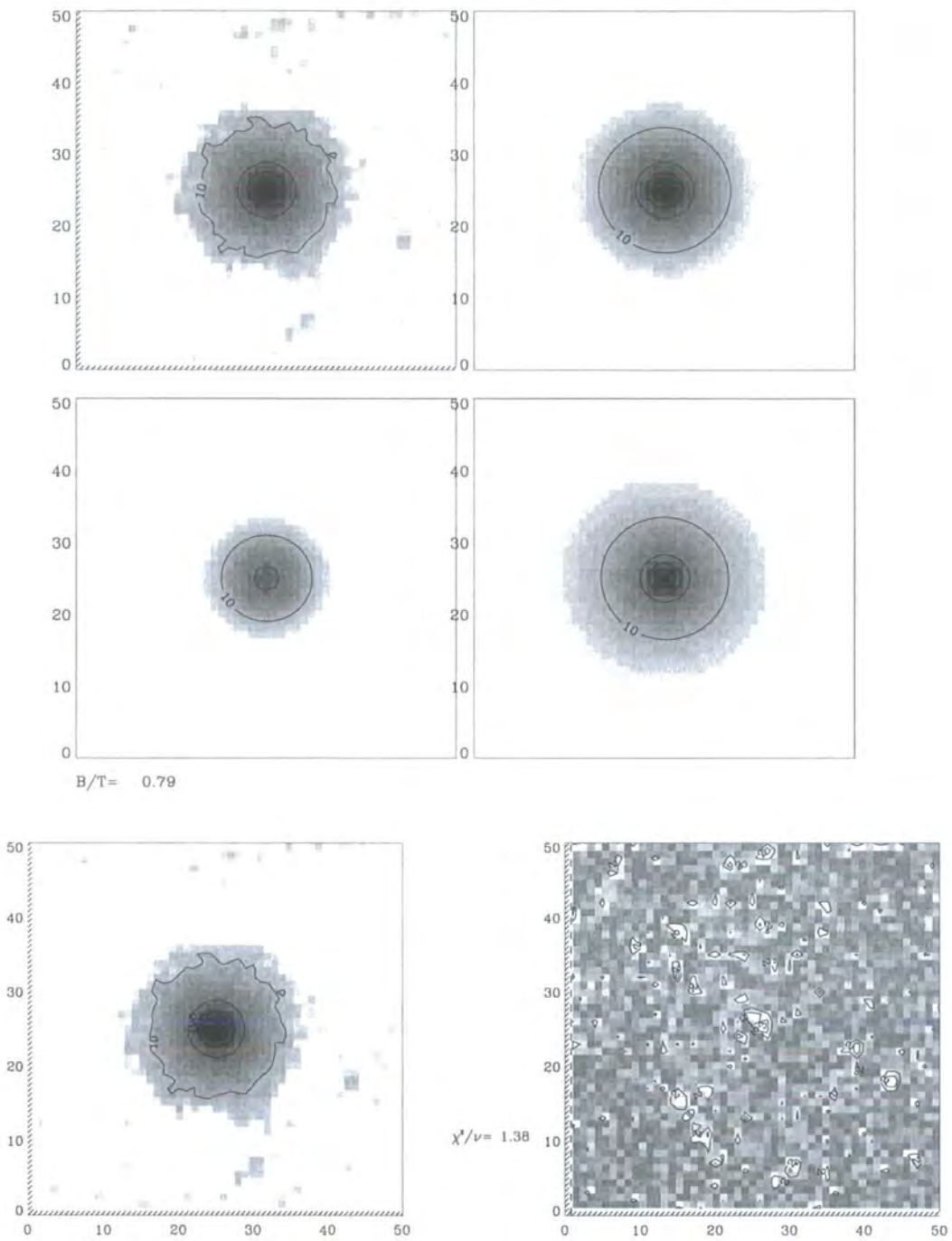

Figure 5.9: Fit to a pure $r^{1/4}$ model galaxy after the original 101×101 model image is binned 2×2. The recovered $B/T = 0.8$ again shows the Fit-Galaxy code to be biased to lower values of B/T. The good fit is inferred from both $\chi^2_\nu \sim 1$ and the noise-dominated residual image.

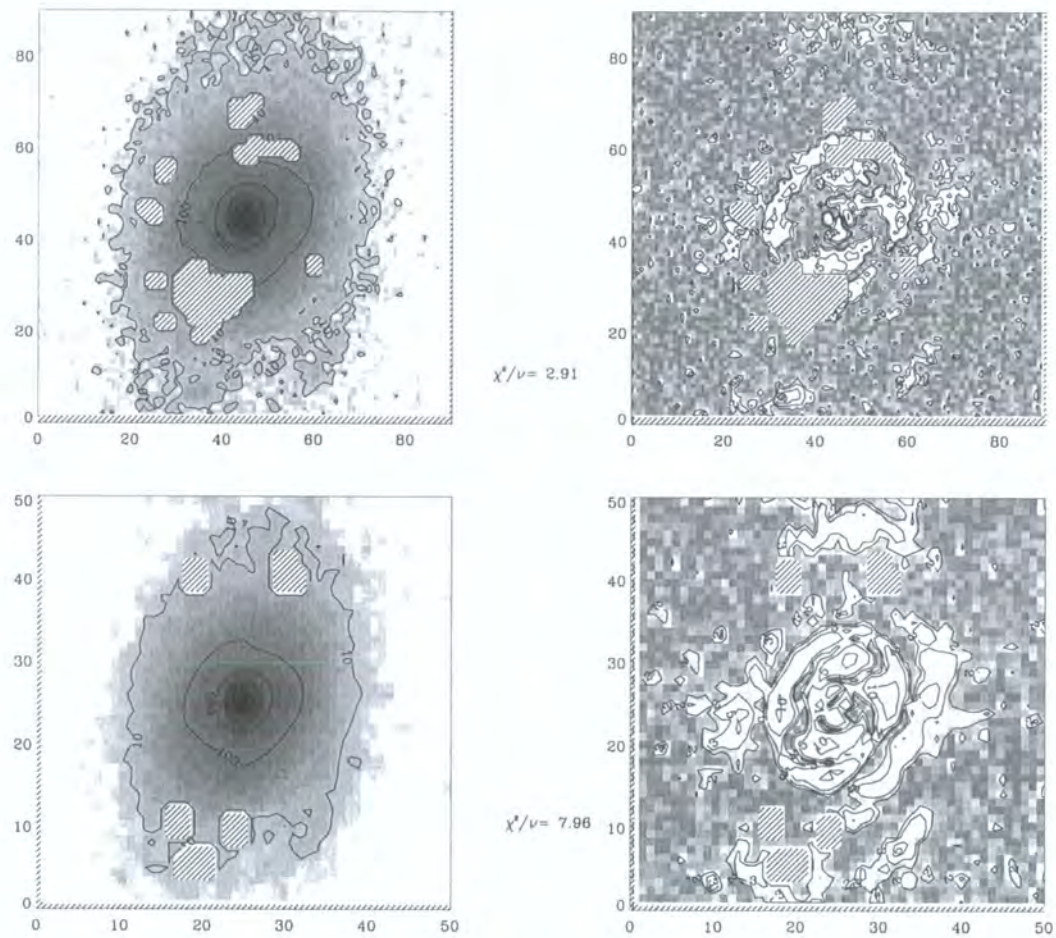

Figure 5.10: The figure shows fits to a galaxy which exhibits internal structure. The top images show the unbinned galaxy postage-stamp (left) and the corresponding residual image (right). The bottom images show the galaxy and the residual after the galaxy is binned 2×2. In both cases the recovered χ^2_ν is poor ($\chi^2_\nu > 2.0$) and residuals are not just noise-dominated. This supports the claim that internally structured galaxies result in poor fits irrespective of whether they are binned or not.

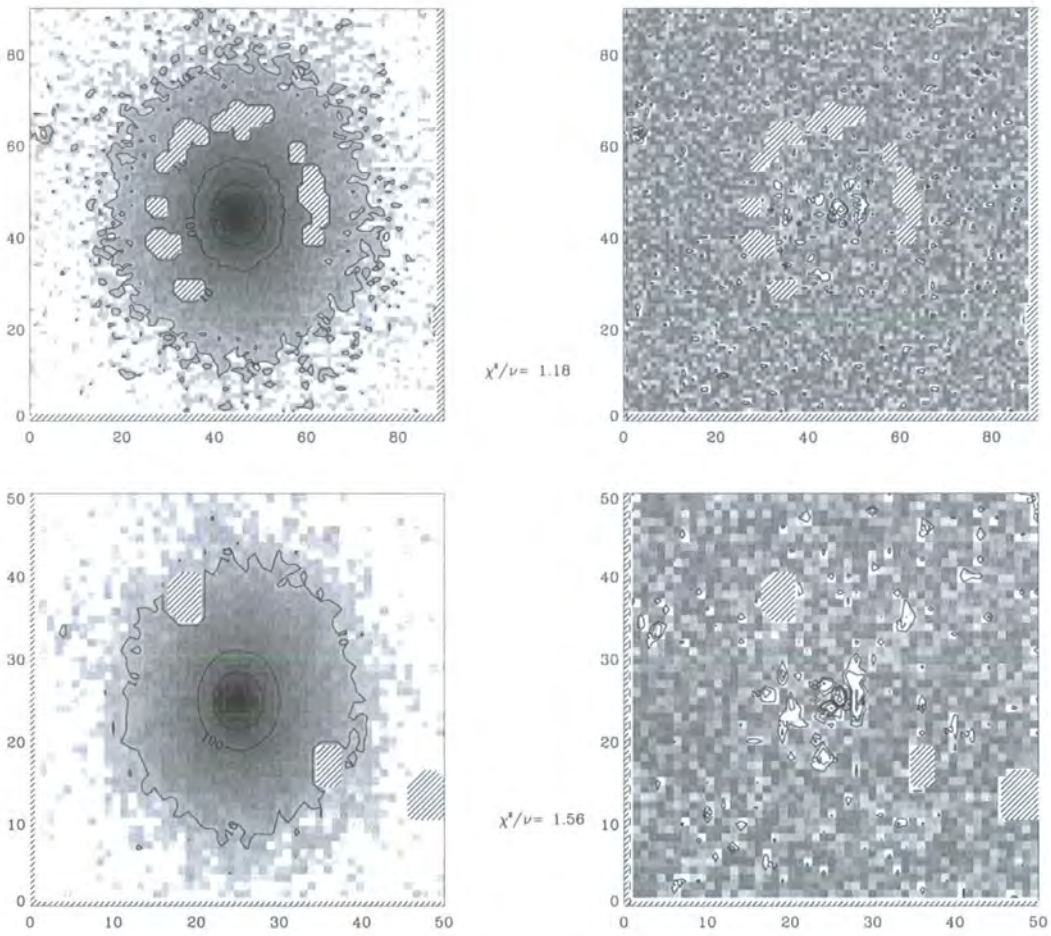

Figure 5.11: The figure shows fits to a galaxy which does not appear to exhibit internal structure. The top images show the unbinned galaxy postage-stamp (left) and the corresponding residual image (right). The bottom images show the galaxy and the residual after the galaxy is binned 2×2. In both cases the recovered χ^2_ν is good ($\chi^2_\nu < 2.0$) and residuals are noise-dominated. This supports the claim that internally non-structured galaxies result in acceptable fits irrespective of whether they are binned or not.

function of the goodness-of-fit as shown in Figure 5.12. Also plotted in Figure 5.12 is the redshift distribution and the distribution of the recovered B/T ratios. Figure 5.12 demonstrates a clear deficit of pure elliptical or bulge-dominated systems and there also appears to be a general lack of objects with $B/T > 0.7$. This is most likely due to the bias in the Fit-Galaxy code acknowledged to be present in Chapter 2. The significance of this bias and its influence on the final results will be addressed at the end of this Chapter.

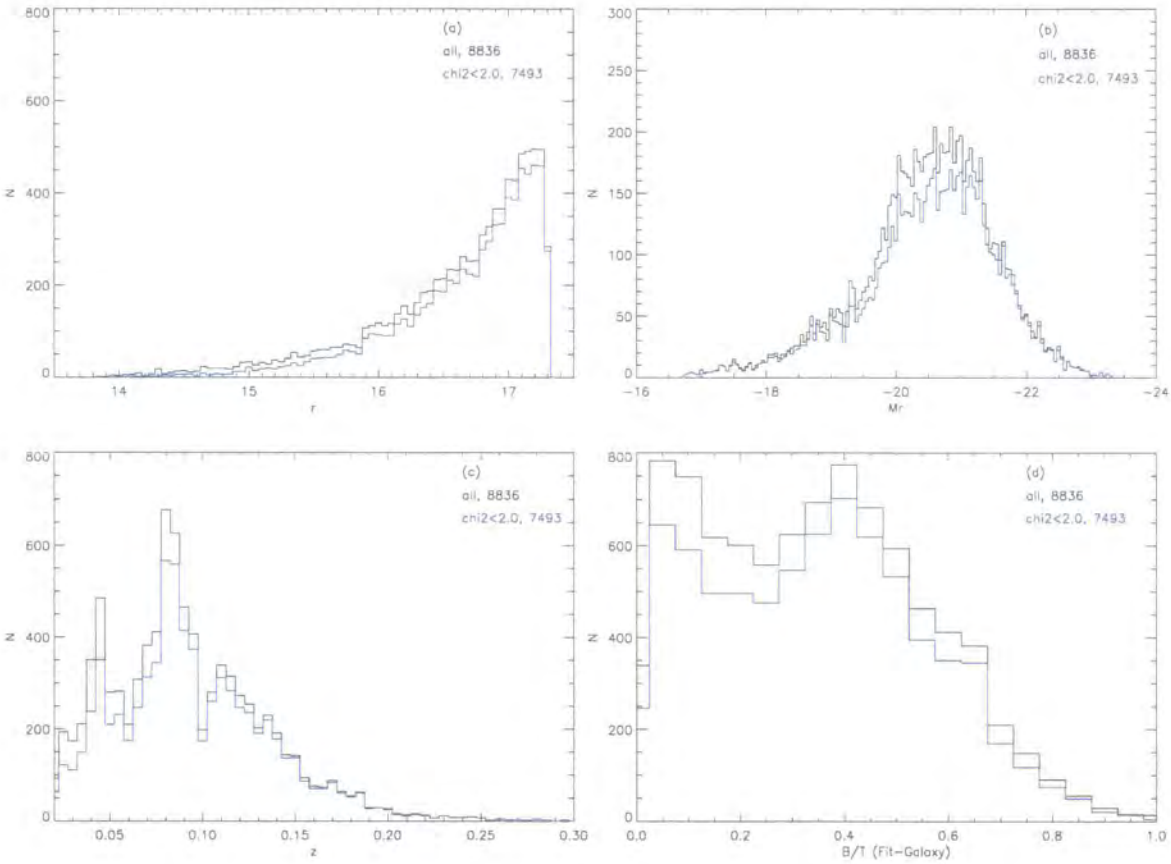

Figure 5.12: Plotted are the distributions of the (a) apparent magnitude, (b) absolute magnitude, (c) redshift and (d) recovered B/T ratios. The total sample is represented by the black histograms and the $\chi^2_\nu < 2.0$ selected sample is represented by the blue histograms. No biases due to the 'reasonable-fit' selection appear to be present.

5.3.4 B/T Error Estimates

Chapter 2 has introduced a Monte Carlo approach as the way of estimating errors on the fitted parameters in Fit-Galaxy. This method has proven to be very time consuming since the Monte Carlo error analysis on a typical galaxy could take up to several days. The full Monte Carlo analysis therefore becomes impossible for a large data-set such as the one used in this study. To obtain representative error estimates the data is divided in apparent magnitude bins of width 0.5 magnitude and, for each of these bins, 5 galaxies were taken from each of three bins in B/T (0.0 <B/T< 0.3, 0.3 <B/T< 0.6, 0.6 <B/T< 1.0). The full Monte Carlo analysis was run on the selected subsample of galaxies and the medians of the derived errors are taken to be representative for a given $[r_{mag}, B/T]$ bin.

5.3.5 Bulge-to-Disk Ratios and Galaxy Morphologies

Before the advent of high performance computing facilities the morphological properties of galaxies have been studied using either (subjective and time-consuming) visual estimates or in terms of global galaxy properties such as their colour or concentration index. Presented in this section is the study of the basic morphological properties of galaxies defined in terms of the quantitative B/T ratios of a large number of galaxies observed in the Sloan Digital Sky Survey. Since the galaxy colour and concentration index measures are also available (Stoughton et al. 2002), an estimate of the degree of correlation between the classical (eye, colour, concentration index) and more sophisticated morphological studies (quantitative B/T ratios) can be made.

Morphological Classification Using Colour

It has long been known that the galaxy colour can be used to separate elliptical (old, red) from spiral (young, blue) galaxies (de Vaucouleurs 1961) since the dominant stellar populations are reflected in the galaxy colours. Investigating the colour-magnitude and colour-colour diagrams Strateva et al. (2001) have shown that the $(u - r)$ colour distribution for the SDSS galaxies has two maxima which are separated by a well defined minimum at $(u - r) = 2.2$ and that 98% of galaxies

spectroscopically classified as 'early' types have $(u-r) > 2.2$ whilst 73% of spectroscopically classified 'late' types have $(u-r) < 2.2$. Strateva et al. (2001) have also shown that this separator holds for a subsample of visually classified morphological types where 80% of galaxies visually classified as E, S0 or Sa have colours redder than $(u-r) = 2.2$ and 66% of galaxies visually classified as Sb, Sc and Irr have colours bluer than $(u-r) = 2.2$. The $(u-r)$ separator has already been used to study morphological properties of galaxies in the SDSS sample as a function of environment (Goto et al. 2002, Balogh et al. 2004).

The derived B/T ratios can be plotted against the galaxy colours for the SDSS sample to investigate their mutual correlation. The correlation plot of the B/T ratios of the SDSS sample and the corresponding galaxy $u-r$ colours is shown in Figure 5.13 and implies that the galaxy colour and the corresponding B/T ratios are only weakly dependent. In particular the 'red' $((u-r) > 2.2)$ galaxies span a large range in B/T ratio.

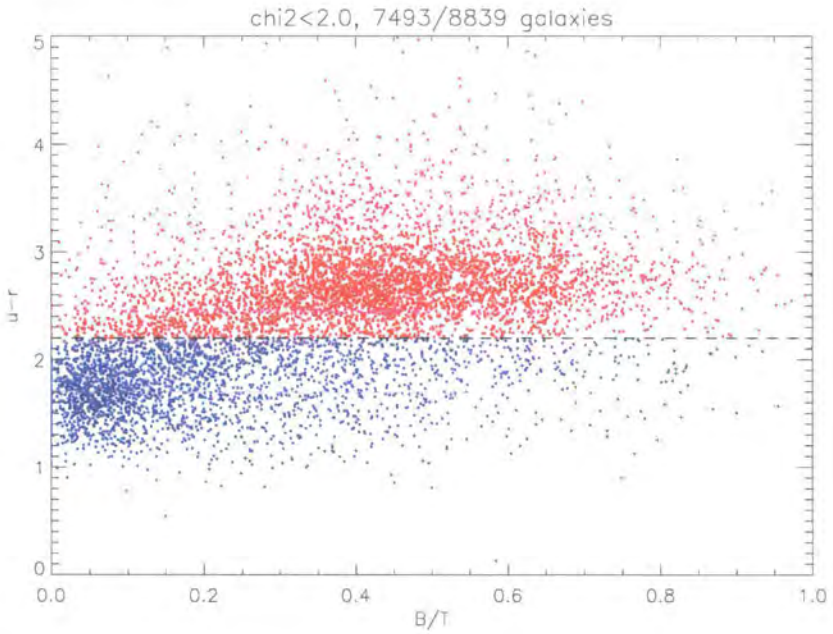

Figure 5.13: Fit-Galaxy B/T ratio vs $(u-r)$ colour for the sample of 7493 SDSS galaxies studied here. The figure does indicate that most galaxies colour classified as late types are predominately disk dominated systems and that the colour classified early type morphologies have $B/T > 0.4$.

Morphological Classification Using Concentration Index

Galaxies can also be classified depending on how 'peaky' their light distribution is by using the concentration index (Abraham et al. 1994). The surface brightness distribution of ellipticals and S0s is expected to be a lot more centrally concentrated than the corresponding surface brightness distribution of spirals and irregulars. Shimasaku et al. (2001) have defined the (inverse) concentration index for the SDSS galaxies to be the ratio of the Petrosian radii at the half-light and 90% light radii and define an optimum division between the late and early types to be at $C = 0.33$ (with $15 - 20\%$ contamination from the opposite types). This separator has also been used to investigate the morphological properties of SDSS galaxies (Goto et al. 2002, Nakamura et al. 2003).

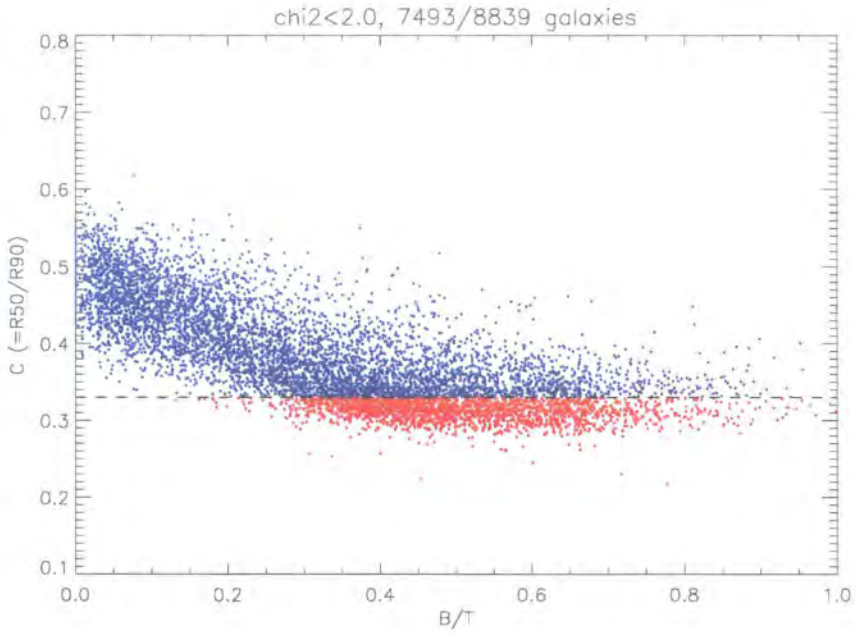

Figure 5.14: Fit-Galaxy B/T ratio vs (inverse) concentration index, $C = R_{50}/R_{90}$, for the sample of 7493 SDSS galaxies. The figure shows that more centrally concentrated galaxies ($C < 0.33$) predominately have higher B/T ratios.

The correlation between B/T ratios and the (inverse) concentration index, C, is shown in Figure 5.14. This figure demonstrates that the bulge-dominated galaxies in general tend to be more centrally concentrated whilst a larger scatter is present

for the galaxies which appear to be disk-dominated.

Morphological Classification : B/T vs Eye-Morphology

Shimasaku et al. (2001) used a sample of 456 bright SDSS galaxies ($g' < 16.0$) visually classified into seven morphological types (Hubble type E, S0, Sa, Sb, Sc, Sdm and Im) to investigate the galaxy colours, effective sizes and the concentrations. The (inverse) concentration index was found to correlate well with the visual estimates of morphology. Shimasaku et al. (2001) have kindly provided us with their visual morphologies and we have correlated them with the Fit-Galaxy B/T ratios. A total of 166 galaxies are found to overlap between the two samples and also have $\chi^2_\nu < 2.0$. Figure 5.15 illustrates a good correlation between the (inverse) concentration index and the eye-morphology for 166 galaxies and confirms the result of Shimasaku et al. (2001). Plotted in Figure 5.16 is the correlation between the derived B/T ratios and the visual morphology for these 166 galaxies. A general trend that the recovered B/T ratio increases as the earlier types are probed is clear, although the scatter in B/T is large.

5.3.6 Correlations of B/T with Other Fitted Parameters

Understanding the properties of this large statistical sample of galaxies is important since it may reveal features which otherwise would not be discovered in smaller samples such as those discussed in Section 5.3.5. Equally any correlations between the parameters could help discover and reduce possible biases introduced by the fitting routine.

The histogram plots of the SDSS galaxy properties inferred from the Fit-Galaxy decompositions are shown in Figure 5.17 and suggest the following :

1. Many galaxies appear to have bulge 1/2-light radii($r_e < 1$kpc),

2. There appears to be a large number of highly elliptical bulges,

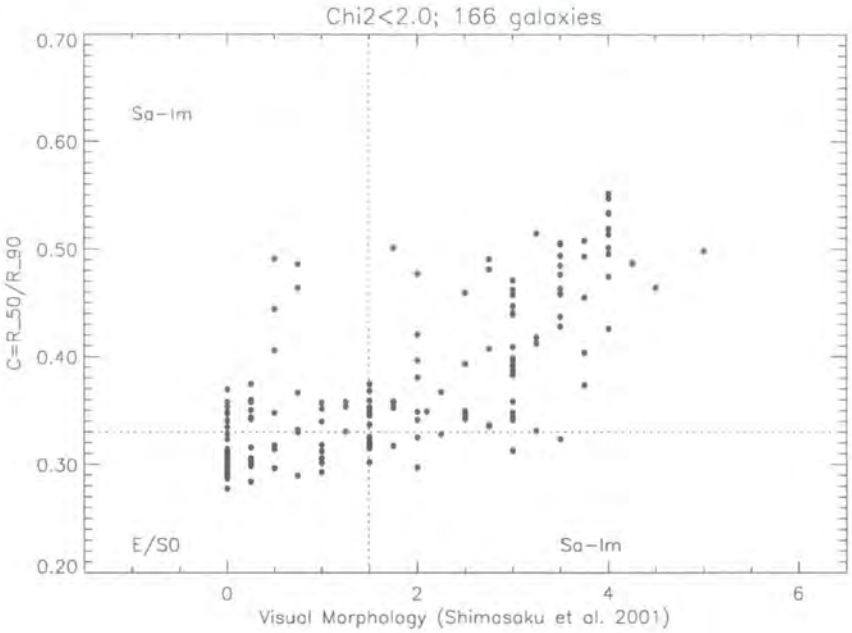

Figure 5.15: Concentration index vs eye morphology of Shimasaku et al. (2001) for the overlapping sample of 166 galaxies. Using the concentration index galaxies can crudely be divided only into early and late types (Shimasaku et al. 2001).

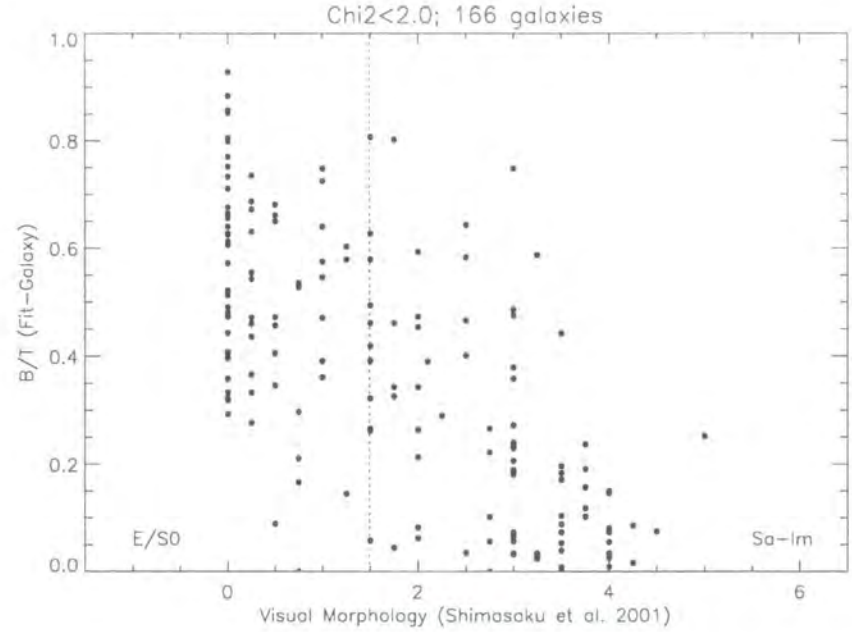

Figure 5.16: Fit-Galaxy B/T ratio vs eye morphology of Shimasaku et al. (2001) for the overlapping sample of 166 galaxies. There appears to be a general trend that the B/T increases with S-S0-E morphologies but the scatter in the B/T ratio is large.

3. An excess in the number of galaxies with PA_{bulge} equal to 0° and 180° is present, and,

4. The distribution of the disk cos(i) for a large sample of galaxies appears to be non-uniform.

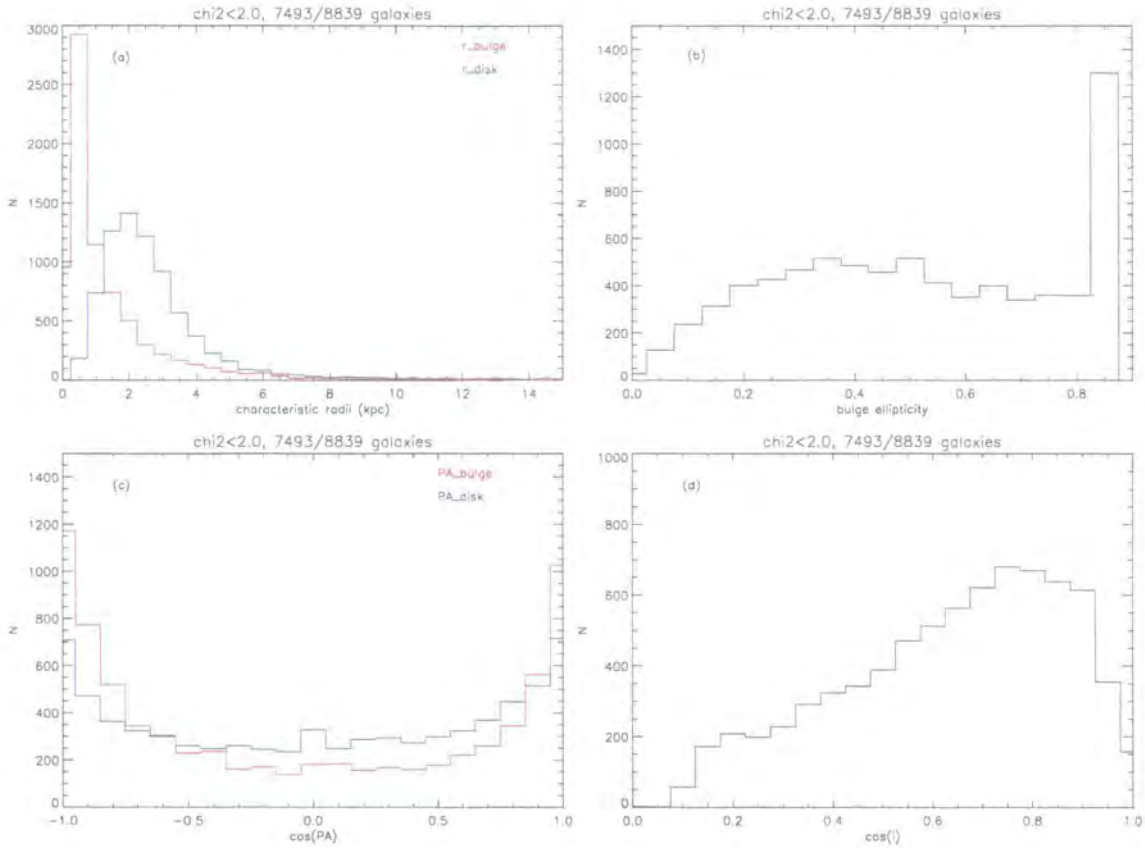

Figure 5.17: Fit-Galaxy parameter histogram plots suggest the following : (1., a) Galaxies have predominately small bulges r_e < 1kpc, (2., b) There exists a large number of highly elliptical bulges, (3., c) Preference to a $PA_{bulge} \sim 0°$ and (4., d) Non-uniformity of the disk inclination angle. All these are discussed in more detail in the text.

Since in this study we are predominantly interested in obtaining reliable measures of the galaxy B/T ratios it is important to understand the cause of the above findings and their influence on the recovered B/T. We next comment on the above findings.

Correlations 1 : B/T and Bulge Characteristic Radii

The bulge half-light radii are on average smaller than the corresponding disk scale lengths and most galaxies have $r_e < 1$kpc. The observed range of the radii is consistent with the findings of the Medium Deep Survey (Ratnatunga et al. 1999) who find that the median value of r_e is 1.5 kpc for their higher ($z \sim 0.4$) redshift sample.

Correlations 2 : B/T and Ellipticity

Around 15% of galaxies appear to have highly elliptical bulge component i.e. the ellipticity has reached the upper limit of $e = 0.83$. A large number of frames have been inspected by eye to find that these galaxies generally show bar-like structures in the direction of the detected highly elliptical bulge components. In these cases the existence of the extra component which is not part of the fitted model, drives the code to fit small and highly elliptical bulges (Figure 5.18). These galaxies are expected to be disk dominated and therefore very little bias is expected to be introduced to the overall B/T ratio.

Correlations 3 : B/T and Bulge Position Angle

Many galaxies appear to have $PA_{bulge} \sim 0°$. This could be due to either :

1. Some feature intrinsic to the code such as the initial moments estimate of the bulge PA, or,

2. Something which is intrinsic to the data.

It remains unclear if the bias PA_{bulge} affects the derived B/T. To test (1.) a galaxy with the recovered $PA_{bulge} \sim 0°$ was re-fit three times. Each time a initial (and very different) PA_{bulge} was explicitly specified and therefore the value for the PA_{bulge} obtained from the initial image moments was ignored. The code was found to very quickly converge to a minimum at $PA_{bulge} \sim 0°$ with the same B/T ratio irrespective of the very different initial PA_{bulge} which demonstrates that the initial value of the PA_{bulge} is not crucial. The point 2. could be a possible explanation

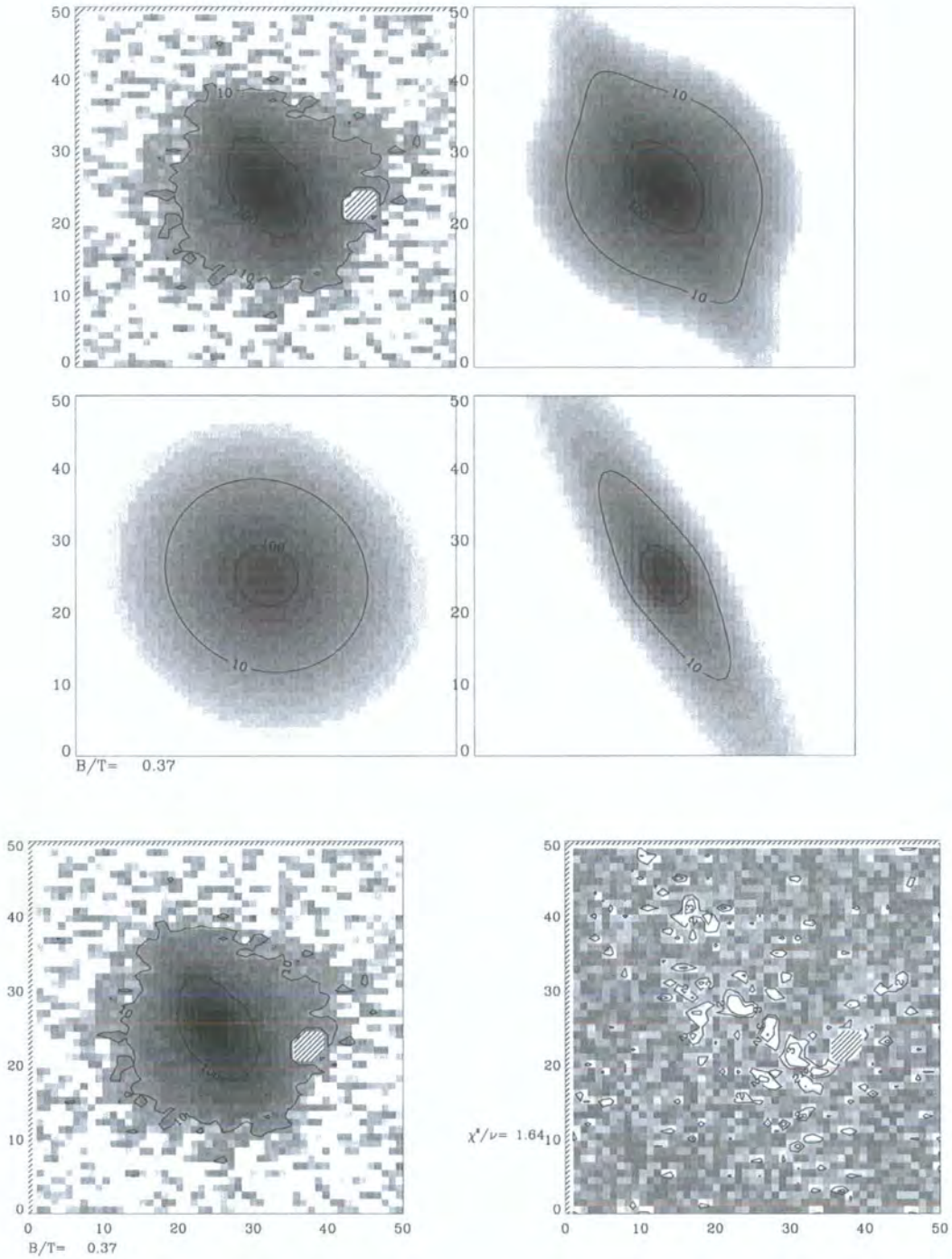

Figure 5.18: An example of a galaxy with a highly elliptical bulge. This galaxy demonstrates how the internal bar-like structure in the galaxy can lead to a detection of a highly elliptical bulge along the same direction.

since the data are observed in the drift-scan mode along the easterly direction (direction of the x-axis). However, we still need to quantify how dependent is the derived B/T upon the bulge orientation. To do this we randomly selected sample of 100 SDSS galaxies and rotate the images by +90° and re-fit. The results are shown in Figure 5.19 and imply that the recovered B/T ratios ($\sigma_{rms} = 0.09$) are not strongly affected by the orientation of the bulge position angle on the sky.

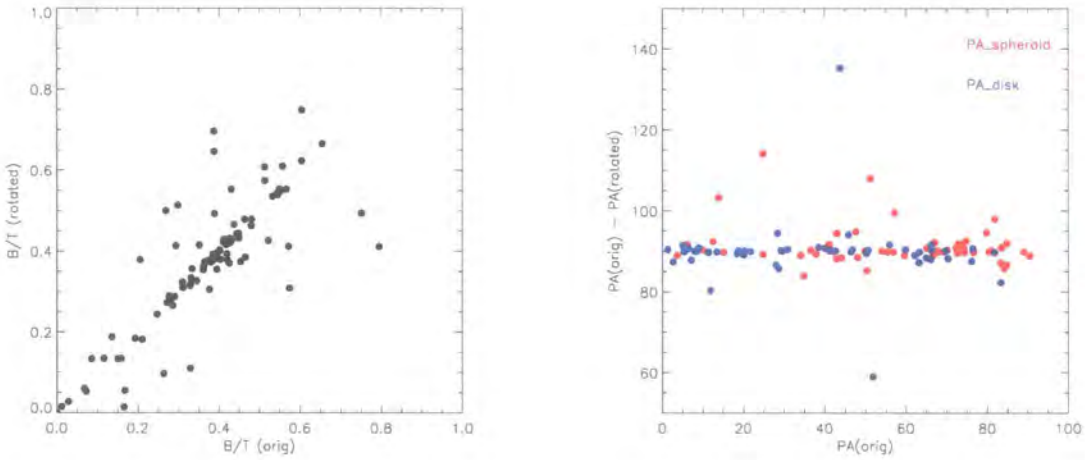

Figure 5.19: Correlation plot for a sample of 100 SDSS galaxies versus the same galaxies but rotated anticlockwise by 90°. This figure demonstrates that the recovered B/T ratios are not strongly affected by the orientation of the bulge position angle.

Correlations 4 : B/T and Disk Inclination

Correlation 4. is the most puzzling one. A large number of objects in the sky which are randomly inclined to the line of sight should have a uniform distribution of $\cos(i)$. Figure 5.17 clearly shows that this is not the case for the inclination angles of the disk components obtained by decomposing the SDSS galaxies. The influence of the $\cos(i)$ bias on the B/T ratio is therefore examined further below.

Fit-Galaxy Code Disk Inclination Tests : Model Galaxies Revisited

To test whether the (apparent) incorrect recovery of the disk inclination is a feature of the code a sample of 200 model galaxies was created internally in the Fit-Galaxy

code (Chapter 2). The galaxy B/T ratios were chosen at random between $[0, 1]$. The remaining parameters, as well as the $\cos(i)$, were also chosen at random. Figure 5.20 demonstrates that the Fit-Galaxy code recovers the $cos(i)$ distribution for 200 model galaxies well. A feature to notice though is a slight excess around $i > 75 - 80°$ which appears to be internal to the code. The code is biased away from the 90° limit as this would correspond to fitting an infinitely thin edge-on disk. This feature remains true even if the inclination limits are increased from $[0, 90]$ to $[-180, 180]$. The B/T ratios do not seem to be affected by this small limitation of the code (model galaxies created with a $i \sim 90°$ and have recovered $i \sim 85°$ do not appear to show a bias in the recovered B/T ratio).

The questions that remain to be answered are : (i) how well is the B/T ratio recovered if the disk inclination angle is recovered incorrectly and (ii) what else could be responsible for the $\cos(i)$ bias ? To test (i) several model galaxies with B/T= 0.5 and $i \sim 20$ and $i \sim 70$ degrees were created. The code was explicitly set to search between the other 'extreme' inclination values (i.e. range $[55, 90]$ for $i = 20°$ and range $[0, 45]$ for $i = 70°$). Figure 5.21 demonstrates that the recovered B/T ratios are strongly dependent upon recovering the correct inclination angle of the disk.

One possibility that could be causing more face-on disks (but only for the brightest of the objects) to be detected could be that some galaxies have a diminant thick disk component and that the intrinsic thickness is compensated for by fitting a more face-on flat disk. However, it remains unclear how to correct for the $\cos(i)$ non-uniformity in terms of the B/T ratio.

5.3.7 Bias Influences on Luminosity Function

Too many elliptical bulges : amount of light put into the bulge is larger than the true value as additional components, such as light from bright spiral arms, is added in. Bulge LF will be overestimated (especially at the faint end). Dephicit of round bulges should not in itself directly affect the LF but will do indirectly because of the previous remark. There appears to be no correlation between bulge ellipticity and

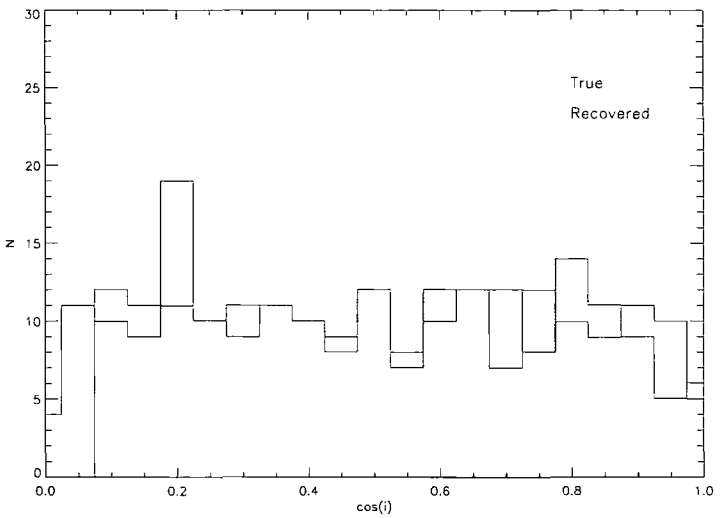

Figure 5.20: The input and the recovered cos(i) distribution for 200 model galaxies created and decomposed using the Fit-Galaxy code. The figure demonstrates that the non-uniformity in the cos(i) is not caused by the fitting code. A slight excess of galaxies with $i \sim 75 - 80°$ is caused by the code not liking to hit the upper limit of $i = 90°$ since this would correspond to fitting an infinitely thin disk. This however does not bias the recovered B/T ratio.

both bulge and disk position angles. A plot of cos(i) vs e_b shows dephicit of inclined disks and a large number of face-on disks. This would lead to overestimate of the disk light and underestimate of the bulge light as it will try to fit large numbers of fake face-on disks which may not necessarily be present.

5.3.8 Inclination : SDSS, WFC and MORPHS Comparison

In Chapter 2 it was demonstrated that the Fit-Galaxy and Gim2D decomposition codes agree well on the recovered parameters (including inclination) for both the model galaxies and the real SDSS data. This point is crucial since it demonstrates once more that the Fit-Galaxy code cannot be responsible for the cos(i) bias. This would imply that there might be something in the SDSS data that could be causing the bias and is supported by the fact that the two cos(i) distributions for the WFC cluster sample (Chapter 3) and MORPHS cluster sample (Chapter 4) shown in Figure 5.22 appear to be a lot more uniform.

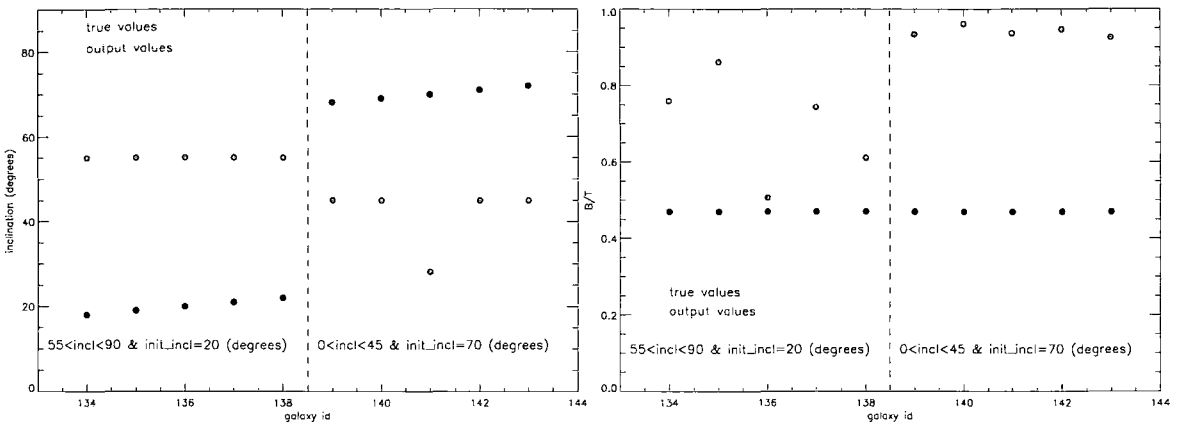

Figure 5.21: A test of the B/T ratio recovery when the disk inclination is incorrectly determined. A set of model galaxies with $B/T = 0.5$ and $i \sim 20°$ and $i \sim 70°$ is created. The code was specifically told to search between the opposite inclination extrema i.e. ranges $[55, 90]$ and $[0, 45]$ respectively. This showed the recovered B/T to be strongly dependent upon the inclination angle.

There now remain two possible explanations : (a) the difference in the data and (b) the difference in the environment. The point (a) is discussed first. Abell 0168 is a cluster which lies in the area of overlap between the SDSS data and the WFC observations. For the galaxies that are found in both samples we plot the inclinations and the B/T ratios obtained using the two independent decomposition codes. As seen in Figure 5.23 the g-band WFC Gim2D outputs agree with the r-band SDSS Fit-Galaxy outputs although this is difficult to quantify since the overlap sample contains only $\sim$ 30 galaxies. However, this is suggestive that the problem is not related to the way the actual observations were taken. The point (b) is potentially suggestive of some extra fitting component which may be associated with the field galaxies only as is discussed in the next section.

5.3.9 Investigating Inclination Dependence on Local Galaxy Environment

The motivation for investigating the possible $\cos(i)$ dependence on the local galaxy environment comes from the comparison of the cluster samples in Figure 5.22 with

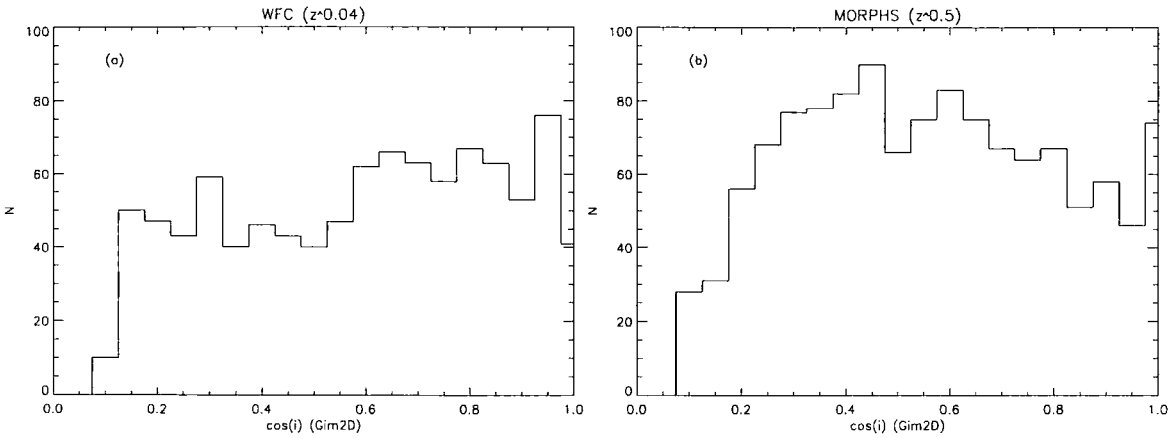

Figure 5.22: The distribution of the recovered cos(i) for a $\sim$ 800 WFC (left) and $\sim$ 1000 MORPHS (right) cluster galaxies decomposed using Gim2D. This cos(i) distribution appears to be more uniform than the corresponding one for the SDSS field galaxies obtained using the Fit-Galaxy code. The decomposition routines are not responsible for the difference in cos(i) observed between the samples.

the SDSS field galaxy sample in Figure 5.17 (d) in which the cluster galaxies appear to have a much flatter cos(i) distribution than the field galaxies. Various tests have ensured that differences in the way the data were taken or in the fitting routines are not responsible for the differences observed. We therefore use the local galaxy density estimator of Balogh et al. (2004) to divide the SDSS sample in terms of the local galaxy environment. The local galaxy density estimator of Balogh et al. (2004) is based upon the nearest neighbour approach i.e. the estimator calculates the projected distance D to 5^{th} nearest neighbour and within $\pm$1000kms^{-1} and down to $M_r = -20.0$ (reddening and K+E corrected) and is reliable between $0.03 < z < 0.08$ (Balogh et al. 2004). The projected surface density is simply given by $\Sigma_5 = 5/\pi D^2$ Mpc^{-2}. A cross-correlation with the Balogh et al. (2004) SDSS DR1 density catalogue allows the densities for $\sim$ 2500 galaxies in our sample to be inferred (we lose most of the other galaxies due to the imposed redshift range). The distribution of the local galaxy densities for $\sim$ 2500 galaxies is shown in Figure 5.24.

Based upon the distribution of densities shown in Figure 5.24 (a) we take 5 galaxies Mpc^{-2} to be a divider between a region of 'low' ($\Sigma_5 < 5$ Mpc^{-2}) and a

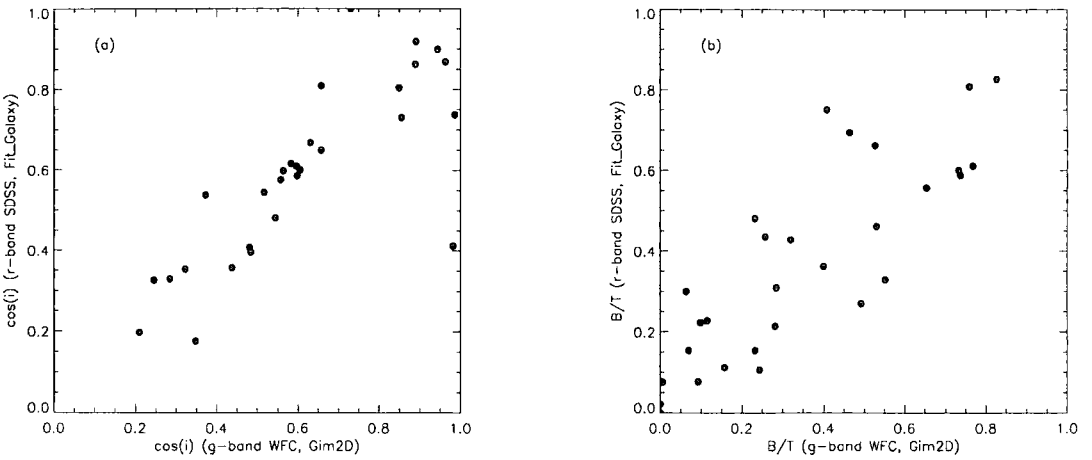

Figure 5.23: The correlation plots for $\sim$ 30 galaxies that overlap between WFC and SDSS samples. The parameters appear to correlate well but the small sample size makes this difficult to quantify. (a) cos(i), (b) B/T ratio. The plots are suggestive that the data itself is not the cause of the bias in the cos(i).

region of 'high' ($\Sigma_5 > 5$ Mpc^{-2}) galaxy density. The cos(i) distributions are plotted in Figure 5.24 (b). The Kolmogorov-Smirnov test gives a very low probability (0.57) that the cos(i) distributions are in agreement. The possible cause of the disagreement is the local galaxy density since this is the main difference between the two samples. Therefore the local galaxy density may play a role in the bias detected in the distribution of the cos(i) of the galaxy disks. Why this should be so remains unclear but could indicate the presence of an additional structural component in galaxies in low density environments which is not present in galaxies in high density regions.

5.3.10 Fit-Galaxy Decompositions : Summary

The main points of this Chapter discussed so far are summarised below :

- The Fit-Galaxy code has been used to derive the structural parameters for a large ($\sim$ 9000) field sample of galaxies taken from the Sloan Digital Sky Survey (SDSS).

- The Fit-Galaxy code can accurately determine B/T ratios for SDSS galaxies

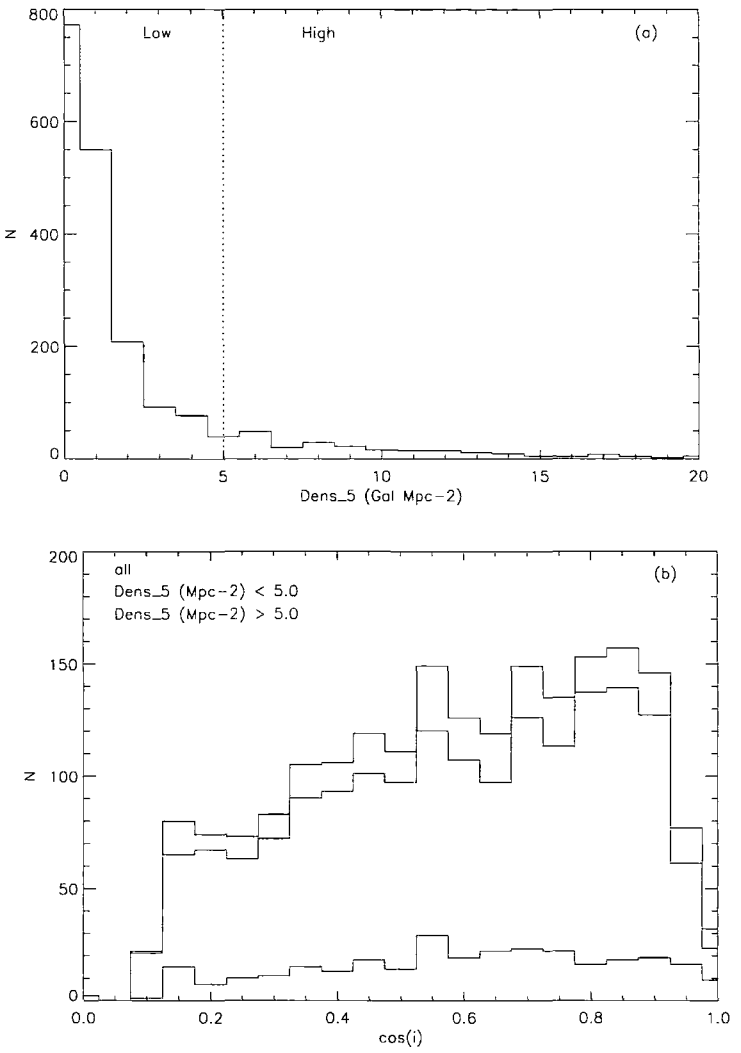

Figure 5.24: The density distribution for a sample of $\sim$ 2500 SDSS EDR galaxies with $0.03 < z < 0.08$. The density is the projected density to the 5^{th} nearest neighbour and down to $M_r = -20.0$. The density of 5 galaxies Mpc^{-2} is used to separate galaxies into those that belong to low ($\Sigma_5 < 5$ Mpc^{-2}, 297 galaxies) and high ($\Sigma_5 > 5$ Mpc^{-2}, 1721 galaxies) density regions. The Kolmogorov-Smirnov test gives a very low probability (0.57) that the cos(i) distributions are in agreement. The possible cause of the disagreement is the local density since this is the main difference between the two samples. Therefore, the local galaxy density may play a role in the bias detected in the distribution of the cos(i) of the galaxy disks.

brighter than $r = 17.3$ magnitude.

- The real SDSS PSF is reasonably well represented by the analytic Moffat PSF assumed by the Fit-Galaxy code.

- Galaxies with postage-stamps greater than 91 pixels on a side are binned 2×2 and model tests showed that the recovery of the input B/T ratio after binning shows no additional biases (c.f. Chapter 2).

- The goodness-of-fit selection was set to be $\chi^2_\nu < 2.0$. The selection showed no biases to be introduced to the sample.

- Fit-Galaxy decomposition outputs revealed the output B/T distribution to lack bulge dominated systems (i.e. $B/T > 0.7$).

- A large number of highly elliptical bulges is found possibly due to the presence of strong bars. Because these are preferentially disk-dominated systems this should not affect the B/T ratios and therefore the luminosity function estimates presented in the next section.

- A preference for the bulge to be oriented at $PA_{bulge} \sim 0/180°$. Tests showed no bias in the B/T recovery for this effect.

- The distribution of $\cos(i)$ for the disk component is non-uniform, as would have been expected for disks randomly oriented with respect to the line of sight. Tests implied that the B/T recovery is very dependent upon the disk inclination.

- A comparison between Gim2D and Fit-Galaxy fits implies that any bias in $\cos(i)$ is not due to the Fit-Galaxy code.

- A comparison of ~ 30 galaxies with both WFC and SDSS data shows that the WFC data has a much better uniformity in $\cos(i)$ suggesting that the cause is some intrinsic property embedded in the SDSS data.

- A $\cos(i)$ dependence on the galaxy environment is investigated where the galaxy environment is defined as the projected surface density to the 5^{th} near-

est neighbour. There is some indication that the $\cos(i)$ might be related to the galaxy environment.

- Although the issue of the non-uniform $\cos(i)$ distribution remains unresolved, we can use the derived structural parameters to investigate the luminosity functions of bulges and disks in the following section.

5.4 SDSS : Luminosity Functions and Luminosity Densities

5.4.1 Introduction

The statistical properties of galaxies are commonly expressed in terms of a Luminosity Function (LF). The LF is defined as :

$$dn(M) = \phi(M)dM \tag{5.1}$$

where dn is the number density of galaxies with luminosities in the range $M, M + dM$. The simplest way to calculate the luminosity function is to estimate the number of galaxies in each individual absolute magnitude bin and divide it by the volume of space that has been surveyed (Efstathiou 1988). Galaxies in any given absolute magnitude range are assumed to be uniformly distributed in the surveyed volume which is not the case if any local over-densities are present. A variety of techniques have been developed to overcome this problem and here we will briefly and qualitatively explain the basis of each of the methods[‡].

The V_{max} method calculates the total (or maximum) volume of space, V_{max}, in which a galaxy with a magnitude m can be seen in a survey of magnitude limit m_{lim} and the luminosity function is readily obtained by summing up the $1/V_{max}$ contributions (Felten 1977). The maximum likelihood methods, STY of Sandage, Tammann & Yahil (1979) and Stepwise Maximum Likelihood Method (SWML) of

[‡]For detailed mathematical explanations of each of the methods the reader is referred to Appendix C.

Efstathiou, Ellis & Peterson (1988), are based on the measure of the probability that a galaxy with a redshift z and an absolute magnitude M is seen in a magnitude-limited survey. The STY method assumes a parametric form for the luminosity function $\phi(M)$ usually taken to be a Schechter function (Schechter 1976) :

$$\phi(M)dM = 0.4 \ln 10 \phi^* 10^{-0.4(M-M^*)(\alpha+1)} exp[-10^{-0.4(M-M^*)}] \quad (5.2)$$

where M^* is a given characteristic magnitude, α is the faint-end slope and ϕ^* is the normalization. Integrating over the Schechter function provides estimates of the basic statistical properties of galaxies such at their luminosity density. The SWML method characterises the LF as a series of steps based on the absolute magnitude weighting and requires no assumption of the parametric form of the LF. The galaxy luminosity density can also be obtained by summing up all the individual SWML contributions.

Computing the bulge and disk LFs is a little more tricky since there is an additional constraint to be considered (Benson et al. 2002) namely the detectability of a bulge/disk depends both on the galaxy apparent magnitude and the corresponding B/T. This needs to be accounted for when constructing the luminosity function. The detailed mathematical explanation of each of the methods is presented in Appendix C. The functional form that is assumed for the STY parametric fits to the bulge and disk LFs is of a Schechter×Exponential form and is motivated by the tail down in the LF estimate at the faint-end (Benson et al. 2002).

5.4.2 SDSS Absolute Magnitudes and K+E Corrections

In order to study the luminosity functions of galaxies we need to obtain the galaxy absolute magnitudes. A galaxy at redshift z with the apparent magnitude m has an absolute magnitude M given by :

$$m - M = 25 + 5log_{10}(D_L) + KE(z) \quad (5.3)$$

where D_L is the luminosity distance in Mpc and $KE(z)$ is the K+E correction. The K-correction is necessary because the broad-band measurements of the flux for galaxies at different redshifts span different regions of the rest-frame galaxy spectrum. The E-correction takes into account that a galaxy evolves with time depending on the galaxy spectral type. Together they are referred to as the K+E correction.

The absolute magnitudes and K+E corrections for each of our catalogued galaxies were obtained using a code kindly provided by Dr Carlton Baugh. The code employs the revised isochrone stellar population synthesis models of Bruzual & Charlot (1993) to determine the present-day galaxy luminosities. The models assume some distribution of masses of stars at the time of birth which are subsequently evolved according to a set of theoretical tracks and the new stars are formed according a defined star-formation rate [$\psi(t) \propto exp^{-t/\tau}$ with τ representing the various star formation timescales]. For a variety of different stellar initial mass functions (IMFs) a grid of models was set each with a varying metallicity (some fraction of Z_{sun}) and a varying τ. The dust extinction is applied to the models and a Salpeter (1955) IMF assumed. A table of absolute magnitudes, galaxy colours, K+E corrections and galaxy mass-to-light ratio is produced for every point on the grid. For a given galaxy redshift a model track is found that best matches the observed $g-r$ and $r-i$ galaxy colours. The selected model track is used to infer the galaxy present-day ($z = 0$) r-band absolute luminosity, the K+E correction and the stellar mass-to-light ratio. The mass-to-light ratio is used to convert the amount of light detected in a given galaxy to the corresponding mass (in units of solar mass) and is useful in determining how much baryonic mass resides in every galaxy and its components. Note that the K+E corrections are based on the total (i.e. bulge plus disk) colour of a galaxy.

5.4.3 SDSS Luminosity Function Estimates

The luminosity function code developed by Benson et al. (2002) will be used to obtain the total, bulge and disk luminosity functions for the current sample of SDSS EDR galaxies. To place the SDSS luminosity function onto a common system of normalisation the number of galaxies per given apparent magnitude bin per square degree needs to be calculated. This number is usually normalised to match the number counts of other published surveys.

5.4.4 Sample Solid Angle

To calculate the area or the solid angle (SA) for the above catalogued sample the RA and Dec coordinates are pixelised in 0.2° bins. All the areas which contain at least one galaxy residing in a particular (RA, Dec) bin were added up to give the total solid angle. To test the dependence upon the choice of the bin size various bin widths were chosen until a particular bin width was reached for which changing it a little did not produce large changes in the recovered SA. As an additional check this bin size was used to reproduce the SA of the whole of the SDSS EDR. For the bin size of 0.2° the solid angle in this study is SA=165.5 square degree.

5.4.5 Luminosity Function Code : Mock Galaxy Catalogue

The performance of the LF code is tested using a mock galaxy catalogue of known input parameters. The mock catalogue was created by random sampling a Schechter LF. The SDSS r-band Schechter function parameters from Nakamura et al. (2003) were assumed : $M^* = -20.62$ and $\alpha = -1.17$. A galaxy i is then chosen with a random M_i and a random ϕ_i. If $\phi(M_i) < \phi_i$ the apparent magnitude of a galaxy i is calculated by placing a galaxy at random in the survey's volume (as determined by the survey's redshift range, $0.02 < z < 0.3$). Only if the inferred apparent magnitude meets the apparent magnitude cut of the catalogue will this galaxy's entry be accepted and a random B/T ratio assigned to it.

For a random-mock catalogue which contains 8839 galaxies and whose B/T ratios were also chosen at random, the input Schechter parameters are recovered with a very high accuracy and the different LF estimators agree very well (Figure 5.25). The χ^2-minimization technique uses a pure Schechter function fits to the SWML data-points using a M^*, α and ϕ^* grid. Comparing the outputs obtained using the χ^2-minimization technique to the outputs obtained using the STY method provides a good test of how well the χ^2-minimization technique works. The importance of the χ^2-minimization will be emphasised in the subsequent section. The main point of the mock-catalogue tests is that the assumed parametric form for the bulge and disk luminosity functions appears to fit the mock data very well.

5.4.6 Luminosity Functions : Real Data

For the real well-fit data it is found that the STY method can recover the total luminosity parameters with a high degree of accuracy and that the STY fit traces the corresponding total luminosity SWML points well. The LF parameters obtained from the STY fit to the total luminosity also agree very well with those of Nakamura et al. (2003) (SDSS r-band, $z = 0$). However, the STY fit to the bulge and disk components does not seem to agree with the corresponding SWML estimates (SWML and V_{max} estimates agree reasonably well) as demonstrated in Figure 5.26 (disk). This is possibly an indication that the assumed functional form for the individual galaxy components (Schechter×Exponential, Appendix C) does not describe the real data. We therefore use the SWML data-points to calculate the luminosity densities by integrating over the SWML points. The luminosity densities for bulges and disks are calculated to be $\rho_L/\mathrm{h} = 0.62 \pm 0.08 \mathrm{L}_\odot$ Mpc^{-3} and $\rho_L/\mathrm{h} = 1.84 \pm 0.27 \mathrm{L}_\odot$ Mpc^{-3} respectively. This is contradictory to the findings of the previous study of Benson et al. (2002) who found the bulge and disk LFs to be very nearly equal. In the following section we investigate various systematic effects which may be biasing the above result.

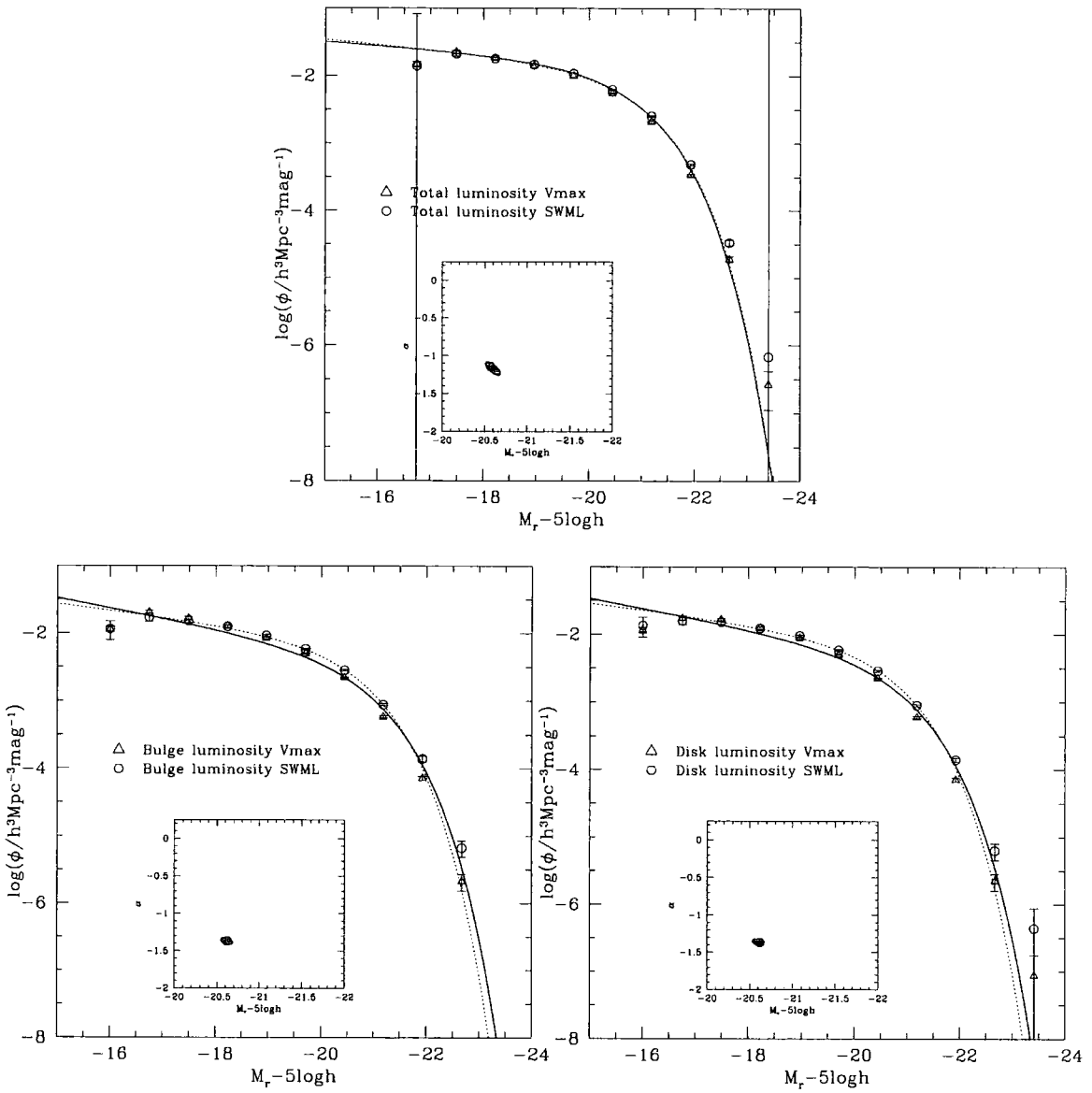

Figure 5.25: Luminosity function fits to the mock galaxy catalogue ($M^* = -20.62$, $\alpha = -1.17$ and SA=165.5 square degree). B/T is drawn at random in this catalogue. The data points are V_{max} and SWML estimates of the luminosity function. The solid lines represent the STY method fits, while the dotted lines represent the fits to the SWML points using the χ^2-minimization technique with best-fit parameters. Total LF : $\chi^2_\nu = 0.75$, $M^* = -20.65$ and $\alpha = -1.17$. Bulge LF : $\chi^2_\nu = 1.62$, $M^* = -20.40$ and $\alpha = -1.24$. Disk LF : $\chi^2_\nu = 0.99$, $M^* = -20.41$ and $\alpha = -1.25$. Upper figure is for the total galaxy luminosity; lower figures are for bulge and disk components respectively.

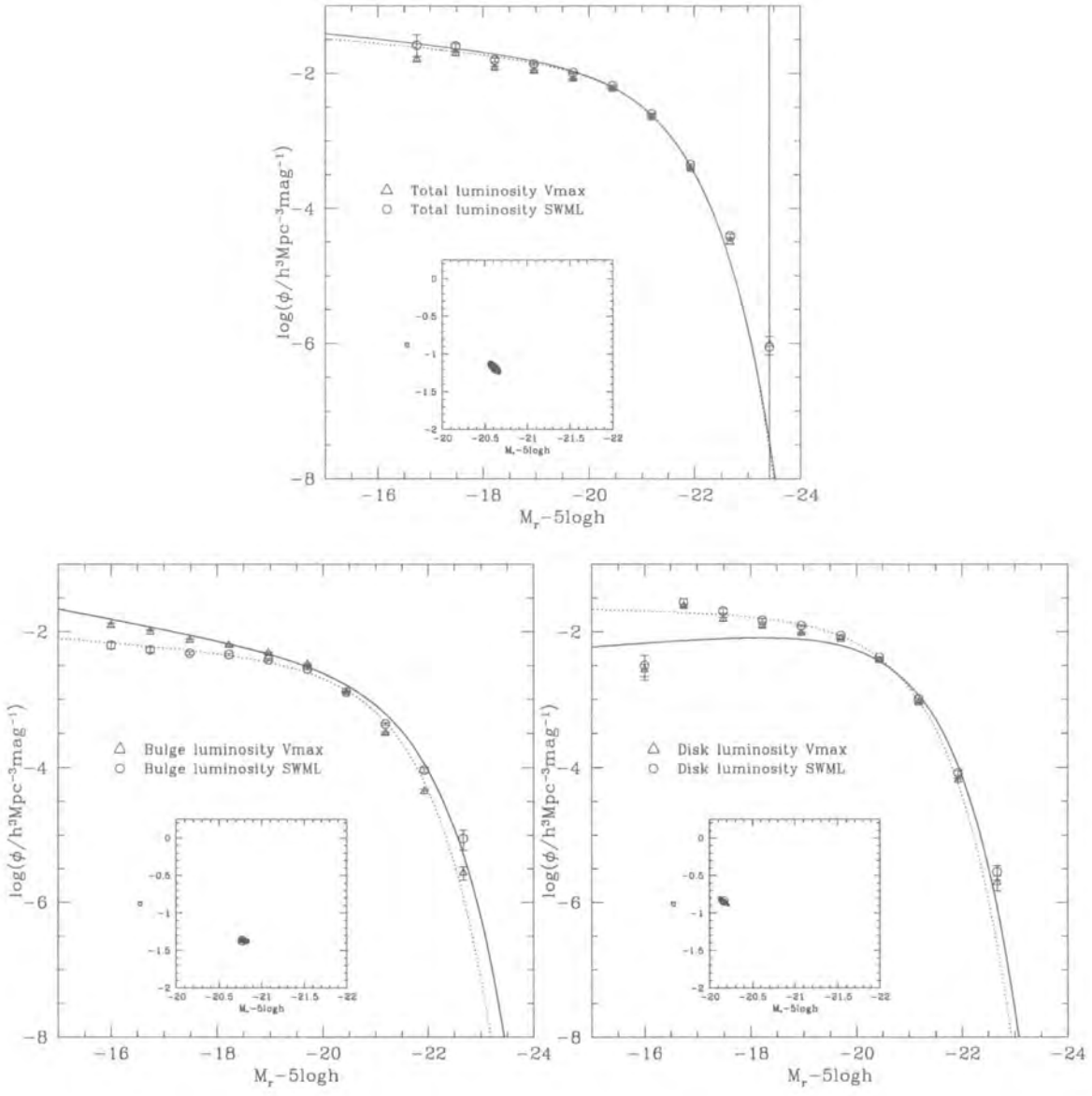

Figure 5.26: Luminosity function fits to the real galaxy catalogue with solid angle of 165.5 square degree and 7493 galaxies with $\chi^2_\nu < 2.0$. The data points are V_{max} and SWML estimates of the luminosity function. The solid lines represent the STY method fits, while the dotted lines represent the fits to the SWML points using the χ^2-minimization technique. Upper figure is for the total galaxy luminosity; lower figures are for bulge and disk components respectively.

5.4.7 Luminosity Function Dependence on Lack of Pure Bulges

In Chapter 2 it was demonstrated that there is a small bias in the way the Fit-Galaxy code recovers B/T ratios and that the recovered B/T ratio can typically be underestimated $\sim$ 20% for the bulge-dominated systems. To quantify how much this bias affects the luminosity function estimates the recovered B/T distribution is made artificially flat for all galaxies with B/T> 0.7. The population of galaxies in the B/T= 0.7 bin is distributed across all B/T> 0.7 bins so that this distribution is now flat as shown in Figure 5.27. This would correspond to the most extreme change in the B/T distribution and will allow any biases in the recovered bulge and disk luminosity functions to be quantified. The LF fits are shown in Figure 5.28 and the luminosity density does not appear to change much from the original values : ρ_L/h= $0.63 \pm 0.08 L_\odot$ Mpc^{-3} and ρ_L/h=$1.82 \pm 0.27 L_\odot$ Mpc^{-3}.

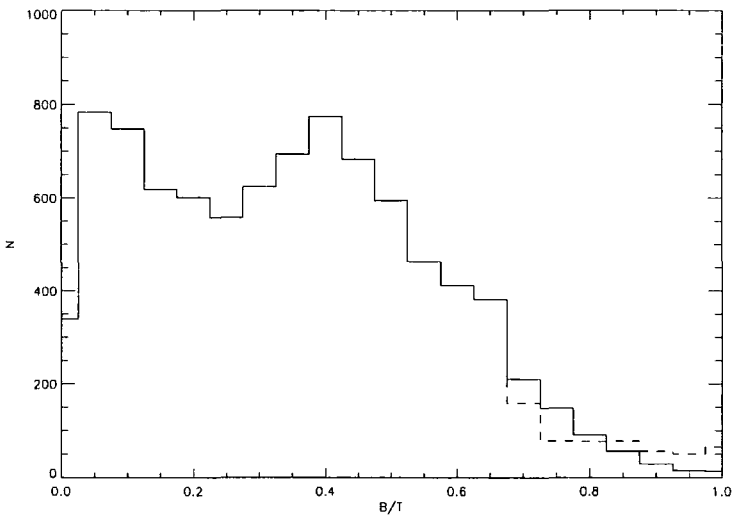

Figure 5.27: The dashed line shows the distribution of artificially flattened B/T ratios while the solid line is the original recovered B/T distribution. The flattened distribution is used to infer the luminosity function parameters. This allows to test how the lack of pure bulges introduced by the Fit-Galaxy code affects the luminosity function outputs.

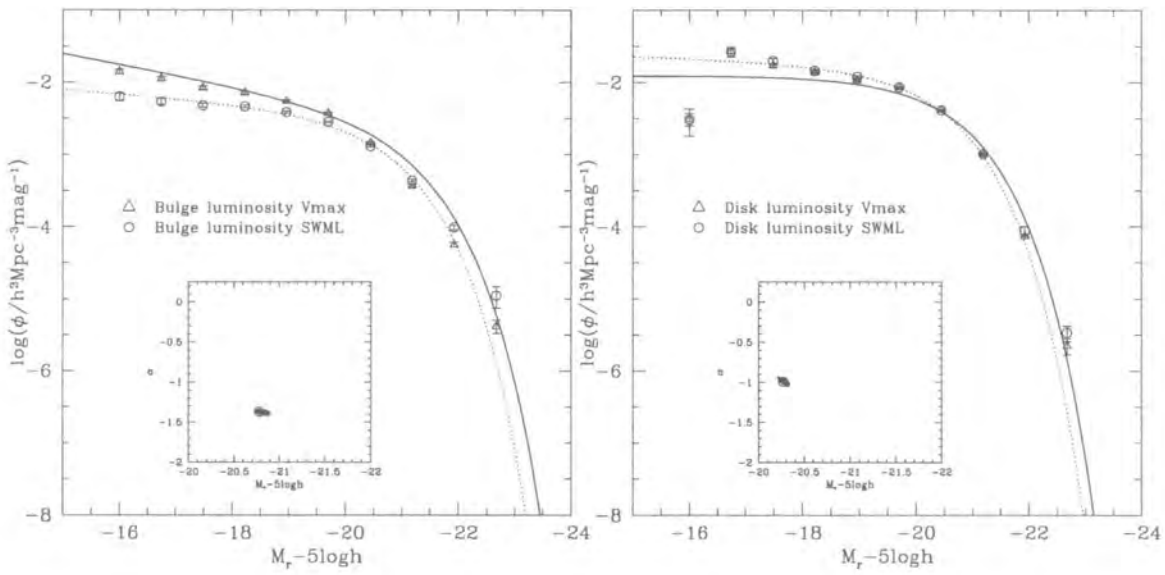

Figure 5.28: Luminosity function fits to the real galaxy catalogue with solid angle of 165.5 square degree and 7493 galaxies with $\chi^2_\nu < 2.0$ and flattened B/T> 0.7 distribution. The data points are V_{max} and SWML estimates of the luminosity function. The solid lines represent the STY method fits, while the dotted lines represent the fits to the SWML points using the χ^2-minimization technique.

5.4.8 Luminosity Function Dependence on Inclination

In this section we make an attempt to understand the way the $\cos(i)$ bias identified in Section 5.3.6 might be corrected for. We randomly sample the full galaxy catalogue and throw away galaxies which have $0.5 < \cos(i) < 0.9$ until a flatter $\cos(i)$ distribution is achieved (Figure 5.29). Whilst this is not a rigorous procedure since there is no way to assume that the galaxies being rejected are the ones with biased $\cos(i)$ estimates, it does allow an initial estimate of the sensitivity of the global properties of the sample (e.g. luminosity densitites) to this problem.

The LF estimates are presented in Figure 5.30 and show a significant difference from the fits that were obtained on the full galaxy sample.

5.4.9 Luminosity Functions : Summary

A summary of the recovered parameters for mock and real galaxy distributions using SWML, STY and χ^2 techniques is given in Table ??. The fits to the total LF agree very well between the various methods. However the functional form assumed by the STY method (Schechter×Exponential) for the bulge and disk LFs does not seem to be appropriate. The χ^2-minimization technique gives better fits to the STWM data-points simply assuming the LF of a Schechter form. The main results from the mock galaxy catalogues seem to indicate that the code does well in recovering the input mock LF parameters if the B/T ratios are drawn from a random distribution. The fits to the real data partially indicate that there might be a functional form is a better representation of the LFs of the individual galaxy components than the one assumed. It is reassuring that the potential bias to low B/T ratios in the code itself does not produce a significant difference in the output LF parameters after the distribution of B/T ratios for B/T$>$ 0.7 is artificially flattened. However, the results do indicate a significant change/bias introduced to the LF if the artificial flattening of the $\cos(i)$ distribution is attempted. It still remains unclear how and what is the best way of correcting for this bias. One possible way would be to only study the LFs of galaxies which appear not to have highly inclined disks but will not be attempted for this Thesis. The final estimate of the integrated

luminosity density is obtained by integrating over the SWML data-points and the large error bars indicate that this quantity has been obtained to $\sim 25\%$ level.

Table 5.2: Recovery of the Schechter parameters. The integrated SWML luminosity density is in solar units ($M_{\rm r}^{\odot} = 4.62$).

Total	N_{gal}	M^*	α (STY)	ρ_L/h $L_\odot$ Mpc^{-3} $\times 10^8$
Real	7493	-20.62	-1.17	2.72 ± 0.46
Real (B/T flat)	7493	-20.65	-1.12	2.72 ± 0.46
Real (cos(i) sel)	4769	-20.62	-1.72	3.48 ± 1.03
Total	N_{gal}	M^*	α (SWML)	ρ_L/h $L_\odot$ Mpc^{-3} $\times 10^8$
Real	7493	-20.65	-1.16	2.16
Real (B/T flat)	7493	-20.65	-1.16	2.16
Real (cos(i) sel)	4769	-20.67	-1.49	2.72
Total	N_{gal}	M^*	α (Vmax)	ρ_L/h $L_\odot$ Mpc^{-3} $\times 10^8$
Real	7493	-20.48	-0.95	1.71
Real (B/T flat)	7493	-20.49	-0.95	1.92
Real (cos(i) sel)	4769	-20.63	-1.16	1.13

5.5 Summary and Conclusions

In this Chapter we have used a sample of $\sim$ 9000 galaxies taken from the Sloan Digital Sky Survey to obtain the bulge and disk luminosity ratios using the Fit-Galaxy code of Benson et al. (2002). The 2D surface brightness fits have revealed a bias in the recovery of the disk inclination angle. Extensive tests have shown that the bias is not code-related nor does it appear to be associated with the SDSS data. Interestingly the decompositions of cluster galaxies in Chapters 3 and 4 have revealed a much more uniform cos(i) distribution somewhat suggestive of an extra

Table 5.3: Recovery of the Schechter parameters. The integrated SWML luminosity density is in solar units ($M_r^{\odot} = 4.62$).

Bulge	N_{gal}	M^*	α (STY)	ρ_L/h $L_{\odot}$ $Mpc^{-3} \times 10^8$
Real	7493	-20.77	-1.34	0.62 ± 0.08
Real (B/T flat)	7493	-20.77	-1.37	0.63 ± 0.08
Real (cos(i) sel)	4769	-20.77	-1.42	0.67 ± 1.03
Bulge	N_{gal}	$M6*$	α (SWML)	ρ_L/h $L_{\odot}$ $Mpc^{-3} \times 10^8$
Real	7493	-20.45	-1.16	0.48
Real (B/T flat)	7493	-20.46	-1.16	0.48
Real (cos(i) sel)	4769	-20.60	-1.40	0.55
Bulge	N_{gal}	M^*	α (Vmax)	ρ_L/h $L_{\odot}$ $Mpc^{-3} \times 10^8$
Real	7493	-20.24	-1.25	0.54
Real (B/T flat)	7493	-20.22	-1.23	0.62
Real (cos(i) sel)	4769	-20.23	-1.28	0.33

component that may be present in the field galaxies that is not accounted for in the 2D-decompositions. This is supported by a study of $\sim$ 2500 SDSS galaxies split into low and high density samples using the local density estimator of Balogh et al. (2004). However, the relatively small number of galaxies that belong to the highest density regimes means that further work is required to confirm this hypothesis.

This study has found that the total luminosity densities in bulges and disks are ρ_L/h= 0.62 ± 0.08 and ρ_L/h= 1.84 ± 0.27 respectively i.e. the contribution of the disks to the total luminosity density appears to be 3× greater than that of the bulges. This is contrary to the findings of the previous studies (Schechter & Dressler 1987, Benson et al. 2002) who find the bulge and disk luminositiess to be very nearly equal. We investigate the potential biases that could be causing this effect in particular a bias associated with the poor recovery of B/T for galaxies that

Table 5.4: Recovery of the disk LF Schechter parameters. The integrated SWML luminosity density isin solar units ($M_r^{\odot} = 4.62$).

Disk	N_{gal}	M^*	α (STY)	ρ_L/h $L_{\odot}$ $Mpc^{-3} \times 10^8$
Real	7493	-20.17	-0.84	1.84 ± 0.27
Real (B/T flat)	7493	-20.27	-0.99	1.81 ± 0.27
Real (cos(i) sel)	4769	-20.17	-0.94	2.49 ± 0.92
Disk	N_{gal}	M^*	α (SWML)	ρ_L/h $L_{\odot}$ $Mpc^{-3} \times 10^8$
Real	7493	-20.05	-1.05	1.44
Real (B/T flat)	7493	-20.08	-1.07	1.43
Real (cos(i) sel)	4769	-19.59	-0.53	1.07
Disk	N_{gal}	M^*	α (Vmax)	ρ_L/h $L_{\odot}$ $Mpc^{-3} \times 10^8$
Real	7493	-19.97	-0.93	1.19
Real (B/T flat)	7593	-19.99	-0.95	1.36
Real (cos(i) sel)	4769	-19.91	-0.50	0.58

appear to be bulge dominated but find that our results do not depend sensitively on this. Unfortunately the further limitation of this study is that it appears to have a bias in the recovered cos(i) and has revealed that the B/T ratios are sensitive to the recovered cos(i) values. An attempt to estimate the effect of the cos(i) bias by random sampling of the galaxy catalogue suggests that the results change somewhat but still remain within the quoted errors.

5.6 Acknowledgements

We are extremely grateful to Chris Miller for providing us with all of the SDSS EDR imaging data and Drs Robert Nichol and Tomotsugu Goto for the kind encouragement given in the early days of this work. We also wish to thank Dr Michael

Balogh for providing us with the SDSS DR1 density catalogue.

Funding for the creation and distribution of the SDSS Archive has been provided by the Alfred P. Sloan Foundation, the Participating Institutions, the National Aeronautics and Space Administration, the National Science Foundation, the U.S. Department of Energy, the Japanese Monbukagakusho, and the Max Planck Society. The SDSS Web site is http://www.sdss.org/.

The SDSS is managed by the Astrophysical Research Consortium (ARC) for the Participating Institutions. The Participating Institutions are The University of Chicago, Fermilab, the Institute for Advanced Study, the Japan Participation Group, The Johns Hopkins University, Los Alamos National Laboratory, the Max-Planck-Institute for Astronomy (MPIA), the Max-Planck-Institute for Astrophysics (MPA), New Mexico State University, University of Pittsburgh, Princeton University, the United States Naval Observatory, and the University of Washington.

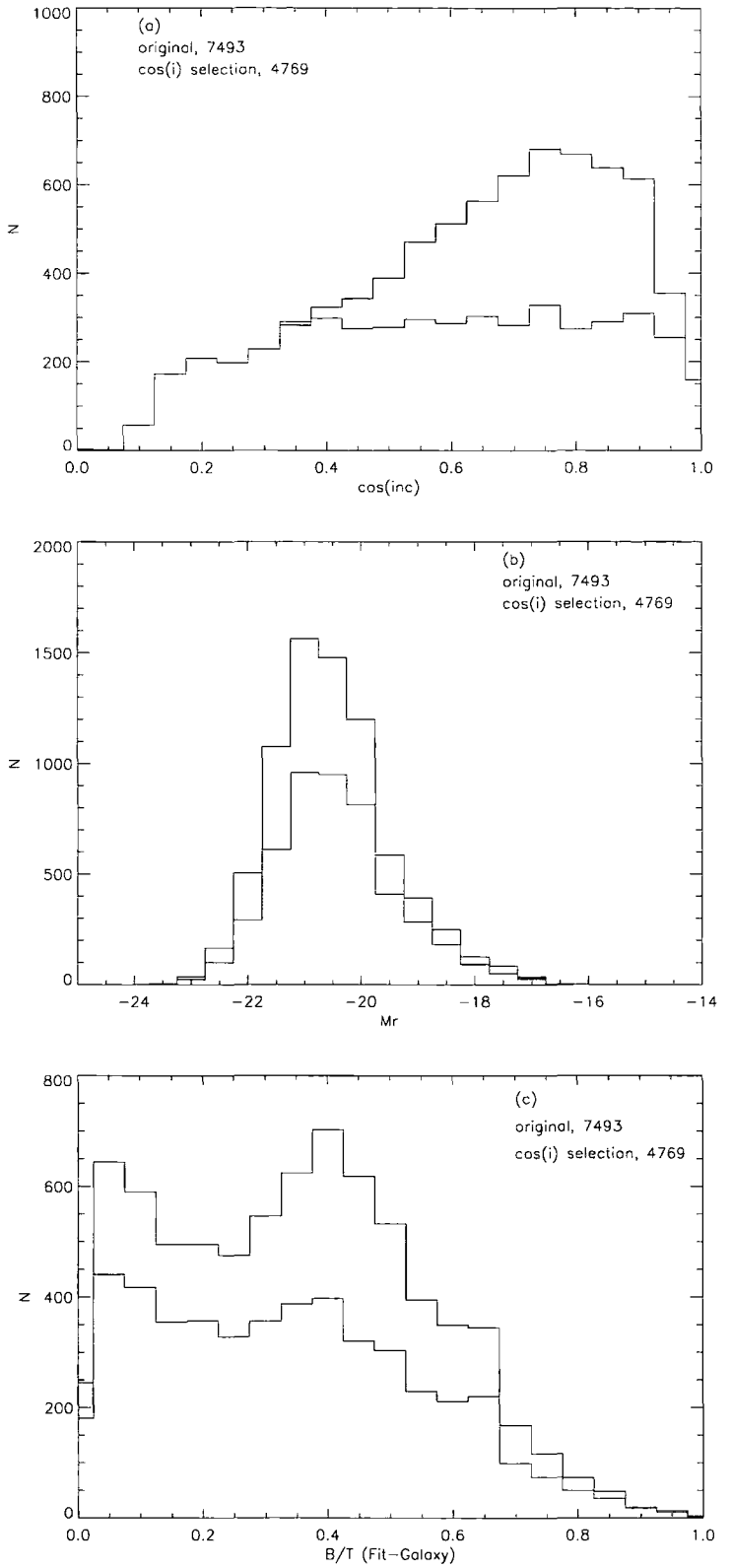

Figure 5.29: cos(i) histogram plots. (a) The original cos(i) distribution is shown as the black line while the artificially flattened cos(i) distribution is shown as a blue line. The artificial flattening is achieved by randomly throwing away galaxies wich had $0.5 <$ cos(i) < 0.9. (b) Distribution of absolute magnitudes before and after cos(i) selection. (c) Distribution of B/T ratios before and after cos(i) selection.

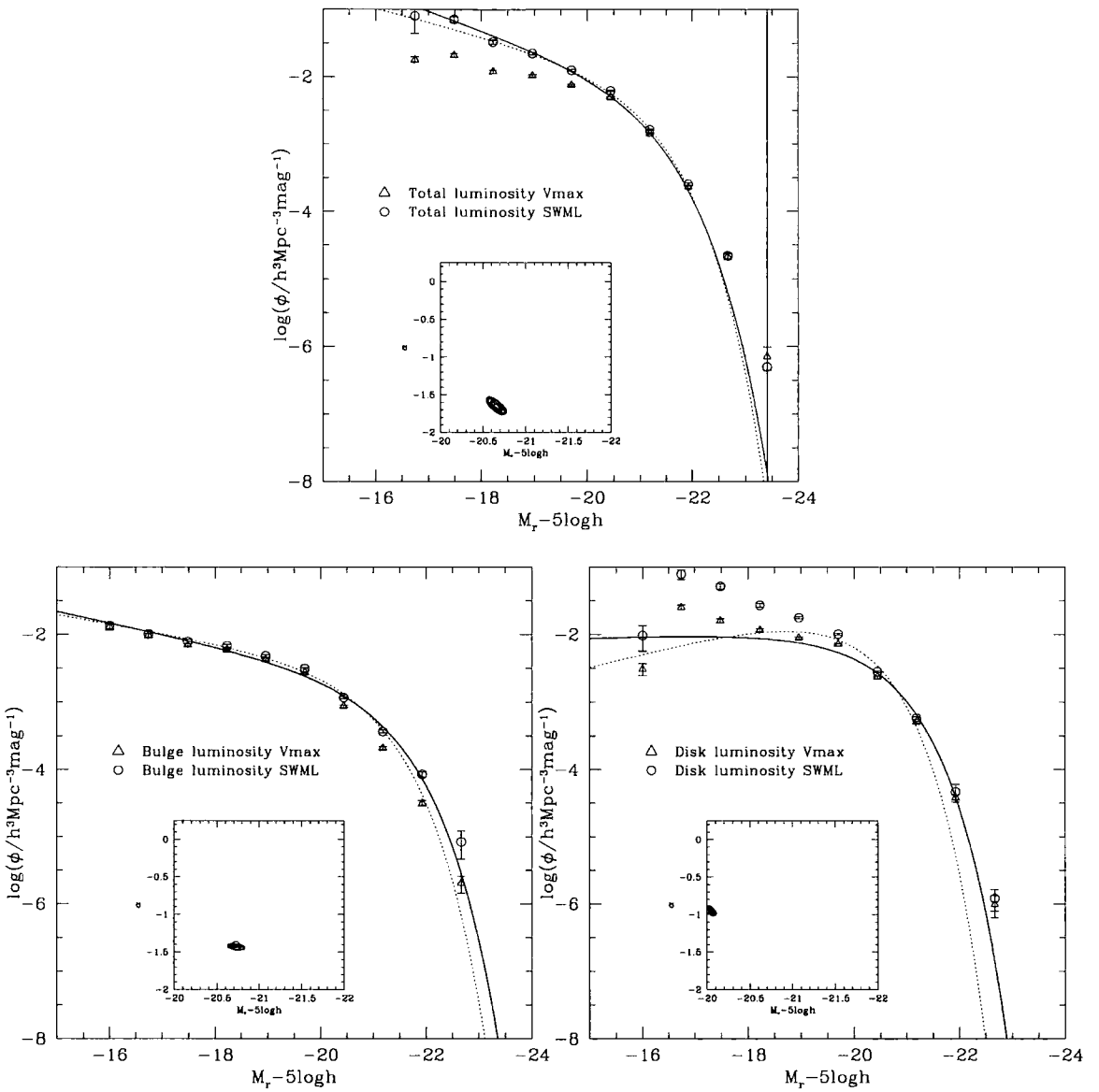

Figure 5.30: The luminosity function plots for 4769 galaxies with the artificially flattened $\cos(i)$ distribution. The LFs show a large deviation from the LF fits obtained for the original sample.

Chapter 6 | *Conclusions*

This Chapter presents a brief review of the motivation for studying structural properties of galaxies, and the overall results and conclusions of the present quantitative morphological study of galaxies in different environments and at different redshifts are also presented. The implications on the evolutionary mechanisms that appear to be responsible for the quantitative structural and morphological changes of galaxies are also discussed. Possible future extensions to this work will be highlighted.

6.1 Motivation for Quantitative Galaxy Morphology

The processes that control the formation and evolution of galaxies are still not fully understood. One of the major questions that remains unresolved is what is the origin of the morphological mix of galaxies we observe i.e. whether different morphologies are created during the initial 'monolithic' collapse (Eggen, Lyden-Bell & Sandage 1962, Jimenez et al. 1999) or whether galaxies form and evolve hierarchically (White & Frenk 1991, Kauffmann et al. 1993). Within the hierarchical structure formation framework, structure in the universe builds through continuous accretion of galaxies (White & Frenk 1991). As spiral galaxies fall into regions of higher density they can mutually interact, for example via mergers (Toomre 1977, Moore et al. 1999), but also with any gas that may fill the environment (Gunn & Gott 1972, Quilis et al. 2000). The net result is a change in the star formation rate of spiral galaxies as they enter the cluster environment (by gas exhaustion in either a gradual gas consumption or through a triggered burst of star formation) and their eventual transformation into S0s and ellipticals. The gas exhaustion occurs on a timescale of $1 - 2$ Gyrs during which galaxies become

progressively redder whilst the morphological evolution is believed to occur on a timescale of the order of several Gyrs. This is based on observations of the changes of the star formation rates and morphological changes of cluster members between redshift $z \sim 0.5$ and present (Poggianti et al. 1999, Dressler et al. 1997).

It is widely accepted that the distribution of galaxy luminosity can be described in terms of two main components - a bulge and a disk. Based on the prominence of these structural components galaxies can be visually classified into a bulge-dominated class (elliptical and S0s) and a disk-dominated class (spirals) whose central cores very much resemble the bulge-dominated systems. The connection between the various visual morphological types, their structural parameters and the interplay between galaxy disks and bulges is crucial for understanding the way galaxies formed and the way they evolve (van den Bergh 1998).

The evolution of galaxy morphology, defined in terms of the ratio of the bulge to total galaxy luminosity, within the hierarchical scenario was studied by Baugh et al. (1996b). All galaxies were assumed to have formed as disks and may subsequently evolve through mergers. By following the merger history of galaxies, the model of Baugh et al. (1996b) was successful in explaining many of the observed properties of local galaxies. In particular the morphological mix was found to match that of the present-day dense environments i.e. dominated by elliptical and S0 populations but also a large fraction of present-day ellipticals were predicted to have undergone a major merger between $0 < z < 0.5$. This implies that the progenitors of present-day ellipticals were spiral galaxies at $z \sim 0.5$, in agreement with observations that at $z \sim 0.5$ galaxy clusters are spiral-dominated (Smail et al. 1997). Although most of the present-day cluster ellipticals have undergone a violent merger in the recent past, Baugh et al. (1996b) find the scatter around the colour-magnitude relation to be small and that the colour-magnitude relation becomes bluer with redshift. The models also display a strong Butcher-Oemler effect and indicate that the large blue fraction in intermediate redshift clusters is largely due to a higher fraction of bright spirals in these clusters. Investigating the structural properties of galaxies in high density regions Baugh et al. (1996b) found them to be biased towards higher B/T

ratios than the corresponding field. One of the useful quantities that the Baugh et al. (1996b) models predict is the total amount of stellar mass locked in bulges and disks of galaxies, a quantity that can be compared with observations and is one of the motivations behind the work presented in this Thesis.

6.2 Determination of Quantitative Galaxy Morphology

Bulge and disk components can be described using empirical formalisms (de Vaucouleurs 1961, Freeman 1970) which can be employed to enable a more quantitative study of galaxy structural parameters. One of the first methods of obtaining quantitative measures of galaxy structure was in terms of one-dimensional fitting of galaxy surface brightness profiles (Kent 1985, Baggett et al. 1998). However, a problem with using the one-dimensional fitting is the loss of information through averaging over a two-dimensional surface brightness profile. This problem can be resolved by using two-dimensional fitting methods. The advantage of the two-dimensional quantitative morphological study employed in this Thesis is that it is non-subjective, reproducible and allows any biases to be understood through simulations. The quantitative methods also offer measures of the basic structural parameters associated with the galaxy surface brightness profiles such as the scale lengths of the bulge and disk components and their integrated luminosities (Wadadekar et al. 1999, Ratnatunga et al. 1999, Simard et al. 2002, Peng et al. 2002). These parameters can be used to test for any structural evolution of galaxies with redshift and/or environment (Balogh et al. 2002) and also for evolution in the amount of light associated with bulges and disks (Trujillo et al. 2004). The change of observed galaxy properties with redshift and environment is of vital importance for understanding of the current theoretical models for galaxy formation and evolution (Baugh et al. 1996a, Baugh et al. 1996b).

Chapter 2 presented a study of two independent quantitative methods for ob-

taining the morphological properties of galaxies - Gim2D of Simard et al. (2002) and Fit-Galaxy of Benson et al. (2002). Both methods use multidimensional parameter search algorithms to obtain a measure of the galaxy bulge-to-disk ratios under the assumption that a combination of the $r^{1/4}$ and the exponential disk laws can be used to separate the bulges from the disks. The codes, tested against simulated and real data, were found to agree well, but both were also found to systematically underestimate the recovered bulge-to-disk ratios for the more bulge-dominated galaxies.

In the subsequent chapters both codes have been used to study the structural properties of galaxies in high density (cluster) environments at $z \sim 0$ and $z \sim 0.5$ and the properties of the local ($z \sim 0$) field galaxy population. The derived bulge-to-disk ratios have enabled a quantitative study of the dependance of the morphological properties of galaxies with respect to redshift and environment to help constrain processes responsible for their morphological transformation and evolution.

6.3 Evolution of Galaxies in Clusters

The motivation for this work comes from the studies of Dressler (1980a) and Dressler et al. (1997), who showed that the S0/spiral ratio in clusters appears to have undergone a rapid evolution between redshifts $z \sim 0.5$ and the present. In particular it has been suggested that spiral galaxies in the $z \sim 0.5$ clusters are being transformed into present-day cluster S0s, although the exact processes responsible for this apparent transformation remain unclear (Treu et al. 2003).

Using a homogeneous sample of 13 nearby rich galaxy clusters we have determined for the first time the relation between bulge-to-total (B/T) ratio and local density and measured the present-day luminosity functions of elliptical, S0 and spiral galaxies. The total luminosity functions of spirals and S0s are found to be very similar yet the distribution of mean B/T ratios was found to differ by a factor of 2.5 across the full range in projected densities. Since a global mechanism such as ram pressure stripping that acts to transform cluster spirals into cluster S0s by stripping

the gas in the disk is not efficient in the low-density regions of these clusters, it cannot therefore be the only mechanism acting. In favour of the ram pressure stripping hypothesis playing some role is the fact that the distribution of bulge magnitudes is found to be brighter for galaxies that belong to clusters with high X-ray luminosity. If the X-ray luminosity is indicative of a larger amount of hot inter-cluster medium then the stripping should be more efficient in these clusters. This study has also demonstrated that the bulges of present-day cluster S0s are on average brighter by ~ 1 magnitude than those of spiral galaxies in similar environments. This would not be expected if present-day S0 galaxies were produced solely by disk fading in a progenitor population which has structural properties similar to that of present-day spiral galaxies. However, with the imposed apparent magnitude limit most of the faint-bulge spirals may have been lost from the sample if their disk magnitudes have faded significantly (by ≥ 1 magnitude). The similarity between the total luminosity functions of S0 and spiral galaxies in $z \sim 0$ clusters makes this argument unlikely.

The population of S0 galaxies in present-day clusters appears to have come from a population of spiral galaxies several Gyrs ago. The question is whether these spiral galaxies have the same structural properties as present-day spirals. This argument can be further investigated by looking at the properties of cluster spirals at $z \sim 0.5$.

In an attempt to measure more directly the population of galaxies responsible for the present-day population of S0s in nearby clusters quantitative measures of bulge and disk magnitudes were obtained for a statistically corrected sample of spiral galaxies from 9 intermediate redshift clusters $z \sim 0.5$. The ratio of the spiral/S0 population gave a crude estimate of the number of $z \sim 0.5$ spirals required to produce the observed S0s today, and is several times higher than observed if a simple disk fading mechanism is responsible for the spiral to S0 transformation. However, the difference in the observed structural properties between the two galaxy populations imply that a simple disk-fading mechanism is not the only mechanism acting. There is also some suggestion that a large number of morphologically pre-processed spiral galaxies needs to be accreted onto the clusters to make the $z \sim 0.5$ and $z \sim 0$ populations consistent (Kodama & Smail 2001).

6.4 Field Galaxies

In Chapter 5 the structural properties of a large sample of 8839 galaxies with r-band imaging taken from the Sloan Digital Sky Survey were studied. The study of this large statistical sample revealed a curious (and serious) bias in the inclinations of the galaxy disks as determined by the fitting codes. When the local galaxy density is used to separate the sample into low density regions typical of the field and high density regions typical of the cluster environment, it was found that in the dense environments the inclinations of galaxy disks appeared to be more uniformly distributed as expected for a random sample. This is suggestive of a potential global characteristic correlated with the galaxy environment and possibly the first evidence for an extra galaxy component that exists in the field but is somehow not present in the cluster galaxies.

Using fits to the luminosity functions of bulges and disks we find that disks contribute about 3 times more light than bulges to the total luminosity density of the universe. This result is reasonably consistent with the study of Schechter & Dressler (1987) for which the B/T ratios were visually obtained and about a factor of 2 higher than a similar but much smaller study of Benson et al. (2002). To enable a direct comparison with simulations, the bulge and disk luminosity densities should in principle be converted into the corresponding mass densities using the procedure described in Benson et al. (2002). Benson et al. (2002) used mass-to-light ratios obtained from the Bruzual & Charlot (1993) stellar population synthesis models to obtain the stellar mass associated with the luminosity of each galaxy to estimate the total mass content associated with bulges and disks. However, since the $\cos(i)$ bias for our sample stands uncorrected for we opt not to pursue the study further until a reasonable correction for the bias is achieved.

6.5 Concluding Remarks and Future Work

In this Thesis we have demonstrated that structural changes in galaxy properties do indeed happen in clusters between intermediate redshifts and the present-day. We have also presented results for the basic structural properties of field galaxy populations.

The work presented is based on determining and understanding quantitative morphological properties of galaxies in various galaxy environments. Although sophisticated, the quantitative methods employed do have some limitations and improving upon these would be a next possible thing to do. A spectroscopic and multi-band follow up of this study would be an interesting way of trying to understand galaxy evolution in clusters by minimizing field contamination and would also provide a measure of the star formation rates associated with various morphological types and their quantitative morphologies. This would allow more rigid constraints to be placed onto the current theoretical models and our underlying understanding of the physics that drives galaxy evolution.

Chapter A | *Appendix*

A.1 Method of χ^2

A common way to quantify how well the data is represented by the model is to calculate the variance weighted difference between the model and the data using the method of Chi-square (χ^2) analysis (Press et al. 1992). The method of χ^2 is based on the hypothesis that an optimum description of a set of data is that which minimizes the weighted sum of the squares of the differences between the data (D) and model (M) values. It is defined in the following way :

$$\chi^2 = \sum \frac{1}{\sigma_i^2}(D_i - M_i)^2 \tag{A.1}$$

For P data points and N parameters the number of *degrees of freedom* $\nu = P - N$ and the *reduced Chi-squared* is equal to $\chi^2_\nu = \chi^2/\nu$. The variance of the fit is estimated using the Poisson noise :

$$\sigma_i^2 = \frac{Raw_i * gain + rdnoise^2}{gain^2} \tag{A.2}$$

where Raw_i is the image data, $gain$ is the CCD gain and $rdnoise$ is the electronic read-out noise. If the model is a good representation of the data the σ^2 is expected to be close to the underlying variance of the parent distribution and $\chi^2_\nu \sim 1$.

A.2 Petrosian System

The Petrosian ratio R_P at a radius r from the center of an object is defined to be the ratio of the local surface brightness in an annulus at r to the mean surface

brightness within r (Stoughton et al. 2002) as given in Equation A.3.

$$R_P(r) = \frac{\int_{0.8r}^{1.25r} dr' 2\pi r' I(r')/[\pi(1.25^2 - 0.8^2)r^2]}{\int_0^r dr' 2\pi r' I(r')/[\pi r^2]} \tag{A.3}$$

where $I(r)$ is the azimythally averaged galaxy light profile. The Petrosian radius r_P for the SDSS data is defined as the radius at which $R_P(r_P) = 0.2$ (Stoughton et al. 2002). The Petrosian flux for the SDSS data is then defined to be the flux within an aperture radius of $2r_P$ (Equation A.4).

$$F_P = \int_0^{2r_P} 2\pi r' dr' I(r') \tag{A.4}$$

This definition of Petrosian magnitude ensures that a constant fraction of the total flux, independent of the position and distance of the object, is measured as discussed by Stoughton et al. (2002). The Petrosian magnitude obtained form the flux measured within an aperture with diameter of $4 \times r_P$ which is large enough to contain nearly all the galaxy flux whilst still being small enough for the contamination from sky to be considered unimportant (Stoughton et al. 2002).

A.3 Luminosity Function, Non-Parametric and Parametric Forms

A.3.1 Vmax Method

A traditional and one of the simplest methods of estimating the luminosity function is the method described in Felten (1977). If the survey is limited by apparent magnitude a galaxy can be seen out to a given distance before it drops out of the magnitude limited sample. The distance is given by

$$5log_{10}(D_{Lmax}) = M - m - 25 - KE(z) \tag{A.5}$$

$$V_{max} = \frac{1}{3}\Omega D_{max}^3 \tag{A.6}$$

where $V_{max} = V(L, m_{lim})$ is the total volume of space in which galaxies with luminosity L can be seen in a survey of magnitude limit m_{lim}. The luminosity function can easily be estimated by summing up the contributions from every galaxy

weighted by its V_{max} :

$$\phi(L)dL = \sum_i 1/V_{max}(Li) \tag{A.7}$$

There are a number of problems with using the $1/V_{max}$ method such as the local inhomogeneities, peculiar motion and magnitude errors (Efstathiou 1988). In shallow catalogues any local density enhancements will overestimate the contribution of intrinsically faint galaxies relative to luminous ones and therefore lead to a biased estimate of $\phi(L)$. Using a deep catalogue would minimize such a bias but such a catalogue should also cover a large area of the sky to avoid any effects such as galaxy clustering with redshift. Methods based on the maximum likelihood analysis have these spatial dependencies factored out and therefore lead to less biased estimates of the luminosity function.

A.3.2 Maximum Likelihood Methods : STY and SWML

The maximum likelihood method was first proposed by Sandage, Tammann & Yahil (1979). The probablility that a galaxy with redshift z_i and luminosity L_i is seen in a magnitude-limited survey is :

$$p_i \propto \phi(L_i) / \int_{L_{min(z_i)}}^{\infty} \phi(L)dL \tag{A.8}$$

The likelihood function is thus defined as :

$$\mathcal{L} = \prod_i p_i \tag{A.9}$$

At this point one can adopt a parametric form for the luminosity function such as the Schechter function (Schechter 1976) is given by :

$$\phi(L)dL = \phi^*(L/L^*)^{(\alpha+1)} exp[L/L^*] \tag{A.10}$$

or expressed in terms of absolute magnitudes,

$$\phi(M)dM = 0.4 \ln 10 \phi^* 10^{-0.4(M-M^*)(\alpha+1)} exp[-10^{-0.4(M-M^*)}] \quad \text{(A.11)}$$

where $phi(L)dL$ is the number of galaxies per unit volume in the luminosity interval from L to L+dL. M^* is some characteristic absolute magnitude (that corresponds to a characteristic luminosity), α is the slope of the luminosity function and ϕ^* is the normalization. The maximum likelihood technique therefore allows for the individual parameters to be obtained by requiring that the product od individual probablilities be maximized. This method was first proposed by Sandage, Tamman and Yahil (1979) and is commonly known as the STY method. The parameters obtained from the fit can be used to estimate various statistical properties such as the total luminosity density contributed by the Schechter function :

$$L_{tot} = \int_0^\infty L\phi(L)d(L) = \phi^* L^* \Gamma(\alpha + 2) \quad \text{(A.12)}$$

A sligtly different method also based upon the maximum likelihood analysis is the Stepwise Maximum Likelihood method (SWML, hereafter) of ? where no analythic form for $\phi(L)$ is assumed. Instead the luminosity function is parametarised as a series of steps.

$$\phi(L) = \phi_k, L_k - \Delta L/2 < L < L_k + \Delta L \quad \text{(A.13)}$$

the likelihood function becomes :

$$\begin{aligned} \mathrm{Ln}[\mathcal{L}] &= \sum_{i=1}^{N} \mathrm{Ln}\left[\sum_{k=1}^{N_p} \phi_k \mathrm{W}(\widetilde{\mathrm{L}}_i - \mathrm{L}_k)\right] \\ &- \sum_{i=1}^{N} \mathrm{Ln}\left[\sum_{k=1}^{N_p} \phi_k \Delta \mathrm{LH}[\mathrm{L}_k - \mathrm{L}_{min}(z_i)]\right] + \tilde{c} \end{aligned} \quad \text{(A.14)}$$

$$W_k(M_i) = \{1 if M_k - \Delta M/2 < M < M_k + \Delta M/20, \text{otherwise} \quad \text{(A.15)}$$

$$H(x) = \begin{cases} 0 & x \leq -\Delta L/2 \\ x/\Delta L + 1/2 & -\Delta L/2 \leq x \leq \Delta L/2 \\ 1 & x \geq \Delta L/2 \end{cases} \quad (A.16)$$

The SWML method is useful since it does not requre an analythic LF. The STY method is useful too since the values obtained can readily be compared between different surveys. To make different surveys fully comparable since they encompass diffrent areas of the sky we need to determine the normalization of the LF, ϕ^*. If we only consider galaxies with luminosities in the range $L_1 < L < L_2$ then the normalization is given by the probability that a galaxy at some redshift z is observed in the survey :

$$S(z) = \frac{\int_{min[L_{min(z)}, L1]}^{L_2} \phi(L) d(L)}{\int_{L1}^{L_2} \phi(L) d(L)} \quad (A.17)$$

A.3.3 Two-Dimensional Luminosity Function, Vmax, STY and SWML Methods

All of the above proposed LF estimators can be adapted to the case of spheroid and disk luminosity functions. One has to bear in mind that the detectability of a spheroid depends on both its apparent magnitude and the B/T ratio.

A.3.4 Vmax Method : 2D

This estimator is applied just as in the case of the standard luminosity function, except that the *total* luminosity of the galaxy is used to compute V_{max} since it is this total luminosity that determines the volume within which each galaxy is detected.

A.3.5 Maximum Likelihood Methods : STY and SWML : 2D

We can define a two-dimensional function, $\Phi(M, B)$, such that $\Phi(M, B)dMdB$ is the number of galaxies per unit volume with B/T ratio in the range B to B+dB

and *spheroid* absolute magnitude in the range M to M+dM. The normal luminosity function of spheroids can be derved using $\phi(M) = \int_0^1 \Phi(M,B)dB$. The probababil-ity that galaxy i with spheroid absolute magnitude $M_i$and bulge-to-total ratio $B_i$is seen in a magnitude limited survey is :

$$p_i \propto \Phi(M_i, B_i) / \int_0^1 \int_{-\infty}^{M_{lim(z_i,B)'}} \Phi(M,B)dMdB \tag{A.18}$$

where $M_{lim}(z_i, B) = M_{lim}(z_i) - 2.5 \log B$ and $M_{lim}(z_i)$ is the limiting *total* ab-solute magnitude of the survey at redshift z_i (Benson et al. 2002). The use of M_{lim} is necessary since arbitrarily faint spheroids will make it into the survey providing they have sufficiently bright disks and vice-versa. The likelihood function is then given as :

$$\ln \mathcal{L} = \sum_{i=1}^{N} \ln \Phi(M_i, B_i) - \sum_{i=1}^{N} \ln\{\int_0^1 \int_{-\infty}^{M_{lim(z_i,B)'}} \Phi(M,B)dMdB\} + \text{const} \tag{A.19}$$

where N is the total number of galaxies.

At this point one can adopt a parametric form for the luminosity function is given by :

$$\Phi(M,B) = \phi(M) \exp(\beta B) \tag{A.20}$$

where $\phi(M)$ is the Schecter function and β is to be estimated from the fit (as well as M^* and α as before).

We can also parametarise the SWML estimate of $\Phi(M,B)$ in the following way :

$$\phi(M,B) = \phi_{k,h}, \quad \text{if} \quad M_k - \Delta M/2 < M < M_k + \Delta M/2 \tag{A.21}$$

$$0, \quad \text{if} \quad B_h - \Delta B/2 < B < B_h + \Delta B/2 \tag{A.22}$$

the likelihood function becomes :

$$\mathrm{Ln}[\mathcal{L}] = \sum_{i=1}^{N} \mathrm{W}(\mathrm{M_i}-\mathrm{M_k}, \mathrm{B_i}-\mathrm{B_h}) \ln \Phi_{\mathrm{k,h}} - \sum_{i=1}^{N} \ln\{\sum_{h=1}^{N_q}\sum_{k=1}^{N_p} \Phi_{\mathrm{k,h}} \Delta\mathrm{M}\Delta\mathrm{B}\mathrm{H}[\mathrm{M_k}, \mathrm{B_h}, \mathrm{M_{lim}}(z_i)]\} + \mathrm{con} \tag{A.23}$$

where,

$$W_{h,k}(M_i, B_i) = 1, \quad \text{if} \quad M_k - \Delta M/2 < M < M_k + \Delta M/2 \tag{A.24}$$

$$\text{and} \quad B_h - \Delta B/2 < B < B_h + \Delta B/2, \tag{A.25}$$

$$0, \quad \text{otherwise} \tag{A.26}$$

and,

$$\mathrm{H}[\mathrm{M_k}, \mathrm{B_h}, \mathrm{M_{lim}}(z_i) = \frac{1}{\Delta\mathrm{M}\Delta\mathrm{B}} \int_{\mathrm{B_h}-\Delta\mathrm{B}/2}^{\mathrm{B_h}+\Delta\mathrm{B}/2} \int_{\mathrm{M_k}-\Delta\mathrm{M}/2}^{\mathrm{M_k}+\Delta\mathrm{M}/2} \mathrm{Q}(\mathrm{M}, \mathrm{B})\mathrm{dMdB} \tag{A.27}$$

where $Q(M, B) = 0$ if $M > M_{lim}(z_i) - 2.5 \log B$ and $Q(M, B) = 1$ otherwise.

Bibliography

The following abbreviations are used in this bibliography :

MNRAS: Monthly Notices of the Royal Astronomical Society

ApJ: The Astrophysical Journal

ApJS: The Astrophysical Journal Supplement

AJ: The Astronomical Journal

A&A: Astronomy and Astrophysics

ARA&A: Annual Reviews of Astronomy and Astrophysics

Abraham R.G., Valdes F., Yee H.K.C. & van den Bergh S., 1994, ApJ, **432**, 75-90.

Abraham R.G. & van den Bergh S., 2001, Science, **293**, 1273-1278.

Abadi M.G., Moore B. & Bower R.G., 1999, MNRAS, **308**, 947-954.

Andredakis Y.C., Peletier R.F. & Balcells M., 1995, **275**, 874A.

Baggett W.E., Baggett S.M. & Anderson K.S.J., 1998, AJ, 116, 1626-1642.

Balogh, M. L., Bower, R. G., Smail, I., Ziegler, B. L., Davies, R. L., Gaztelu, A., & Fritz A., 2002, MNRAS, **337**, 256B.

Balogh M.L., Smail I., Bower R.G., Ziegler B.L., Smith G.P., Davies R.L., Gaztelu A., Kneib J.-P. & Ebeling H., 2002, ApJ, **566**, 123-136.

Balogh M., Eke V., Miller C., Lewis I., Bower R.G., Couch W., Nichol R., Bland-Hawthorn J., Baldry I.K., Baugh C., Bridges T., Cannon R., Cole S., Colless M., Collins C., Cross N., and Dalton G., de Propris R., Driver S.P., Efstathiou G., Ellis R.S., Frenk C.S., Glazebrook K., Gomez P., Gray A., Hawkins E., Jackson

C., Lahav O., Lumsden S., Maddox S., Madgwick D., Norberg P., Peacock J.A., Percival W., Peterson B.A., Sutherland W. & Taylor K., 2004, MNRAS, **348**, 1355-1372.

Balogh M.L., Baldry I.K., Nichol R., Miller C., Bower R. & Glazebrook K., 2004, astro-ph/0406266.

Barger A.J., Aragon-Salamanca A., Smail I., Ellis R.S., Couch W.J., Dressler A., Oemler A., Poggianti B.M. & Sharples R.M., 1998, ApJ, **501**, 522-+.

Barnes J.E. & Hernquist L., 1992, ARA&A, **30**, 705-742.

Baugh C.M., Cole S. & Frenk C.S., 1996a, MNRAS, **282**, L27-L32.

Baugh C.M., Cole S. & Frenk C.S., 1996b, MNRAS, **283**, 1361-1378.

Benson A.J., Frenk C.S. & Sharples R.M., 2002, ApJ, **574**, 104B.

Bertin E. & Arnouts S., 1996, A&A, **117**, 393.

Beijersbergen M., de Blok W.J.G. & van der Hulst J.M., 1999, **351**, 903-919.

Bekki K., Couch W.J. & Shioya Y., 2002, ApJ, **577**, 651-657.

Binney J. & Merrifield M., 1998, *Galactic Astronomy*, Princeton University Press.

Blanton M.R., et al., 2001, AJ, **121**, 2358.

Bower R.G., Kodama T. & Terlevich A., 1998, MNRAS, **299**, 1193-1208.

Bower R.G., Lucey J.R. & Ellis R.S., 1992, MNRAS, **254**, 601B.

Bower R.G., 1990, *Ph.D.Thesis*, University of Durham.

Bruzual A. G., & Charlot S., 1993, ApJ, **405**, 538B.

Butcher H. & Oemler A.Jr., 1984, ApJ, **285**, 426-438.

Butcher H. & Oemler A.Jr., 1985, ApSS, **57**, 665-691.

Christlein D. & Zabludoff A., 2004, astro-ph/0408036.

Cole S., Norberg P., Baugh C.M., Frenk C.S., Bland-Hawthorn J., Bridges T., Cannon R., Colless M., Collins C., Couch W., Cross N., Dalton G., De Propris R., Driver S.P., Efstathiou G., Ellis R.S., Glazebrook K., Jackson C., Lahav O., Lewis I., Lumsden S., Maddox S., Madgwick D., Peacock J.A., Peterson B.A., Sutherland W. & Taylor K., 2001, MNRAS, **326**, 255-273.

Couch W.J., Ellis R.S., Sharples R.M. & Smail I., 1994, ApJ, **430**, 121-138.

Couch W.J., Barger A.J., Smail I., Ellis R.S. & Sharples R.M., 1998, ApJ, **497**, 188.

de Jong R. S., 1996, A&AS, **118**, 557-573.

de Vaucouleurs G., 1961, ApJS, **5**, 233.

de Vaucouleurs G. & de Vaucouleurs A., 1964, *Reference catalogue of bright galaxies', University of Texas Monographs in Astronomy*, Austin: University of Texas Press.

de Vaucouleurs G., de Vaucouleurs A. & Corwin H.G., 1976, *Second Reference Catalogue of Bright Galaxies*, Austin : University of Texas Press.

Domínguez M., Muriel H. & Lambas D.G., 2001, AJ, **121**, 1266-1274.

Dressler A., 1980, ApJ, **236**, 351-365.

Dressler A., 1980, ApJS, **42**, 565-609.

Dressler A., Oemler A.Jr., Couch W.J., Smail I., Ellis R.S., Barger A., Butcher H., Poggianti B.M. & Sharples R.M., 1997, ApJ, **490**, 577-591.

Dressler A., Smail I., Poggianti B.M., Butcher H., Couch W.J., Ellis R.S. & Oemler A.J., 1999, ApJs, **122**, 51-80.

Efstathiou G., Ellis R. S. & Peterson B. A., 1988, MNRAS, **232**, 431.

Efstathiou G., 1993, *Les Houches Lectures : Observations of Large-Scale Structure in the Universe*, Elsevier Science Publishers.

Eggen O.J., Lynden-Bell D. & Sandage A.R., 1962, ApJ, **136**, 748.

Ellis R.S., Smail I., Dressler A., Couch W.J., Oemler A.J., Butcher H. & Sharples R.M., 1997, ApJ, **483**, 582-+.

Felten J.E., 1977, AJ, **82**, 861-878.

Freeman, K.C., 1970, ApJ, **160**, 811-+.

Fujita Y., 1998, ApJ, **509**, 587-594.

Fukugita M., Shimasaku K. & Ichikawa T., 1995, PASP, **107**, 945.

Fukugita M., Ichikawa T., Gunn J.E., Doi M., Shimasaku K. & Schneider D.P., 1996, AJ, **111**, 1748.

Gardner J.P., Sharples R.M., Carrasco B.E. & Frenk C.S., 1996, MNRAS, **282**.

Gisler G.R., 1979, ApJ, **228**, 385G.

Goto T., Okamura S., McKay T.A., Bahcall N.A., Annis J., Bernardi M., Brinkmann J., Gómez P.L., Hansen S., Kim R.S.J., Sekiguchi M. & Sheth R.K., 2002, PASJ, **54**, 515-525.

Goto T., Yamauchi C., Fujita Y., Okamura S., Sekiguchi M., Smail I., Bernardi M. & Gomez P.L., 2003, MNRAS, **346**, 601-614.

Griffiths R.E., Casertano S., Ratnatunga K.U., Neuschaefer L.W., Ellis R.S., Gilmore G.F., Glazebrook K., Santiago B., Huchra J.P., Windhorst R.A., Pascarelle S.M., Green R.F., Illingworth G.D., Koo D.C. & Tyson A.J., 1994, ApJL, **435**, L19-L22.

Gunn J.E. & Gott J.R., 1972, ApJ, **176**, 1.

Helsdon S.F. &Ponman T.J., 2003, MNRAS, **340**, 485-498.

Hubble E.P., 1936, *Realm of the Nebulae*, Yale University Press.

Jimenez R., Friaca A.C.S., Dunlop J.S., Terlevich R.J., Peacock J.A. & Nolan L.A., 1999, MNRAS, **305**, L16-L20.

Kauffmann G., White S.D.M. & Guiderdoni B., 1993, MNRAS, **264**, 201.

Kennicutt, R.C., 1998, ARAA, **36**, 189-232.

Kent, S. M., 1985, AJSS, **59**, 115-159.

Kodama T., Balogh M.L., Smail I., Bower R.G. & Nakata F., 2004, astro-ph/0408037.

Kodama T. & Bower R.G., 2001, MNRAS, **321**, 18-36.

Kodama T. & Smail I., 2001, MNRAS, **326**, 637-642.

Krist J., 1995, *ASP Conf. Ser. 77: Astronomical Data Analysis Software and Systems IV*, 349.

Landolt A.U., 1992, AJ, **104**, 340L.

Ledlow M.J., Voges W., Owen F.N. & Burns J.O., 2003, astro-ph/0310175.

Lilly S.J., Le Fevre O., Hammer F. & Crampton D., 1996, ApJL, **460**, L1+.

Lucey J.R., Guzman R., Steel J. & Carter D., 1997, MNRAS, **287**, 899-914.

Lupton R.H., Gunn J.E., Ivezić Z., Knapp G.R., Kent S. & Yasuda N., 2001, ADASS, **10**, 269L.

McIntosh D.H., Rix H-W. & Caldwell N., 2002, astro-ph/0212427.

Metropolis N., Rosenbluth A., Rosenbluth M., Teller A. & Teller E., 1953, Journal of Chemical Physics, **21**, 1087.

Moffat A.F.J., 1969, AAP, **3**, 455+.

Moore B., Lake G., Quinn T. & Stadel J., 1999, MNRAS, **304**, 465-474.

Moss C. & Whittle M., 2000, **317**, 667-686.

Nakamura O., Fukugita M., Yasuda N., Loveday J., Brinkmann J., Schneider D.P., Shimasaku K. & SubbaRao M., 2003, AJ, **125**, 1682-1688.

Nelson A. E., Simard L., Zaritsky D., Dalcanton J. J. & Gonzalez A. H., 2002, AJ, **567**, 144.

Norberg P., Cole S., Baugh C.M., Frenk C.S., Baldry I., Bland-Hawthorn J., Bridges T., Cannon R., Colless M., Collins C., Couch W., Cross N.J.G., Dalton G., De Propris R. Driver S.P., Efstathiou G., Ellis R.S., Glazebrook K., Jackson C., Lahav O., Lewis I., Lumsden S., Maddox S., Madgwick D., Peacock J.A., Peterson B.A., Sutherland W. & Taylor K., 2002, MNRAS, **336**, 907-931.

Oemler A., 1992, *Environmental Influences on Galaxy Morphology*, NATO ASIC Proc. 366: Clusters and Superclusters of Galaxies.

Oemler A.J., 1974, ApJ, **194**, 1-20.

Peng C.Y., Ho L.C., Impey C.D. & Rix H., 2002, AJ, **124**, 266-293.

Petrosian V., 1976, ApJ, **209L**, 1P.

Poggianti B.M., Smail I., Dressler A., Couch W.J., Barger A.J., Butcher H., Ellis R.S. & Oemler A.J., 1999, ApJ, **518**, 576-593.

Press W.H., Teukolsky S.A., Vetterling W.T. & Flannery B.P., 1992, *Numerical Recipes in FORTRAN*, Cambridge University Press, Chapter 10.

Quilis V., Moore B. & Bower R.G., 2000, Science, **288**, 1617-1620.

Ratnatunga K.U., Griffiths R.E. & Ostrander E.J., 1999, AJ, **118**, 86-107.

Salpeter E.E., 1955, ApJ, **121**, 161S.

Sandage A., 1961, *The Hubble atlas of galaxies*, Washington: Carnegie Institution.

Sandage A. & Brucato R., 1979, AJ, **884**, 472-475.

Sandage A., Tammann G.A. & Yahil A., 1979, ApJ, **232**, 352-364.

Sandage A. & Tammann G.A., 1981, *Book Review*, Washington: Carnegie Institution.

Schechter P., 1976, ApJ, **203**, 297-306.

Schechter P.L. & Dressler A., 1987, AJ, **94**, 563S.

Sérsic J.-L., 1968, *Atlas de Galaxias Australes*, Cordoba : Obs. Astronomico, Generalised $R^{1/4}$ law.

Shimasaku K., Fukugita M., Doi M., Hamabe M., Ichikawa T., Okamura S., Sekiguchi M., Yasuda N., Brinkmann J., Csabai I., Ichikawa S., Ivezić Z., Kunszt P.Z., Schneider D.P., Szokoly G.P., Watanabe M. & York D.G., 2001, AJ, **122**, 1238-1250.

Simard L., Willmer C.N.A., Vogt N.P., Sarajedini V.L., Phillips A.C., Weiner B.J., Koo D.C., Im M., Illingworth G.K. & Faber S.M., 2002, ApJS, **142**, 1S.

Smail I., Dressler A., Couch W.J., Ellis R.S., Oemler A.J., Butcher H. & Sharples R.M., 1997, ApJs, **110**, 213-+.

Smith G.P., Treu T., Ellis R.E, Moran S.M. & Dressler A., 2004, astro-ph/0403455.

Solanes J.M. & Salvador-Sole E., 1992, ApJ, **395**, 91S.

Stoughton C., et al., 2002, AJ, **123**, 485S.

Strateva I., et al., 2001, AJ, **122**, 1861S.

Toomre A., 1977, *Evolution of Galaxies and Stellar Populations*, Yale University Press.

Tran K.H., Simard L., Illingworth G. & Franx M., 2003, ApJ, **590**, 238-255.

Treu T., Ellis R.S., Kneib J., Dressler A., Smail I., Czoske O., Oemler A. & Natarajan P., 2003, ApJ, **591**, 53-78.

Trujillo I., Aguerri J.A.L., Cepa J. & Gutiérrez C.M., 2001, MNRAS, **328**, 977-985.

Trujillo I., Aguerri J.A.L., Gutiérrez C.M. & Cepa J., AJ, **122**, 38-54.

Trujillo I., Gutiérrez C.M., Aguerri J.A.L. & Cepa J., 2003, *Revista Mexicana de Astronomia y Astrofisica Conference Series*, 315-316.

van den Bergh S., 1998, *Galaxy Morphology and Classification*, Cambridge University Press.

Wadadekar Y., Robbason B. & Kembhavi A., 1999, AJ, **117**, 1219-1228.

White S.D.M. & Frenk C.S., 1991, ApJ, **379**, 52-79.

Whitmore B.C., Gilmore D.M. & Jones C., 1993, ApJ, **407**, 489-509.

Yasuda N., Fukugita M., Narayanan V.K., Lupton R.H., Strateva I., Strauss M.A., Ivezić Ž., Kim R.S.J., Hogg D.W., Weinberg D.H., Shimasaku K., Loveday J., Annis J., Bahcall N.A., Blanton M., Brinkmann J., Brunner R.J., Connolly A.J., Csabai I., Doi M., Hamabe M., Ichikawa S., Ichikawa T., Johnston D.E., Knapp G.R., Kunszt P.Z., Lamb D.Q., McKay T.A., Munn J.A., Nichol R.C., Okamura S., Schneider D.P., Szokoly G.P., Vogeley M.S., Watanabe M. & York D.G., 2001, AJ, **122**, 1104-1124.